AN ABSTRACT OF THE DISSERTATION OF

Whitney L. Schmidt for the degree of Doctor of Philosophy in Chemistry presented on March 17, 2014.

Title: Synthesis and Investigation of Layered Oxides with Honeycomb Ordering

Abstract approved:

_____

Munirpallam A. Subramanian

Synthesis and discovery lies at the core of every field in chemistry. The investigation of the structure-property relationships in compounds known or new is the fundamental purpose of solid state chemistry. Mixing related solid state compounds to form solid solutions can lead to exciting new and/or unexpected properties. Layered compounds are used in everyday technology, especially batteries. A renewed interest in layered oxides with honeycomb ordering has arisen in the past two years with the discovery of many new compositions as well as the reinvestigation to clarify the structure and properties of previously reported compounds.

In this work the discovery and characterization of 7 new compounds is presented and discussed. One family of solid solutions that was investigated have the compositions $Na_3M_{2-x}M'_xSbO_6$ where M, M' = Cu, Mg, Ni, Zn. All compositions crystallize in the *C*2/*m* space group and contain a honeycomb ordering within the M^{2+}/Sb^{5+} edge-sharing octahedra. X-ray diffraction verified lattice parameter trends based on the ionic radii of the M^{2+} cations however, the Jahn-Teller active Cu^{2+} ion creates larger differences than predicted. The antiferromagnetic order in $Na_3Ni_2SbO_6$ and the spin gap magnetic behavior of $Na_3Cu_2SbO_6$ are suppressed upon

substitution with the nonmagnetic Zn^{2+} and Mg^{2+} cations. Estimated band gaps for these compounds are determined from diffuse reflectance measurements.

Two compositions that were discovered during this work were $Na_3LiFeSbO_6$ (space group *C*2/*c*) and the ion exchange delafossite $Ag_3LiFeSbO_6$ (space group $P3_112$. The space group index of $Na_3NaFeSbO_6$ was also reinvestigated. These compounds are related to the previous materials with a lamellar structure with Na^+ filling interlayer space between $Li_{1/3}Fe_{1/3}Sb_{1/3}O_2$ slabs. A high degree of stacking faults was present in the X-ray diffraction patterns preventing full structural characterization. Magnetic susceptibility verified the presence of high spin Fe^{3+}. In order to determine some information regarding the arrangement of cations within the slabs ^{57}Fe Mössbauer spectroscopy was employed.

The new layered compound $Li_3Ni_2BiO_6$ was discovered as well as the partially substituted phases $Li_3NiM'BiO_6$ (M' = Mg, Cu, Zn). These compounds crystallize in the monoclinic *C*2/*m* space group. These compounds have a lamellar structure with a honeycomb ordering between the Ni^{2+} and Bi^{5+} within the slabs which are separated by Li^+ ions filling the interlayer space. Magnetic susceptibility measurements indicate paramagnetic behavior of all the compositions at high temperature and only the parent compound $Li_3Ni_2BiO_6$ contains an antiferromagnetic ordering at 5.5 K. Topotactic molten salt ion exchange was used to synthesize the new delafossite $Ag_3Ni_2BiO_6$. Compositions of $Li_3Ni_2BiO_6$ and the exchange compound $Ag_3Ni_2BiO_6$ were verified using inductively coupled plasma – atomic emission spectroscopy.

Solid solution studies were also performed as part of this work where structural transitions and property modifications were observed for two families of compounds. In the family of P2-$Na_2M_2TeO_6$ (M = Co, Ni, Zn), three full solid solutions were prepared. These too contain a M^{2+}/X^{6+} honeycomb ordering within slabs of edge-sharing octahedra which are separated by nonstoichiometric filling of Na^+ in trigonal prismatic interlayer sites. All compounds crystallize in a hexagonal unit cell however, a different stacking sequence is observed for the nickel (space

group $P6_3/mcm$) containing composition compared to the zinc and cobalt compositions (space group $P6_322$) causing a structural transition to occur when nickel is substituted by zinc or cobalt which was monitored using X-ray diffraction. Magnetic susceptibility indicates high temperature paramagnetic behavior in all compositions with low temperature antiferromagnetic transitions in the compounds containing nickel or cobalt. This transition is suppressed upon zinc substitution. An interesting color transition from pink to light green to white was observed for M = Co, Ni, Zn, respectively, and was examined using diffuse reflectance spectroscopy.

Synthesis and Investigation of Layered Oxides with Honeycomb Ordering

by
Whitney L. Schmidt

A DISSERTATION

submitted to

Oregon State University

in partial fulfillment of
the requirements for the
degree of

Doctor of Philosophy

Presented March 17, 2014
Commencement June 2014

Doctor of Philosophy dissertation of Whitney L. Schmidt presented on March 17, 2014

APPROVED:

Major Professor, representing Chemistry

Chair of the Department of Chemistry

Dean of the Graduate School

I understand that my dissertation will become part of the permanent collection of Oregon State University libraries. My signature below authorizes release of my dissertation to any reader upon request.

Whitney L. Schmidt, Author

ACKNOWLEDGEMENTS

The author expresses sincere appreciation to Dr. Mas Subramanian, who graciously accepted me as the third student to join his large research group in the fall of 2010. After a slow start to my first term in graduate school, he pushed me to begin research in January 2011 starting with hydrothermal synthesis, a technique that was not familiar to most of the group. Although I did not have a solid state chemistry background, his laboratory lent itself to a curious mind, where he has provided all the necessary equipment and materials for success. He encouraged me to pursue projects that complimented my research style (slow and steady wins the race!) and interests. Upon hiring a postdoctoral researcher Dr. Romain Berthelot, Mas recognized that his background complimented my interests and encouraged our collaboration to start my thesis work.

I would like to thank my entire PhD committee, Dr. Arthur Sleight, Dr. Michael Lerner, Dr. Brady Gibbons and Dr. David Graham for insightful discussion during my program meeting and oral examination. I am grateful for their dedication serving as my committee. I am very thankful to Dr. Gibbons who took on the additional role of becoming a mentor and encouraging me through the rough times I encountered through graduate school.

I am also eternally grateful for Dr. Romain Berthelot and his dedication to my individual progress during his postdoctoral work at OSU. His guidance and knowledge of layered oxide materials was invaluable to my success. He made contributions to Chapters 4-7 which are all published works.

I also acknowledge Dr. Jun Li who has been a wonderful office mate for the last year of my PhD and all the help she has provided to our entire group for the years she has been here.

To my lab mates, especially those who have tread the path alongside me Geneva Laurita-Plankis and Rosa Grajczyk, we would not be the “Masketeers”

without each other. To Dr. Sean Muir, Dr. Alvin Gatimu, Dr. Peng Jiang, Dr. June Thiritanon and Dr. James Eilertsen who were so helpful with training and discussions about solid state chemistry when I first started. To the many friends I have made from all different divisions and departments, you have kept me up to speed on subjects outside my dissertation bubble and provided support during my times of need.

It has been a wonderful experience to work at such a beautiful campus that we have here at Oregon State University. The walks around campus were refreshing when everything became too much. I am grateful for the Chemistry department and the support they have provided during my time here. I have had the opportunity to TA the general chemistry (science and non-science students) and the junior and senior Chemistry major undergraduates. My final summer research was funded by the David P. Shoemaker Fellowship which allowed me to focus on finishing up many projects.

To where it all started from elementary school with Mrs. Hubbard who implemented wonderful science experiments to my 3rd grade class to middle school with Mr. Elam where I first saw the reaction of sodium metal with water, to high school with Dr. Weber who was such a wonderful Physics and Chemistry teacher and provided the foundation to my success going into college. I was lucky to be part of the K-12 program in Campbell County, KY with all my teachers along the way.

My first experience as a researcher was during my undergraduate career in the Chemistry department at Northern Kentucky University. The facilities provided, for lab courses and research, were phenomenal and provided me with an exemplary foundation for chemistry. My advisor Heather A. Bullen was always enthusiastic and taught me that it is unacceptable to make excuses. She was such an inspiration personally and professionally.

TABLE OF CONTENTS

TABLE OF CONTENTS (Continued)

TABLE OF CONTENTS (Continued)

Page

TABLE OF CONTENTS (Continued)

Page

LIST OF FIGURES

Figure Page

LIST OF FIGURES (Continued)

LIST OF FIGURES (Continued)

LIST OF FIGURES (Continued)

LIST OF FIGURES (Continued)

LIST OF FIGURES (Continued)

LIST OF FIGURES (Continued)

LIST OF FIGURES (Continued)

LIST OF TABLES

DEDICATION

For my uncommon parents who instilled in me the beliefs, morals and ideals that have carried me through life. For my Dad, you always answered the phone when I was far away and terrified. For my Mom, always sharing your dreams and fostering my independent spirit.

For my favorite brother, who helped me develop a thick skin and always included me to make sure I wasn't just your little sister.

For my grandparents, who are and were the perfect examples of living, loving and dreaming.

For my family and friends, I am so blessed.

For me, what an unwonted life I have had the pleasure to live.

Chapter 1

Introduction

Solid state chemistry is only about a century old. Many of the fundamentals that are used in this field, such as characterization of crystalline materials with X-rays, were also only discovered about 100 years ago. Solid state chemists rely on the same principles that Mendeleev used to build one of the first periodic tables and predict the unknown elements during that time. These properties and trends in the elements dominate the structures that can be formed and the coordination environment that an element can exist in. The relationship between structure and properties is the fundamental background to solid state chemistry. The ultimate driving force for solid state chemistry is the search for new and efficient technology in the areas of energy storage materials, solar cells, microelectronic devices and lighting devices.

1.1 Layered Solid State Structures

The fundamentals of building solid state structures will be reviewed in this section. As this dissertation work focuses on a family of layered quaternary oxides, the emphasis will be on building layered structures starting from the simplest of solid state compounds.

1.1.1 Basic Atomic Packing Sequences

Crystalline materials are built when atoms organize in periodic arrangements. If an atom is considered as a sphere, there are a few stacking sequences that can occur to build a crystalline materials. Simple cubic packing is where each atom is surrounded by four spheres in the same plane, one above and one below; creating a layer sequence of AA… (Figure 1.1a). Interstitial sites are void spaces within the packing of the main atoms. In this simple cubic packing there are interstices that have eight spheres surrounding the void space. Close packing of spheres creates a more dense arrangement of atoms than the simple cubic packing. Figure 1.1b illustrates a close packing of purple spheres for the first layer. A second layer can then be placed above the first in two places indicated by the orange and blue dots between the purple spheres. When the second layer is placed in the orange positions you get an AB… stacking sequence and the blue positions are empty as seen by the white space in Figure 1.1c. If this AB stacking is repeated, the structure is in a hexagonal close packed array. If the third layer is placed in the blue, C, positions, the stacking sequence is ABC (Figure 1.1d). When this sequence is repeated, the structure is in a cubic close packed array.

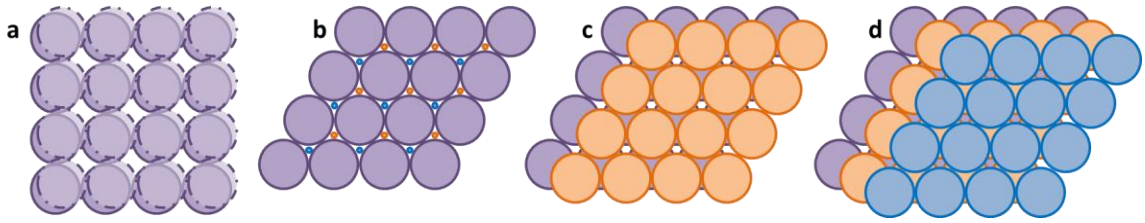

Figure 1.1 a) simple cubic packing of purple spheres with the second layer using dashed outlines and slightly offset for visual purposes, b) close packed array of purple spheres with different positions marked with orange and blue spheres for the next layer stacking, c) AB... stacking sequence for hexagonal close packing, d) ABC... stacking sequence for cubic close packing.

1.1.2 Coordination Environments in Solid Materials

For the above close packed stacking sequences, two different interstitial sites are available: octahedral and tetrahedral. Figure 1.2 indicates where these interstitial sites are located in a close packed array. The tetrahedral interstitial site has one atom from the first layer and three atoms from the second layer surrounding it. The octahedral interstitial site has three atoms from the first layer and three atoms from the second layer surrounding it. These stacking sequences and coordination environments are necessary to understand in order to build both simple and complex structures; however, multiple stacking sequences can be present which creates different coordination environments for the atoms.

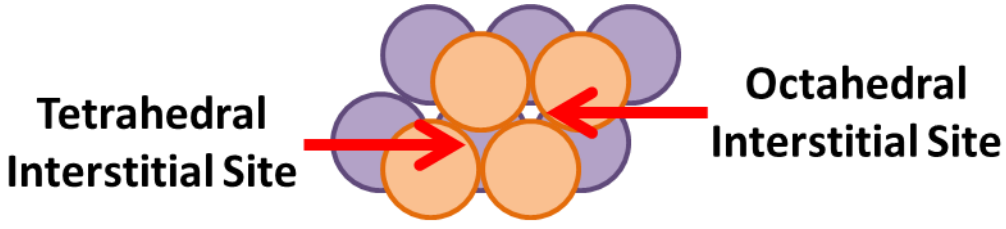

Figure 1.2 Location of interstitial sites in close packed arrays.

When the stacking sequences become more complex than the simple descriptions above, different coordination environments are created for the interstitial sites. The interstitial in Figure 1.1a is an eight coordinate environment. If a layer repeats itself in the close packing cases such as ABBA…, a trigonal prismatic coordination is realized for the interstitial site (Figure 1.3). Basic solid state crystal structures are generally built from close packed layers of anions which create these different interstitial environments for the cations to fill. The right image in Figure 1.3 indicates a close packing of red spheres with ABBA… stacking, with octahedral interstitial sites created between the AB layers and trigonal prismatic sites created between the BB layers. The octahedral sites are filled by the green and light blue atoms and the trigonal prismatic site is filled by a light yellow atom.

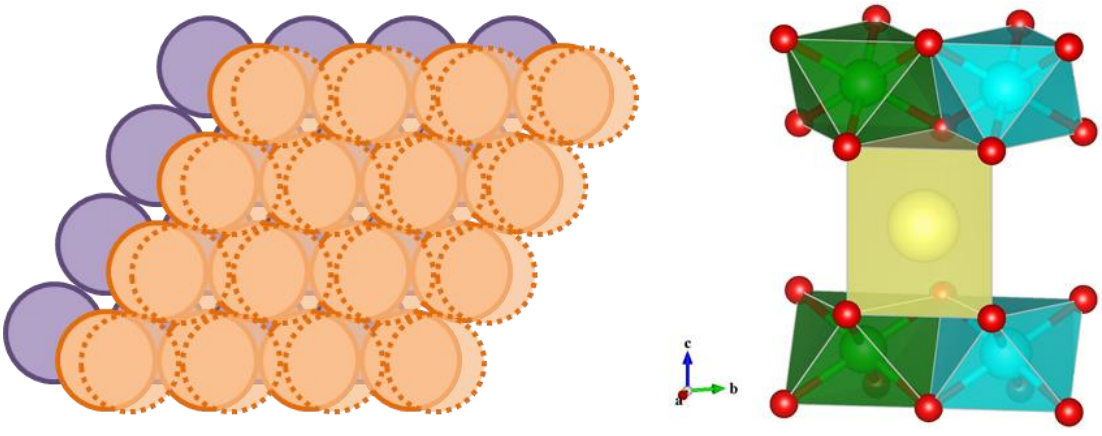

Figure 1.3 Illustration of ABBA… stacking sequence (orange spheres left image, red spheres right image), the second B layer has dashed outlines and is offset for visual purposes but in reality is directly above the first orange B layer.

1.1.3 Basic Layered Structures

Structures as the right image of Figure 1.3 are built from a close packing of the anions with cations filling the interstitial sites. Two of the most basic layered structures are $CdCl_2$ and CdI_2. A cubic stacking sequence produces $CdCl_2$ and a hexagonal stacking sequence produces CdI_2. These two structures can be used as starting models for layered compounds and are shown in Figure 1.4. It is noticed that the octahedra in the layers lie on a face and are edge sharing in both structures, also only every other layer between the anions is filled with cadmium (i.e, only ½ of the octahedra are filled with cations). The empty interlayer spaces produced from oxygen stacking is also octahedral coordination.[1] When all octahedra are filled, NaCl and NiAs structures are formed. It is also interesting to note that in the layered structures of Figure 1.4, the octahedra are oriented in the same direction for $CdCl_2$, whereas for CdI_2 every other layer is oriented in the opposite direction. Although these two materials are not the same composition, this different stacking orientation of the layers can be seen within one composition.

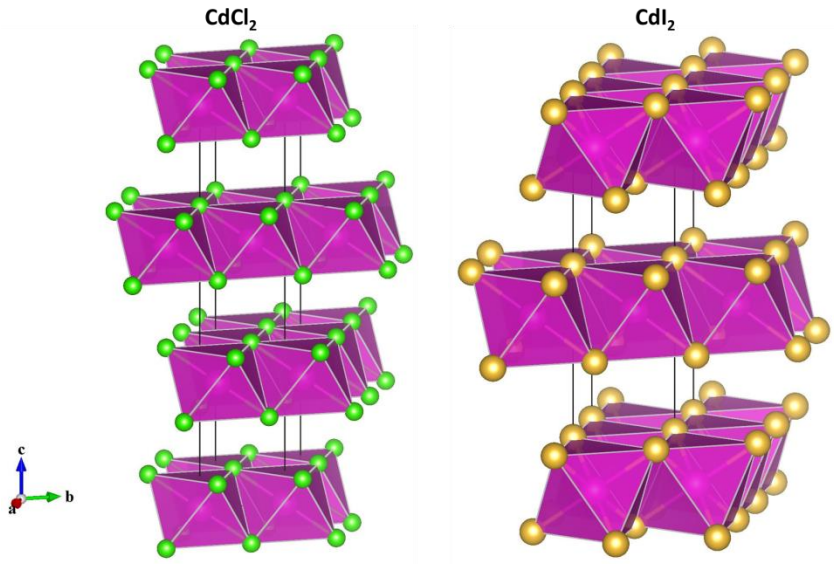

Figure 1.4 Structures of $CdCl_2$ (left; ICSD 38116) and CdI_2 (right; ICSD 86440).

Another simple layered structure is TiS_2, which has a hexagonal close packed structure similar to that of CdI_2. The most important feature of this compound is its ability to undergo intercalation of cations into the empty sulfide layers. A notation can be introduced to help explain the stacking sequences. As TiS_2 is a hexagonal close packed structure the sulfide atoms can be considered to stack in an ACAC… sequence. Since titanium only fills the octahedral spaces in every other layer of sulfide stacking the sequence is now AbCAbC…, where the lower case letter indicates the cation layers. When this material undergoes intercalation of other species, i.e., alkali cations, the stacking sequence can now be described as AbC(b)AbC, where the parentheses indicate the layer of inserted species.[2] It was found that upon insertion of lithium, this material remained single phase over all compositions of Li_xTiS_2 and this was one of the first examples of using the reversibility of intercalation into layered compounds for use in electrochemical cells.[3]

1.1.4 Bonding in Transition Metals

It is important to discuss the interaction of transition metals with their ligands when they are in different coordination environments. Crystal field theory first explains that the degeneracy of the five *d* orbitals of transition metals is removed upon placing ligands around the metals. In crystal field theory, ligands are considered point negative charges which will cause repulsion with the metal electrons in the orbitals that are along the bonding axes. It is helpful to see the orientations of the *d* orbitals which are shown in Figure 1.5. The first and middle images of Figure 1.6 indicate the splitting of the orbitals due to crystal field theory. The d_z^2 and $d_{x^2-y^2}$ orbitals lie directly on the axes where the ligands can be found and this interaction pushes these two orbitals up in energy while the other three are in a lower energy. Although some transition metals can be in other coordination, tetrahedral or trigonal prismatic, the octahedral coordination is most important to this dissertation.

Further splitting of the orbitals in an octahedral coordination can occur when the electron filling results in an unequal filling of the upper two orbitals. The middle image is filled with a d^9 configuration (i.e., Cu^{2+}). This along with d^4 electron counts can result in what is referred to as Jahn-Teller distortion. Jahn-Teller elongation is depicted in the right image of Figure 1.6. In this case, the d_z^2 orbital is full having two electrons. This orbital along with the d_{xz} and d_{yz} longer bond lengths between the metal and the ligand along the *z*-axis, therefore, these orbitals are lowered in energy because of less repulsion between the electrons on the metal and the

electrons on the ligand. The $d_{x^2-y^2}$ and d_{xy} orbitals are increased in energy because the equatorial ligands (along *x* and *y* axes) have a higher degree of overlap because the $d_{x^2-y^2}$ orbital is only half filled. The metal and ligand orbital overlap shortens the bond length and creates a high repulsive force between these orbitals and the ligands. This removes the degeneracy of these orbitals further as they are increased in energy because of this repulsion. The Jahn-Teller distortion can also cause axial compression but this configuration is less common.

The removal of degeneracy in the *d* orbitals correlates to the physical properties realized in a structure: optical spectra, thermodynamic and magnetic properties. A discussion of physical properties can be found in Chapter 2.

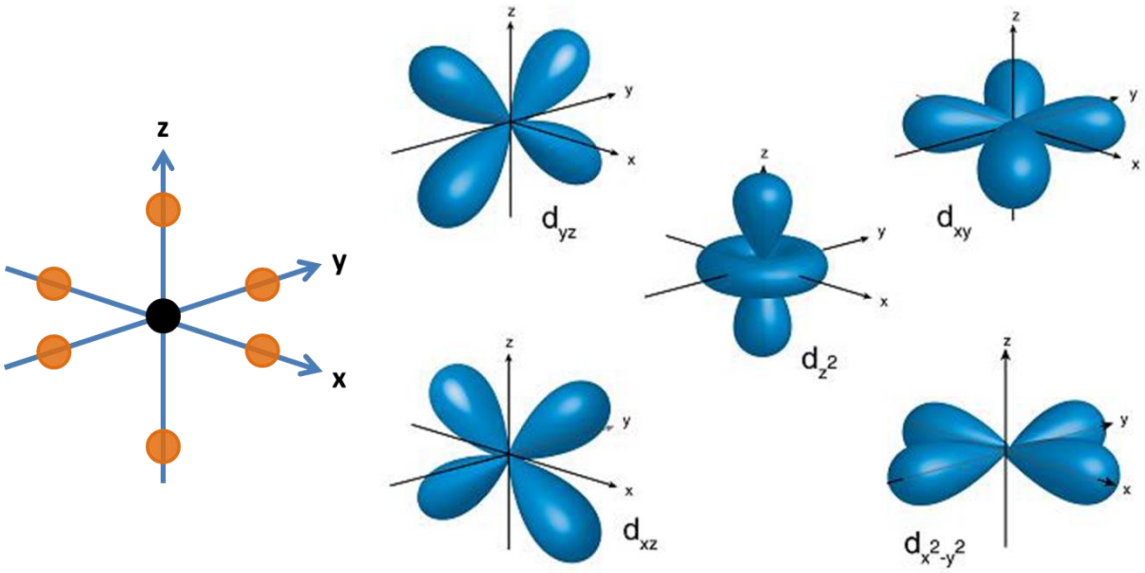

Figure 1.5 Left image, location of orange ligands around the black central atom for octahedral configuration. Right, the orientation of *d*-orbital probability lobes, Adapted from Wikibooks [4].

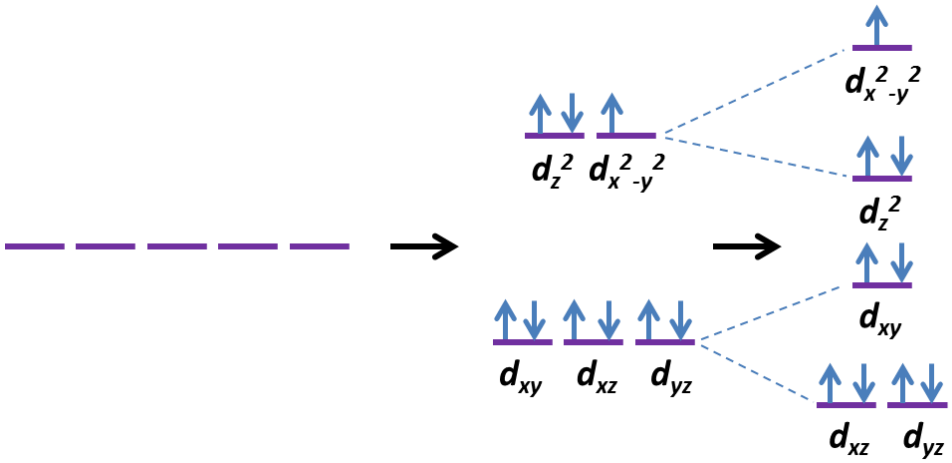

Figure 1.6 Splitting sequences of transition metal *d* orbital based on octahedral coordination of ligands. The middle image depicts a regular octahedral coordination and the right image depicts Jahn-Teller elongation resulting from certain electron configurations of the transition metals.

1.2 Ternary Layered Oxides

Building from the basic layered structures and considering the application of intercalation chemistry to these structures, many layered oxides have become popular research topics. Layered ternary oxides AMO_2, where M is a transition metal and A an alkali, include a wide number of compounds that have been extensively studied because of their remarkable chemical and physical properties. As alkali ions can be reversibly deintercalated from the layered structure, the main interest is in their electrochemical behavior as positive electrode materials for lithium-ion or sodium-ion batteries.[5–11] $LiCoO_2$ is nowadays the reference oxide for positive electrode materials of lithium batteries.[10,11] The reports of other interesting physical behaviors have focused the interest of the scientific community on these layered alkali-transition metal oxides. For example, the layered ternary

oxide system P2-Na_xCoO_2 has been intensively studied in the past as it exhibits various remarkable properties, such as its electrochemical behavior as a positive electrode of sodium batteries,[12–15] interesting thermoelectric properties for high sodium content,[16–18] or even superconductivity for hydrated $Na_xCoO_2 \bullet yH_2O$ phases.[19] The lamellar structure is one of the key points to explain all these wide range of physical properties.

1.2.1 Stacking Sequences

In the case of Na_xCoO_2, it is described as a stacking of edge-shared CoO_6 octahedra layers forming CoO_2 slabs between which Na^+ cations are intercalated in trigonal prismatic sites. As two slabs are necessary to fully describe the stacking in the hexagonal unit cell, the prefix P2 is added according to a general nomenclature to differentiate all the distinct stacking available for layered ternary oxides AMO_2.[20] In this structure the CoO_2 slabs are not oriented in the same direction, the second layer is rotated by π/3 or 60° compared to the first (Figure 1.7, left).[13] The P2 arrangement occurs when $x \approx 0.7$ and the oxygen stacking sequence is ABBA… and described by the space group $P6_3/mmc$. Another stacking sequence for Na_xCoO_2 is the P3, where there are now three CoO_2 slabs required to describe the unit cell (Figure 1.7, right). This structure is stable for $x \approx 0.5$ and has a ABBCCA… oxygen packing sequence with space group $R\text{-}3m$. In this case, all the CoO_2 slabs are oriented in the same direction upon stacking.

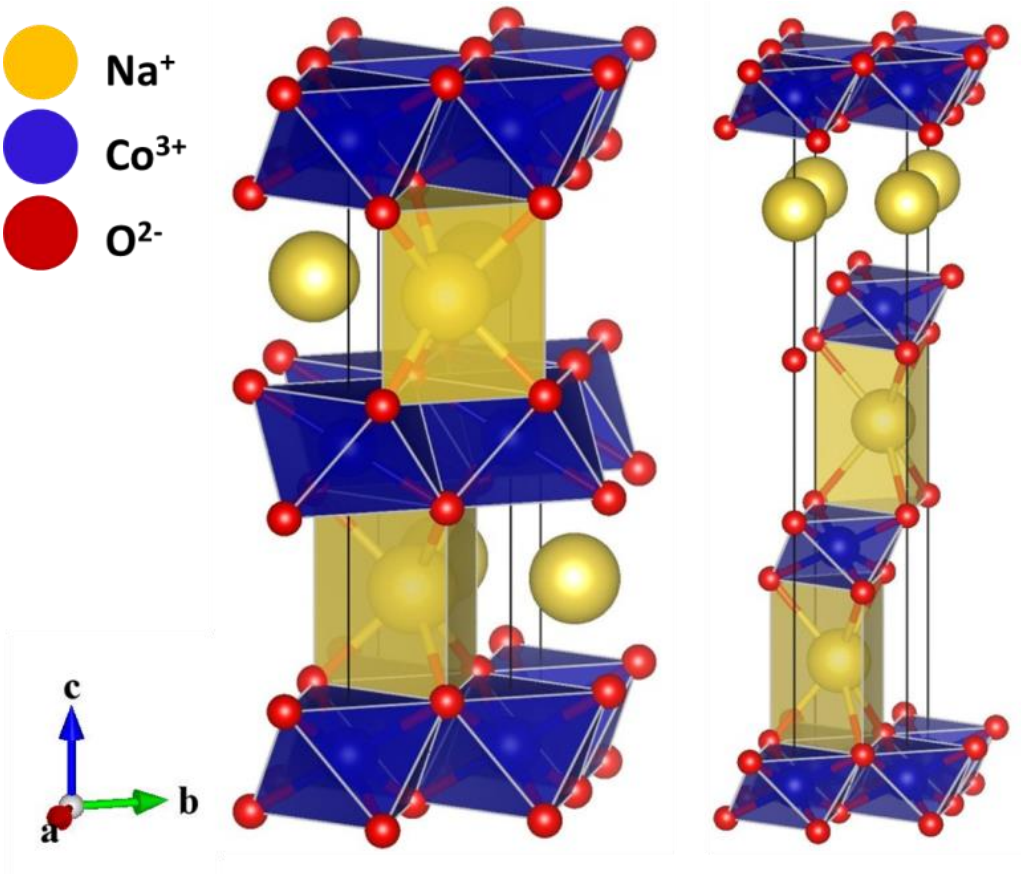

Figure 1.7 The P2 (left) and the P3 stacking arrangement (right) of Na_xCoO_2 ($x \leq 1$).

If the oxygen anion layers are arranged in a cubic close packed fashion ABCABC…, the interlayer sites are now an octahedral coordination. This is the structure adopted by α-$NaFeO_2$ (Figure 1.8, left). This structure is labelled as O3 indicating the interlayer sites are octahedral and three layers of FeO_2 slabs are required to describe the unit cell. Upon ion exchange of the sodium in P3 Na_xCoO_2 with lithium, a slab gliding process occurs and forms the O3 structure which is adopted by $LiCoO_2$ (Figure 1.8, right). Both of these compounds crystallize in the *R*-3*m* space group and have the same MO_2 slab orientation as that for the P3-Na_xCoO_2 compound. It is also possible to for an O2 structure of $LiCoO_2$ via ion exchange;

however, the starting structure must be the P2-Na_xCoO_2. Due to the different orientations of the octahedra in the second slab, metal – oxygen bonds would have to be broken to go from the P3 to O2 or from P2 to O3 structures. In both of these O3 structures, it is possible to electrochemically deintercalate the interlayer cations (Na^+ or Li^+) which causes a monoclinic distortion of the unit cell (Figure 1.8, right). Since the deintercalation process is reversible, this distortion helps stabilize the metal slabs when the interlayer cation content is reduced. The monoclinic unit cell is shown in the right image of Figure 1.8 for $Li_{0.5}CoO_2$. This compound could be described as a hexagonal unit cell which would require three CoO_2 slabs therefore; the monoclinic distortion is still noted as O3.

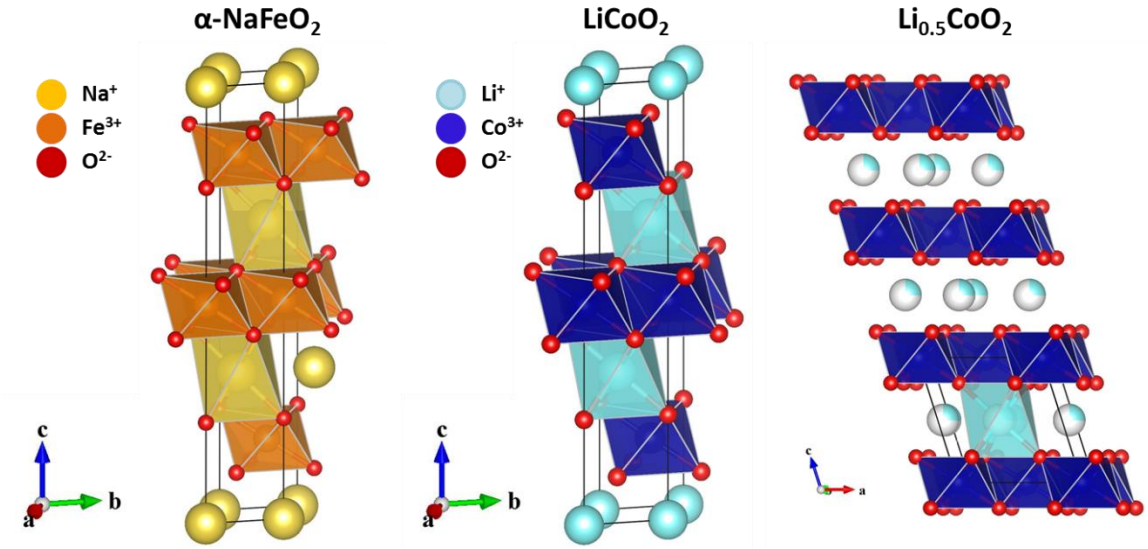

Figure 1.8 Structures of α-$NaFeO_2$ (left), $LiCoO_2$ (middle) and $Li_{0.5}CoO_2$ (right). The interlayer cations are in octahedra coordination and there are three metal-oxygen slabs required to describe the hexagonal unit cell in all cases. The unit cells are shown as solid black lines. The spheres representing Li^+ in the far right image are incompletely colored because there is only partial filling of the layers for this stoichiometry.

1.2.2 Rise of Stacking Defects

As described above, there are multiple stacking sequences for layered materials creating the different polytypes of these compounds.[21] If a structure is not in the regular O3 stacking with the *R*-3*m* space group then commonly one of the three space groups, $P3_112$, *C* 2/*m* or *C* 2/*c*, are used to describe the unit cell. Bréger et al. applied first principles calculations for each stacking variant in Li_2MnO_3, i.e. $Li_3LiMn_2O_6$ a layered structure, and found that all stacking variations have very close energies with the monoclinic space groups only having a 2 meV difference.[22] Since there are multiple stacking sequences available for these layered materials, stacking faults, or a disruption in the layering sequence, are common. A disruption of the layering scheme can be described by going from an ABCABA… to an ABCABABC… stacking sequence. In the second sequence, one C layer is missing and/or has slipped to be in the A position. The disruption only affects the structure along the stacking directions keeping order in the layers. Generally, the structure can go on in the regular sequence after the disruption but this does have effects on the XRD patterns, peak broadening or peak intensity differences from the calculated patterns.

1.3 Expanded Compositions Containing Honeycomb Ordering

While keeping the general layered structure of the AMO_2 compounds, a large number of other compounds have been reported in the literature by substituting the M cation with another X cation. Specifically when only 1/3 of M is substituted by X,

the general formula is expanded to $A_2M_2XO_6$ and $A_3M_2XO_6$, where M is now a 2+ cation and the A content is dependent on the oxidation state of the X cation (usually 5+ or 6+). These specific compositions sometimes lead to an M/X cationic ordering within the slab where each XO_6 octahedron is surrounded by six MO_6 octahedra forming a honeycomb network. The octahedra in the slabs are still edge sharing as shown for the simpler structures above and this honeycomb ordering occurs so that the XO_6 octahedra are not sharing edges with each other according to Pauling's rules.[23] Many compositions have already been reported in the literature: $A_3M_2XO_6$ (A^+ = Na, Li; X^{5+} = Sb, Bi, Nb, Ta, Ru) or $A_2M_2TeO_6$ (M^{2+} = Co, Cu, Mg, Zn, Ni).[24–43] This honeycomb superstructure is also found in other layered phases with different cationic charges, A_2MO_3 (i.e., $AM^{4+}{}_{2/3}A^{+}{}_{1/3}O_2$),[44–47] A_5XO_6 (i.e., $AA^{+}{}_{2/3}X^{7+}{}_{1/3}O_2$)[48,49], Cu_5SbO_6[35] and $Na_3M^{2+}Ir_2O_6$ or $Na_3M_2{}^{3+}IrO_6$.[50–52] Many of these compounds crystallize in a monoclinic *C*2/*m* or *C*2/*c* unit cell but are still classified as O3 compounds because it takes 3 honeycomb layers to describe the unit cell in a hexagonal setting. A full review of honeycomb ordered layered structures is not available to date however; Chapter 3 provides a review of the layered honeycomb ordered compounds containing Sb^{5+}, Bi^{5+} and Te^{6+}.

1.4 References

[1] F. Hulliger, Structural Chemistry of Layer-Type Phases, D. Reidel Publishing Company, Dordrecht, Holland, 1976.
[2] P.G. Bruce, Solid State Electrochemistry, Cambridge University Press, Cambridge, 1995.
[3] A.K. Cheetham, P. Day, Solid State Chemistry Compounds, Oxford University Press, New York, 1992.
[4] Wikibooks, High Sch. Chem. At. Orbitals (2014).

[5] K. Mizushima, P.C. Jones, P.J. Wiseman, J.B. Goodenough, Mater. Res. Bull. 15 (1980) 783.
[6] J.-J. Braconnier, C. Delmas, C. Fouassier, P. Hagenmuller, Mater. Res. Bull. 15 (1980) 1797.
[7] C. Delmas, J.-J. Braconnier, C. Fouassier, P. Hagenmuller, Solid State Ion. 3–4 (1981) 165.
[8] R. Berthelot, D. Carlier, C. Delmas, Nat. Mater. 10 (2011) 74.
[9] Y. Takeda, K. Nakahara, M. Nishijima, N. Imanishi, O. Yamamoto, M. Takano, R. Kanno, Mater. Res. Bull. 29 (1994) 659.
[10] J.M. Tarascon, M. Armand, Nature 414 (2001) 359.
[11] M. Armand, J.-M. Tarascon, Nature 451 (2008) 652.
[12] J.-J. Braconnier, C. Delmas, C. Fouassier, P. Hagenmuller, Mater. Res. Bull. 15 (1980) 1797.
[13] C. Delmas, J.-J. Braconnier, C. Fouassier, P. Hagenmuller, Solid State Ion. 3–4 (1981) 165.
[14] L.W. Shacklette, T.R. Jow, L. Townsend, J. Electrochem. Soc. 135 (1988) 2669.
[15] R. Berthelot, D. Carlier, C. Delmas, Nat. Mater. 10 (2011) 74.
[16] I. Terasaki, Y. Sasago, K. Uchinokura, Phys. Rev. B 56 (1997) R12685.
[17] M. Lee, L. Viciu, L. Li, Y. Wang, M.L. Foo, S. Watauchi, R.A. Pascal Jr, R.J. Cava, N.P. Ong, Nat. Mater. 5 (2006) 537.
[18] M. Lee, L. Viciu, L. Li, Y. Wang, M.L. Foo, S. Watauchi, R.A. Pascal Jr., R.J. Cava, N.P. Ong, Phys. B Condens. Matter 403 (2008) 1564.
[19] K. Takada, H. Sakurai, E. Takayama-Muromachi, F. Izumi, R.A. Dilanian, T. Sasaki, Nature 422 (2003) 53.
[20] C. Delmas, C. Fouassier, P. Hagenmuller, Phys. BC 99 (1980) 81.
[21] A.R. West, Basic Solid State Chemistry, John Wiley & Sons, Chichester, 1999.
[22] J. Bréger, M. Jiang, N. Dupré, Y.S. Meng, Y. Shao-Horn, G. Ceder, C.P. Grey, J. Solid State Chem. 178 (2005) 2575.
[23] L. Pauling, J. Am. Chem. Soc. 51 (1929) 1010.
[24] C. Greaves, S.M.A. Katib, Mater. Res. Bull. 25 (1990) 1175.
[25] J.M.S. Skakle, M.A. Castellanos R., S.T. Tovar, A.R. West, J. Solid State Chem. 131 (1997) 115.
[26] G.C. Mather, R.I. Smith, J.M.S. Skakle, J.G. Fletcher, M.A. Castellanos R, M.P. Gutierrez, A.R. West, J. Mater. Chem. 5 (1995) 1177.
[27] G.C. Mather, C. Dussarrat, J. Etourneau, A.R. West, J. Mater. Chem. 10 (2000) 2219.
[28] R. Nagarajan, S. Uma, M.K. Jayaraj, J. Tate, A.W. Sleight, Solid State Sci. 4 (2002) 787.
[29] O.A. Smirnova, V.B. Nalbandyan, A.A. Petrenko, M. Avdeev, J. Solid State Chem. 178 (2005) 1165.
[30] O.A. Smirnova, M. Avdeev, V.B. Nalbandyan, V.V. Kharton, F.M.B. Marques, Mater. Res. Bull. 41 (2006) 1056.
[31] Y. Miura, R. Hirai, T. Fujita, Y. Kobayashi, M. Sato, J. Magn. Magn. Mater. 310 (2007) e389.
[32] L. Viciu, Q. Huang, E. Morosan, H.W. Zandbergen, N.I. Greenbaum, T. McQueen, R.J. Cava, J. Solid State Chem. 180 (2007) 1060.
[33] S. Derakhshan, J.E. Greedan, T. Katsumata, L.M.D. Cranswick, Chem. Mater. 20 (2008) 5714.
[34] V.V. Politaev, V.B. Nalbandyan, A.A. Petrenko, I.L. Shukaev, V.A. Volotchaev, B.S. Medvedev, J. Solid State Chem. 183 (2010) 684.

[35] E. Climent-Pascual, P. Norby, N.H. Andersen, P.W. Stephens, H.W. Zandbergen, J. Larsen, R.J. Cava, Inorg. Chem. 51 (2011) 557.
[36] M.A. Evstigneeva, V.B. Nalbandyan, A.A. Petrenko, B.S. Medvedev, A.A. Kataev, Chem. Mater. 23 (2011) 1174.
[37] E.A. Zvereva, M.A. Evstigneeva, V.B. Nalbandyan, O.A. Savelieva, S.A. Ibragimov, O.S. Volkova, L.I. Medvedeva, A.N. Vasiliev, R. Klingeler, B. Buechner, Dalton Trans. 41 (2012) 572.
[38] R. Berthelot, W. Schmidt, S. Muir, J. Eilertsen, L. Etienne, A.W. Sleight, M.A. Subramanian, Inorg. Chem. 51 (2012) 5377.
[39] R. Berthelot, W. Schmidt, A.W. Sleight, M.A. Subramanian, J. Solid State Chem. 196 (2012) 225.
[40] V. Kumar, N. Bhardwaj, N. Tomar, V. Thakral, S. Uma, Inorg. Chem. 51 (2012) 10471.
[41] V.B. Nalbandyan, M. Avdeev, M.A. Evstigneeva, J. Solid State Chem. 199 (2013) 62.
[42] V.B. Nalbandyan, A.A. Petrenko, M.A. Evstigneeva, Solid State Ion. 233 (2013) 7.
[43] E.A. Zvereva, O.A. Savelieva, Y.D. Titov, M.A. Evstigneeva, V.B. Nalbandyan, C.N. Kao, J.-Y. Lin, I.A. Presniakov, A.V. Sobolev, S.A. Ibragimov, M. Abdel-Hafiez, Y. Krupskaya, C. Jähne, G. Tan, R. Klingeler, B. Büchner, A.N. Vasiliev, Dalton Trans. 42 (2013) 1550.
[44] P. Strobel, B. Lambert-Andron, J. Solid State Chem. 75 (1988) 90.
[45] A.C.W.P. James, J.B. Goodenough, J. Solid State Chem. 74 (1988) 287.
[46] M.J. O'Malley, H. Verweij, P.M. Woodward, J. Solid State Chem. 181 (2008) 1803.
[47] K. Kataoka, Y. Takahashi, N. Kijima, H. Nagai, J. Akimoto, Y. Idemoto, K. Ohshima, Mater. Res. Bull. 44 (2009) 168.
[48] T. Betz, Z Anorg Allg Chem 512 (1984) 19.
[49] L.R. Morss, E.H. Appelman, R.R. Gerz, D. Martin-Rovet, J. Alloys Compd. 203 (1994) 289.
[50] Y. Singh, P. Gegenwart, Phys. Rev. B 82 (2010) 064412.
[51] S.K. Choi, R. Coldea, A.N. Kolmogorov, T. Lancaster, I.I. Mazin, S.J. Blundell, P.G. Radaelli, Y. Singh, P. Gegenwart, K.R. Choi, S.-W. Cheong, P.J. Baker, C. Stock, J. Taylor, Phys. Rev. Lett. 108 (2012).
[52] K. Baroudi, C. Yim, H. Wu, Q. Huang, J.H. Roudebush, E. Vavilova, H.-J. Grafe, V. Kataev, B. Buechner, H. Ji, C. Kuo, Z. Hu, T.-W. Pi, C. Pao, J. Lee, D. Mikhailova, L. Hao Tjeng, R.J. Cava, J. Solid State Chem. 210 (2014) 195.

Chapter 2

Fundamentals of Solid State Synthesis and Material Properties

This chapter will server to introduce the fundamentals of solid state synthesis, material properties and the characterization techniques used throughout this work.

2.1 Solid State Synthesis Methods

Conventional solid state synthesis uses powdered starting reagents intimately mixed together, pressed into pellets and fired in a furnace. The temperature of the reaction depends on the desired product and on the properties of the starting reagents. Multiple grinding and heating steps may be required to achieve the desired product due to the slow nature of this synthesis process. This method relies on the movement of atoms between the starting materials to form the product. The grinding process using a mortar and pestle can never achieve atomic level mixing, therefore, regrinding breaks up the interfaces between the product and left over starting materials that are left at the core of the particles. A cartoon of this process is shown in Figure 2.1. Upon first reaction, starting reagents will diffuse into one another, a slow process dependent on the mobility of ions between one another to form the product. Initial products will have cores of starting reagent and outer shells of product. Regrinding these particles creates new

interfaces for reaction between the starting reagents and the previously formed product acts as a guide for these materials to form the desired products.

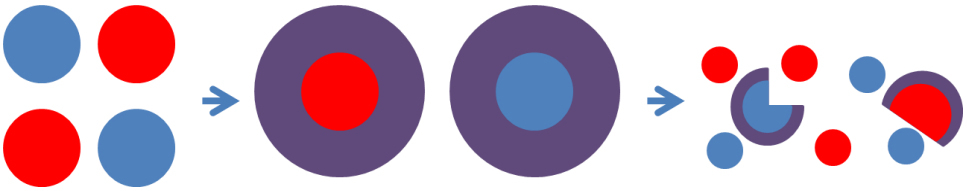

Figure 2.1 Red and blue spheres represent starting reagents for conventional solid state synthesis of the purple product. Product formation occurs through diffusion at the surface of particles, which are broken up (far right) to allow further reaction.

Reactivity, volatility and structure of the starting materials must be considered when preparing to synthesize desired compounds. Materials such as Al_2O_3 are highly inert and require elevated temperatures for reaction whereas Li_2CO_3 or Na_2O are volatile at higher temperatures and could be lost during a reaction.[1] In this work, volatile carbonate starting reagents were used and to accommodate for loss during heating, 5 – 7.5% excess were mixed at the onset of the synthesis without further need for additional reagent upon multiple heating steps. Reactants such as Bi_2O_3 and Sb_2O_3 were also used but evaporation of these more volatile reagents was not observed at synthesis temperatures. The reactivity of the materials with the reaction vessel holding the materials in the furnace must also be considered. Alumina crucibles are commonly used as reaction vessels but if the starting materials are incompatible, Au or Pt trays can be used as the reaction containers.

In some cases desired products cannot be prepared with conventional methods of grinding, heating and cooling back to room temperature. These

products or phases are called metastable, which is the state between unstable products and stable products. Stability of a phase at constant temperature and pressure is measured by its Gibbs free energy (G). When the Gibbs free energy of a system is at a minimum (or dG = 0), a phase is in an equilibrium state and is stable.[2] Figure 2.2 shows an example of a thermodynamic stability plot of phases A and B. Although both phases lie at a minimum G, phase A is still at a higher energy than B. Since B is the lowest energy, it will be the most stable phase formed. Phase A is the metastable state which can be produced either by nontraditional methods: quenching a material from a high temperature or performing lower temperature ion exchange reactions.

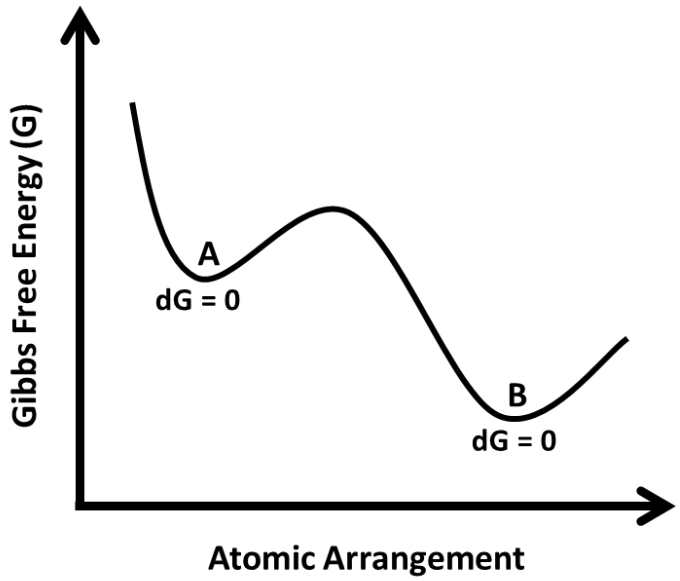

Figure 2.2 Gibbs free energy plot of phases A and B.

Molten salt ion exchange can be used to obtain metastable products and can be a low temperature process depending on the melting point of the salt used for

the exchange. A first consideration of molten salt ion exchange is that the structure must allow for ions to be exchanged. Secondly, usually a nitrate salt (or salt with low melting temperature) of the desired metal for exchange is intimately ground, in excess, with the solid material in which the exchange will occur. Smaller particle sizes will allow for better exchange efficiency just as in conventional solid state synthesis. This mixture is then heated to or slightly above the melting temperature of the metal salt, where the metal from the molten salt will diffuse through and push out the original metal in the structure. The removed metal ions are now part of the molten mixture outside of the solid structure. The excess metal salt can then be easily washed away and a new solid structure can be collected. This reaction is considered a topotactic reaction as the interlayer cations are exchanged and the host structure retains its integrity but may undergo a simple transition to accommodate the new ions. In this work, molten salt ion exchange was employed to obtain new compositions.

Electrochemical intercalation can also be used to obtain metastable products and allows for strict control over the desired stoichiometry, which is not always possible with conventional solid state methods. Intercalation or deintercalation is the process of introducing or removing a guest species (i.e., interlayer cations) into a solid lattice without any major adjustments of the host structure.[3] This method implements the starting material in an electrochemical cell and when a voltage is applied, the mobile cations will be removed from the structure and a nonstoichiometric product can be characterized. The fine adjustment of interlayer

species can impact the physical properties, electronic or magnetic, properties of the material.

The ease with which these two nontraditional techniques can occur depends greatly on the starting compound or the host structure. The channels or bottlenecks that the ions must pass through affect the rate and efficiency of these reactions. This is a structure dependent issue and it is known that faster diffusion of ions can occur from trigonal prismatic coordination (rectangular window) than from an octahedral coordination (trigonal window)[4], Figure 2.3a-b.

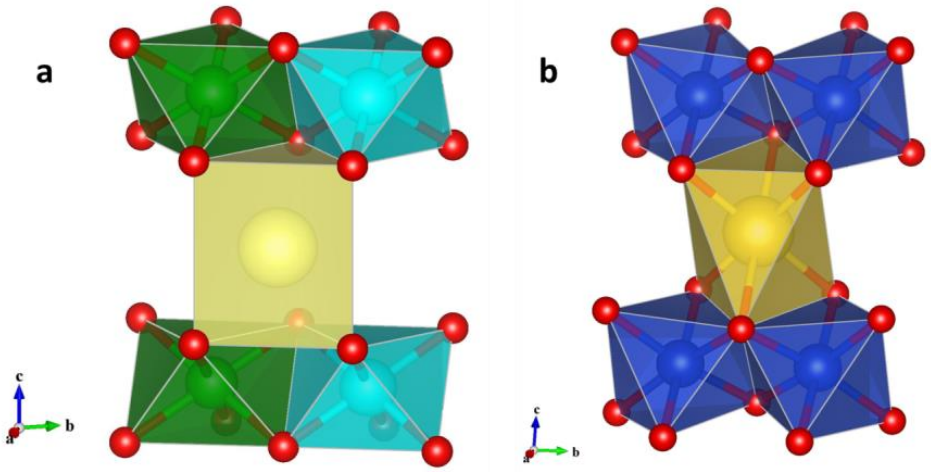

Figure 2.3 a) Illustration of rectangular window for ion diffusion when the light yellow ion is in trigonal prismatic coordination and b) the trigonal window available when the yellow ion is in an octahedral coordination.

2.2 Powder X-ray Diffraction

Although we have recently passed the 100th anniversary of Bragg's Law, discovered in 1912 and the Nobel Prize awarded in 1915, we are in the midst of the 100 year mark for when crystallography became the most useful technique for

structure determination. The work of this father and son team were able to describe the necessary conditions for diffraction in a simple manner than the Laue method.[5]

X-ray diffraction requires an X-ray tube (the source), sample stage and detector. The source consists of a metal target (anode) and an electron generator (cathode). A high voltage is applied to the cathode and electrons are quickly forced to the metal target. This rapid impact and deceleration of the electrons at the target causes a continuous spectrum of white radiation to be emitted in all directions. If the voltage of the tube is high enough, characteristic wavelengths to the metal target can be used. The K radiation lines are of the most interest for X-ray diffraction because they are the shortest wavelength and have the highest energy to detect. The wavelengths of X-rays (0.1 Å to 100 Å) are on the order of atomic distances depending on the source which is necessary when analyzing atomic positions and lattice parameters of materials. These occur when an electron from the K shell (*s* electrons) is knocked out by the impact of an electron. When the vacancy is filled from the outer shells (2*p* or 3*p* electrons), Kα and Kβ lines are produced. For experiments, the Kβ line is filtered out because the Kα is a stronger line and occurs more frequently. The Kα line is still a doublet of Kα1 and Kα2 because the transition from the 2*p* has two possible spin states relative to the *s* orbital it is filling. Once the characteristic wavelength is obtained, it is focused out of the source through beryllium windows on the tube onto the sample where the X-rays are diffracted to the detector.

X-rays are scattered by the electron cloud of an atom which makes X-ray diffraction sensitive to the elemental composition of a sample. The scattering of X-rays by an atom is directly related to the atomic number of the atom. In a crystal or polycrystalline material, the atoms sit in the planes of the unit cell. For diffraction to occur, Bragg's Law must be obeyed. Figure 2.4, shows the necessary relations used to derive Bragg's Law. They described a material as built up in layers where some of the radiation will be reflected at an angle equal to that of the incident radiation but other incident beams will transmit through the sample and reflected by other layers. The spacing between these layers is called the *d*-spacing which has the relation, $\lambda = 2d\sin\theta$, where λ is the wavelength of the radiation and θ is the angle between the plane and the incident and reflected beam. Diffraction occurs when the incident and reflected beams are in phase with one another. If an X-ray is reflected at an angle different than the incident angle, the waves are out of phase and destructive interference.

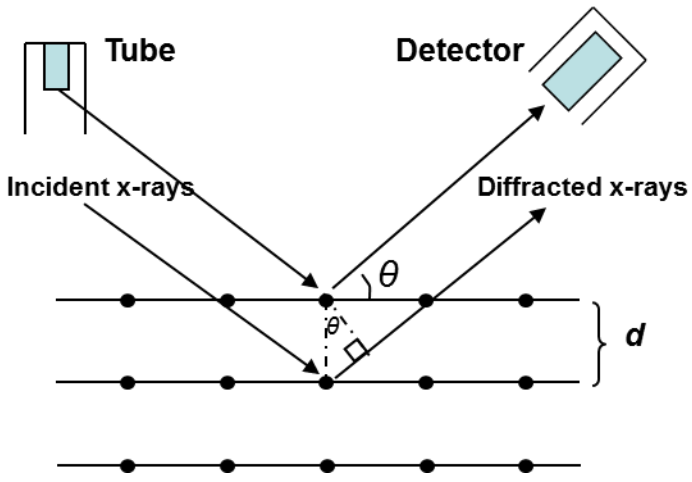

Figure 2.4 Relationship of incident and diffracted beams for derivation of Bragg's Law and the relation to *d*-spacing in a unit cell.

The resulting diffraction pattern collected at the detector can be used to calculate the unit cell parameters, the atomic positions of the elements in the crystal lattice and determine the structure of a compound. The raw data were analyzed using the Jade 8.0 program with access to the International Center for Diffraction Data (ICDD) databases. This program was used for phase identification and conversion of the raw data from the Rigaku software to useable .dat files. The .dat files can be used directly with the Full Prof suite equipped with WinPLOTR[6,7] or converted to a format that can be used with GSAS equipped with EXPGUI.[8,9] These two programs were used to obtain a Le Bail fit of the PXRD patterns. This method doesn't require a structure model and the unit cell parameters, background and peak shapes can be refined.[10] This method gives a good estimate of the cell, profile intensities and background before attempting to fit a structure with the Rietveld method.[10,11] In this dissertation, the Le Bail method was used and cell parameters are reported however, due to structural defects causing highly irregular PXRD patterns, Rietveld refinement for full structural analysis was not performed.

2.3 Introduction to Magnetism and Magnetic Susceptibility Measurement Parameters

From Plato ca. 428 – 348 BC to now, magnetism has played an important role in society, whether philosophical or scientific understanding and application.[12] It is now understood that magnetic properties arise from unpaired electrons in the

valence orbitals of an atom, described as paramagentism. If an atom has no unpaired electrons in its valence shell, it is diamagnetic. In paramagnetic materials, the unpaired electron spins are oriented in a random way throughout a structure. If atoms are positioned in a structure that will allow for interactions between these spins, different phenomena can be seen: ferromagnetism, antiferromagentism or ferrimagnetism (Figure 2.5). In ferromagnetic materials, all of the spins are oriented in the same direction and result in an additive magnetic moment. For antiferromagnetic materials, the spins align antiparallel and essentially cancel out. These two phenomena occur at certain temperatures with the former labeled as T_C (Curie temperature) and the latter labeled as T_N (Néel temperature). Ferrimagnetism occurs when there is an antiparallel ordering of the spins however the magnitude of the spins are not the same and do not cancel out to zero.

Classification & orientation of magnetic moments	Critical temperature	Magnitude of χ_m	Temperature dependence of χ_m
Diamagnetic	None	-10^{-6} to -10^{-5}	
Paramagnetic 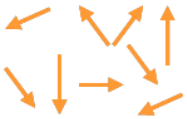	None	10^{-5} to 10^{-3}	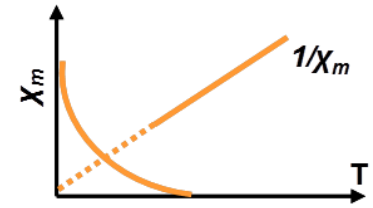
Ferromagnetic 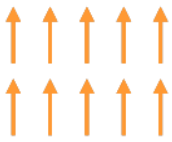	T_c Curie Temp. $\chi_m = C/(T - \theta)$	Large below T_c	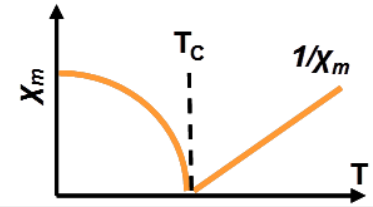
Anti - Ferromagnetic 	T_N Neel Temp. $\chi_m = C/(T \pm \theta)$	10^{-5} to 10^{-3}	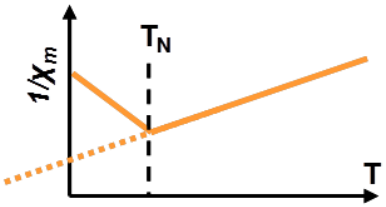
Ferrimagnetic 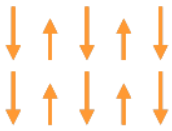	T_c Curie Temp. $\chi_m \approx C/(T - \theta)$	Large below T_c	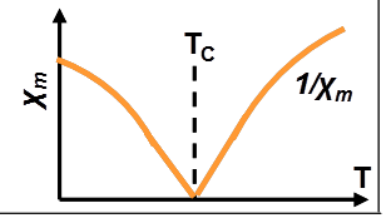

Figure 2.5 Representations of magnetic spin interactions as well as the magnetic susceptibility and inverse susceptibility vs. temperature plots expected from measurements. Adapted from J. P. Jakubovics [13].

In some cases, the coordination and organization of magnetic ions in a structure can lead to more complex behavior than those described by Figure 2.5.

Superexchange mechanisms can occur where the metal ions interact with their neighbors through their shared covalently bound ligand. A set of rules governing these interactions were described by Goodenough and Kanamori which are appropriately call the Goodenough-Kanamori rules.[14–17] When an M – O – M bond angle is 180°, due to the metal (M) *d* orbitals overlapping with the same *p* orbital of the oxygen, the unpaired electrons on the metal atoms must be antiferromagentically coupled through the oxygen (upper image of Figure 2.6). When the M – O – M bond angle is 90°, the *d* orbitals of the metals are overlapping with separate *p* orbitals on the oxygen and the unpaired spins on the metal atoms will most likely be ferromagentically coupled (lower image of Figure 2.6).

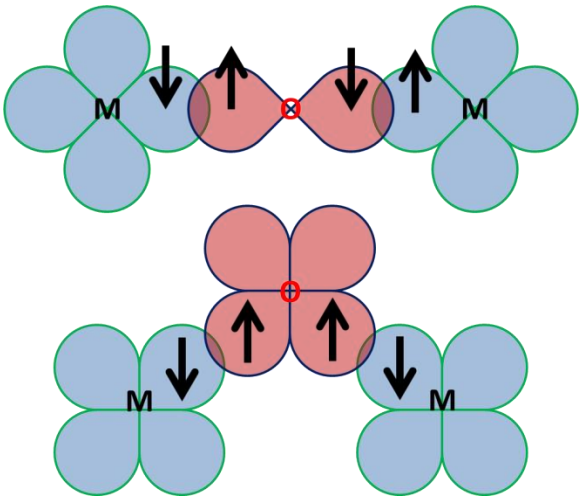

Figure 2.6 Magnetic superexchange interactions of metals (blue *d* orbitals) and ligand (oxygen, red *p* orbitals). Upper image depicts antiferromagnetic superexchange and the lower image depicts ferromagnetic superexchange.

Magnetic interactions in a materials can be measured and characterized by placing a sample in a magnetic field, *H*, and monitoring the interaction of the field

with the sample. The magnetic flux density, B, is related by the permeability of the material, μ, to the magnetic field by $B = \mu H$. The relation can be expanded to include the magnetization of the sample, M, using μ_0, the permeability of free space: $B = \mu_0 H + \mu_0 M$. The magnetic susceptibility is defined as the magnetization divided by the field, $\chi = M/H$. The susceptibility can be used to determine the magnetic behavior of a sample when the temperature or applied filed is varied.

The Curie law simply indicates that the magnetic susceptibility is inversely related to temperature by $\chi = C/T$, where C is the Curie constant and T is the temperature. This is obeyed when materials are paramagnetic and there is no interaction between the electrons in a material. When interactions are present in a material leading to ferromagnetism or antiferromagentism, the Curie-Weiss law, $\chi = C/T - \theta$, is better suited to fit the paramagnetic region and extrapolate the Weiss value, θ, to determine the identity of the magnetic interactions. When the inverse susceptibility vs. temperature is plotted, the x-intercept of the resulting line gives the Weiss constant value. A positive Weiss value indicates ferromagnetism and a negative value indicates antiferromagnetism. When this line crosses zero, the material is paramagnetic.

The magnetic moment, μ, of a material can be determined from the magnetic susceptibility. When the data is fit with the Curie-Weiss law, the magnetic moment of the sample is determined by $\mu = 2.84\sqrt{C}$. This experimental value can be compared to the theoretical value (μ_{Theor}) determined from the number of unpaired electrons present in the sample. The $\mu_{Theor} = g\sqrt{S(S+1)}$, where S is the sum of the

individual unpaired electrons and *g* is the gyromagnetic ratio which is approximated to 2.00. When a solid solution is formed, the total magnetic moment consists of the stoichiometric contribution of the present elements and their number of unpaired electrons. The theoretical moment can then be found by $\mu_{Total} = \sqrt{[(\mu_{Theor}A*x)+(\mu_{Theor}B*y)+\ldots]}$, where A and B are the magnetic ions and *x* and *y* are the stoichiometric amounts of each ion (i.e., A_xB_y). In the subsequent chapters, theoretical moments are compared to those determined from magnetic susceptibility experiments. Information is also gain at what kind of magnetic interactions these materials have.

2.4 Optical Properties in Materials

The optical properties of inorganic compounds are dependent on the electronic configuration of the material. The color along with knowledge of the composition and structure can aid in determining the electronic interactions within a material.

2.4.1 Light Interactions with Materials

When light interacts with a material, there are many different effects that can take place: specular reflection, diffuse reflection, absorption and/or transmission (Figure 2.7). In general, reflection is when incident light on a surface is returned with the same wavelength as what hit the surface. Specular reflection, the reflected light has the same angle as the incident light, occurs from smooth surfaces

and preserves the images being reflected or causes the visual effect of glare, sheen or luster.[18] Absorption causes the reflected light to have less intensity because some of the energy is absorbed by the material and the light that enters the sample doesn't leave. Transmission is when light passes directly through the sample and is only useful for measurement on non-opaque samples, such as thin films or single crystals. Diffuse reflection occurs when light is reflected in all directions from a surface. In a diffuse reflectance measurement, all of the light is collected except for the specular reflected light. Since polycrystalline materials have a rough surface, i.e., crystallites oriented in all directions, the sample will scatter light in all directions. The intensity of diffuse reflection is related to the incident intensity by Lambert's cosine law, i.e. $I = I_0 \text{Cos } \theta$, where I is the observed intensity, I_0 is the incident intensity and θ is the angle between the incident beam and path of radiant emission.[18,19]

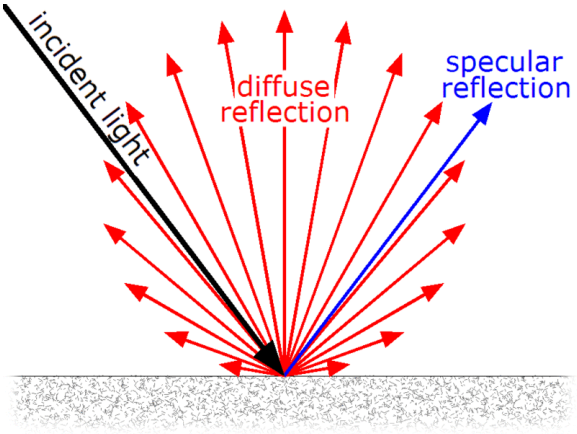

Figure 2.7 Picture of specular and diffuse reflection of light. Transmission and absorption are not shown. If absorption occurs in a sample, the intensity of the reflected light would be lowered. Adapted from GianniG46 [20].

2.4.2 Diffuse Reflectance Spectroscopy

Diffuse reflectance of a powder sample can be used to estimate the band gap energy. The collected UV-Vis diffuse reflectance data is converted to absorbance using the Kubelka-Munk relation, $f(R) = (1-R)^2/2R$, where R is the reflectance intensity for the sample collected from the instrument.[21] If a plot of absorbance [f(R)] vs. energy (eV) is made, the linear region can be extrapolated to the *x*-axis for estimation of the band gap energy (the energy separating the top of the valence band and bottom of the conduction band). The color transitions in the compounds investigated in this work lead to the interest in estimating the band gaps of these materials. These measurements were performed on a setup in Dr. McIntyre's lab in the Physics department at Oregon State University. Deuterium and halogen light sources are directed to the sample through a bifurcated fiber optic setup which collects the diffuse reflectance and carried it to an Ocean Optics CCD spectrometer.

2.5 Mössbauer Spectroscopy

It is common in chemistry to use the fact that an element possesses ground states and excited states. It has already been discussed that electronic transitions between these states produce X-rays beneficial for phase identification and structural analysis of compounds. In certain cases, nuclear transitions create gamma rays which can be utilized to determine the atomic oxidation state, the chemical environment and symmetry or the magnetic properties of the atom.

In 1957, Rudolf Mössbauer discovered that some nuclei can undergo the phenomenon of recoilless nuclear resonance fluorescence; this was in turn named the Mössbauer effect. Conservation of momentum indicates that a gamma ray emitted or absorbed by a nucleus would lose energy due to recoil during the process and this prevents resonant emission and absorption of a gamma ray. The Mössbauer effect occurs because the nuclei are bound in a crystal lattice which prevents the nuclei from moving during an emission or absorption event. Only certain isotopes undergo this phenomenon and a periodic table of Mössbauer elements is in Figure 2.8. The Mössbauer effect is only present in isotopes with low lying excited states and the resolution of the signals is dependent on the lifetime of the excited state.[22] These are two limiting factors for which elements can undergo the Mössbauer effect.

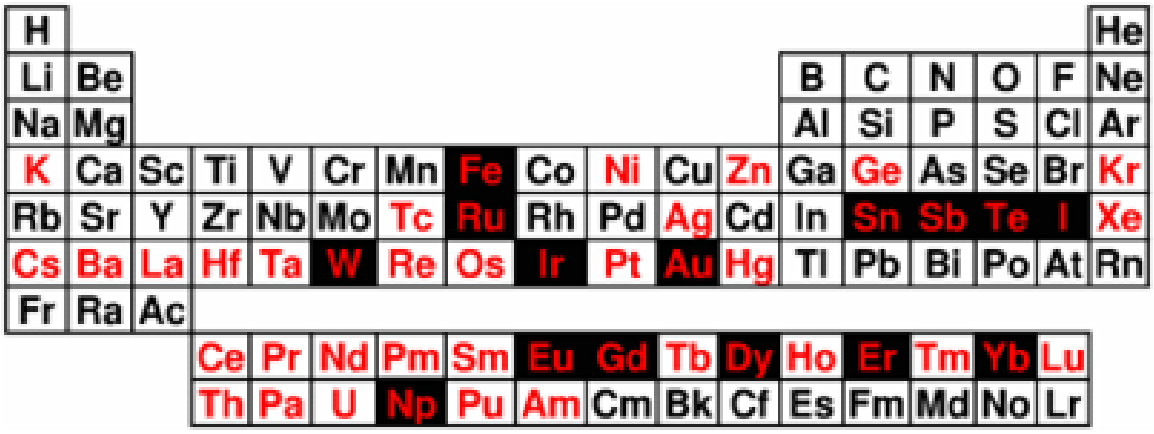

Figure 2.8 Periodic Table of Mössbauer elements. Red font are Mössbauer elements, the black fill are the most common. Adapted from the Royal Society of Chemistry [22].

Another issue with the Mössbauer effect is whether there is a viable source for the emitter. The most common element for Mössbauer is ^{57}Fe. In this case, ^{57}Co is used as the source which decays to the excited state of ^{57}Fe (Figure 2.9). The decay patterns for gamma ray emission in ^{57}Fe are shown. The energy of interest for Mössbauer spectroscopy is the 14.4 keV gamma rays. These gamma rays are directed to the absorber (sample of interest) and a transmission spectrum is collected. The way in which the gamma rays interact with the samples depends on the environment and electronic configuration of the atom inside the sample.

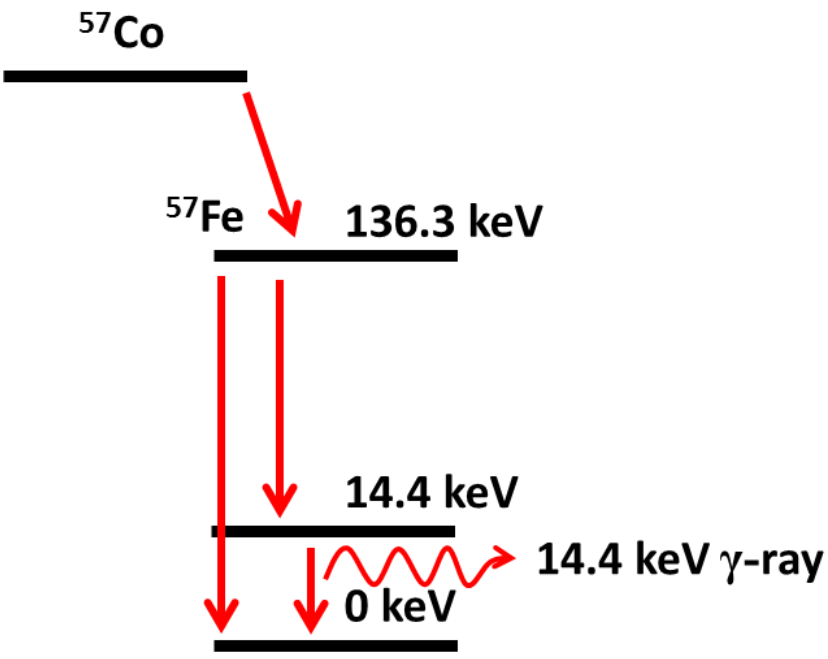

Figure 2.9 Decay pattern for ^{57}Fe Mössbauer spectroscopy.

Resonant absorption occurs when the energy of the gamma ray of an emitter (which is moving in Mössbauer spectroscopy) matches the nuclear transition energy for a Mössbauer nucleus in the absorber (stationary), and these nuclei must be

identical for resonance to occur.[23] As Mössbauer spectroscopy is sensitive to the chemical environment around the desired element, the emitter and absorber will not be in resonance if the two are in different environments. A moving emitter that is oscillated towards and away from the sample allows use of the Doppler Effect to bring the energies of the emitter and absorber back in resonance. The velocity (mm/s) is then used to determine the different sample characteristics that can be measure with this technique.

The isomer shift (or chemical shift, δ) occurs when the emitter (source) and absorber (sample) are not in identical environments. This manifests as a shift in the absorption peak position in the spectra. This change is due to the nuclear energy levels being affected by the *s* electron density around the atom. When atoms contain the nuclear spin quantum number $I > ½$, a quadrupole moment results because the distribution of positive charge in the nucleus is non-spherical.[1] This will result in a split absorption peak with a distance, Δ, between the two peaks. This is sensitive to oxidation state and local structure around the atom. Magnetic hyperfine splitting (Zeeman splitting) arises when the sample is exposed to a magnetic field. The nucleus will split from I levels to $2I + 1$ sublevels in response to this magnetic field. This can give information on the magnetic interactions in a material, such as, ferromagnetic, antiferromagnetic or paramagnetic and magnetic ordering temperatures can be found. Sample Mössbauer spectra describing all of these effects are shown in Figure 2.10.

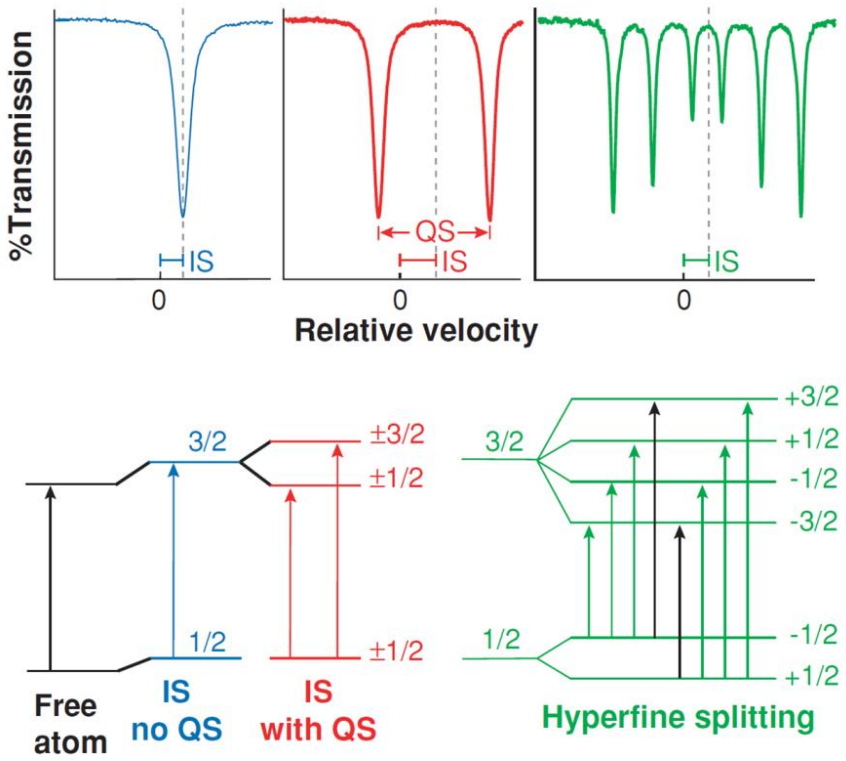

Figure 2.10 Sample Mössbauer spectra showing isomer shift (blue), quadrupole splitting (red) and magnetic hyperfine splitting (green). Adapted from Dyar et al. [24].

Mössbauer spectroscopy was used to determine the iron environment in $Na_3LiFeSbO_6$. This compound is discussed in Chapter 5. The experiment and data analysis were performed by Dr. Alain Wattiaux at the ICMCB.

2.6 Inductively Coupled Plasma – Atomic Emission Spectroscopy

Inductively coupled plasma – atomic emission spectroscopy (ICP-AES) is an important technique for elemental analysis and is sensitive enough to detect trace amounts of metals. Due to the nature of this technique, detection limits are in the 1 parts per billion range or lower for some elements. Quantitative results are

determined using sets of standards and a high range of linearity can be achieved, i.e., 50 ppb to 5000 ppb. This technique is useful when determining trace impurities in a sample or to aid in the determination of the stoichiometry of the elements in a compound.

Atomic emission spectroscopy exploits the electronic relaxation of an atom or ion from its excited state back down to its ground state. During this process, elements emit characteristic wavelengths of electromagnetic radiation that can be measured. ICP-AES employs argon plasma to excite the atoms or ions. The plasma, a conducting gaseous mixture of significant concentrations of cations and electrons[25], is created by discharging a spark through argon gas flowing through a radio frequency coil which is generating a high electromagnetic field around the gas. The spark initiates the ionization of argon which can then absorb sufficient power from the RF coil to sustain the plasma. A peristaltic pump carries the analyte of dissolved ions into a nebulizer that supplies a continuous aerosol of the analyte into the plasma. This steady state introduction of the sample into the plasma guarantees that enough of the atoms will be excited to relax to the ground state during the measurement at the wavelengths for each element. The wavelength is chosen by a monochromator and multiple elements in a sample can be measured by changing the monochromator position using a stepper motor. This is an advantage over flame atomic absorption spectroscopy that requires specific lamps at the proper wavelength to excite the sample and detect how much of the light was absorbed by the sample.

ICP-AES was performed by Laetitia Etienne at the ICMCB-Bordeaux for Chapters 5 and 6. This technique was employed to help determine the stoichiometry of the new compounds.

2.7 Thermal Gravimetric Analysis

Thermal analysis is a useful technique that can probe solid state reactions, thermal stability, dehydration processes, phase transitions and help in the building of phase diagrams.[1] Thermal gravimetric analysis (TGA) measures the change in mass of a sample over a time or temperature range and the experiment can be run under vacuum, in air or with a reactive gas (e.g., O_2). Sample mass can either decrease or increase depending on the reaction taking place. During a sample reaction, oxygen may be gained and an increase in the mass of the sample at the reaction temperature will be detected. During a decomposition or dehydration, a mass loss is measured. For example, if a mass loss is measured at 100°C and water was known to be in the sample, the mass percent loss can be used to determine the exact amount of water contained in the sample. After a decomposition process of solid materials, the resulting powders can then be analyzed using XRD to identify the exact decomposition products. Care must be taken because contamination of the instrument furnace will occur if the sample is completely vaporized or if there are volatile metals, i.e., antimony. A benefit to this technique is that only small sample sizes are needed (15 – 50 mg).

2.8 Scanning Electron Microscopy

Electron microscopy can be used to look at materials between the submicron and atomic level. A focused beam of electrons is shot at the sample and is scanned over the surface in a very small area, 50 to 100 Å.[1] Scanninc electron microscopy (SEM) takes advantage of the different process that can occur when electrons interaction with a material, emission of X-rays and/or secondary electrons, which can be used for elemental analysis and for building an image of the material.[26,1] An image of a material at this level can give information on particle sizes and shapes at the submicron level and the lower limit of SEM is approximately 100 Å.[1]

2.9 References

[1] A.R. West, Basic Solid State Chemistry, John Wiley & Sons, Chichester, 1999.
[2] D.A. Porter, K.E. Easterling, M.Y. Sherif, Phase Transformations in Metals and Alloys., CRC Press, Boca Raton, FL, 2009.
[3] A.K. Cheetham, P. Day, Solid State Chemistry Compounds, Oxford University Press, New York, 1992.
[4] M. Avdeev, V.B. Nalbandyan, I.L. Shukaev, in:, V.V. Kharton (Ed.), Solid State Electrochem. I, Wiley-VCH Verlag GmbH & Co. KGaA, 2009, pp. 227–278.
[5] B.D. Cullity, S.R. Stock, Elements of X-Ray Diffraction, Prentice Hall, Upper Saddle River, NJ, 2001.
[6] J. Rodriguez-Carvajal, T. Roisnel, Int. Union Crystallogr. Newsl. 20 (1998).
[7] T. Roisnel, J. Rodriguez-Carvajal, Prodeedings Seventh Eur. Powder Diffr. Conf. EPDIC 7 (2000) 118.
[8] A.C. Larson, R.B. Von Dreele, Los Alamos Natl. Lab. Rep. LAUR 86-748 (1994).
[9] B.H. Toby, J. Appl. Crystallogr. 34 (2001) 210.
[10] B.H. Toby, (n.d.).
[11] R.A. Young, International Union of Crystallography, Commission on Powder Diffraction, Netherlands Energy Research Foundation, eds., The Rietveld Method: International Workshop : Papers, Oxf. U. P., 1993.
[12] A.F. Orchard, Magnetochemistry, Oxford University Press, Oxford, 2003.
[13] J.P. Jakubovics, Magnetism and Magnetic Materials, Institute of Materials, London, 1994.

[14] J.B. Goodenough, Magnetism and the Chemical Bond, John Wiley & Sons: Interscience Publishers, New York-London, 1963.
[15] P.W. Anderson, Phys. Rev. 79 (1950) 350.
[16] J.B. Goodenough, A.L. Loeb, Phys. Rev. 98 (1955) 391.
[17] J. Kanamori, J. Phys. Chem. Solids 10 (1959) 87.
[18] S. Juds, Photoelectric Sensors and Controls: Selection and Application, First Edition, CRC Press, 1988.
[19] G. Kortüm, Reflectance Spectroscopy Principles, Methods, Applications, Springer Berlin Heidelberg, Berlin, Heidelberg, 1969.
[20] GianniG46, Wikipedia Free Encycl. (n.d.).
[21] P. Kubelka, F. Munk,, Z. Tech. Phys. 12 (1931) 593.
[22] Royal Society of Chemistry, Introd. Mössbauer Spectrosc. (2014).
[23] J. Danon, L. May, An Introduction to Mössbauer Spectroscopy., Plenum Press, New York, 1971.
[24] M.D. Dyar, D.G. Agresti, M.W. Schaefer, C.A. Grant, E.C. Sklute, Annu Rev Earth Planet Sci 34 (2006) 83.
[25] D.A. Skoog, F.J. Holler, S.R. Crouch, Principles of Instrumental Analysis., Thomson Brooks/Cole, Belmont, CA, 2007.
[26] A.K. Cheetham, Day, Solid State Chemistry: Techniques, Clarendon Press, Oxford [etc.], 1988.

Chapter 3

Review of Layered Oxides with Honeycomb Ordering Containing Bi^{5+}, Sb^{5+} or Te^{6+}

Although there are a multitude of compositions that have a layered structure and exhibit a honeycomb ordering, this work focuses on the compounds that contain Bi^{5+}, Sb^{5+} and Te^{6+} ordered with M^{2+} = Cu, Co, Ni, Mg, Zn or other heterovalent substitutions on the M site. This chapter is designed to cover the literature of these compounds and inform the reader of their significance to the field of layered compounds.

3.1 Compositions Containing Sb^{5+}

In 1990, a report on $Li_3Zn_2XO_6$ (X = Bi, Sb) compositions was published. The discussion focused on $Li_3Zn_2SbO_6$ and the structure was reported to have an ordering between the Zn/X cations octahedral sites in alternate layers separated by layers filled with Li^+ in octahedral sites.[1] Since then, the antimony containing phases have expanded to include many compositions ($A_3M_2SbO_6$, A^+ = Li, Na, Ag, Cu; M^{2+} = Co, Cu, Mg, Ni, Zn).[2–12] The compositions containing Li or Na crystallize with a monoclinic unit cell as an O3 variant of the layered honeycomb ordered structures with the monovalent cations filling octahedra voids between the slabs of $M_2SbO_6^{3-}$ (Figure 3.1a). The compositions containing Ag or Cu are related to the delafossite family and generally crystallize in the $P3_112$ space group. In the

delafossites, the monovalent cations fill spaces between the slabs to have linear coordination between oxygens of two slabs, Figure 3.1b.

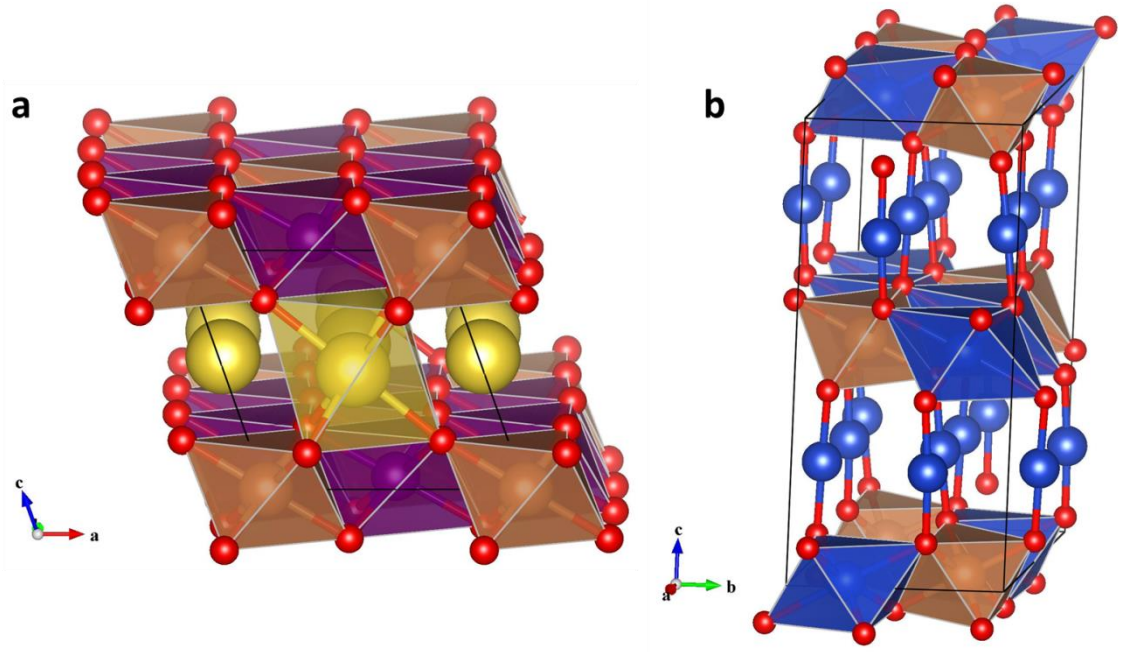

Figure 3.1 a) Unit cell representing the monoclinic $A_3M_2SbO_6$ compounds, interlayer light yellow atoms are in octahedral coordination and a honeycomb order exists in the $M_2SbO_6^{2-}$ slabs; b) Delafossite related $Cu_3Cu_2SbO_6$ structure with Cu^+ cations in linear coordination between the honeycomb ordered $Cu_2SbO_6^{2-}$ slabs.

Much attention has been paid to the compounds containing copper, i.e. $A_3Cu_2SbO_6$ (A^+ = Cu, Na, Li), due to the interesting behavior of Cu^{2+} in an octahedral coordination. In 1997 Skakle et al. reported on $Li_3Cu_2SbO_6$ (space group *C*2/*c*) and their results indicated mixing can occur between the Li^+ (0.76 Å) and Cu^{2+} (0.73 Å) due to similar ionic radii.[3,13] The structure with Li/Cu mixing was verified by a statement in a 2006 article, although, no structural data was presented.[14] The first magnetic investigation indicated this was a simple paramagnetic material[3], however, Miura et al. determined that this compound exhibited the same spin gap

magnetic behavior[14] as that of $Na_3Cu_2SbO_6$, which will be discussed shortly. A study in 2013 reinvestigated this compound and determined the structure should be indexed to the *C*2/*m* space group (*a* = 5.4655(7) Å, *b*= 8.7216(8) Å, *c* = 5.3845(7) Å and β = 115.270(5)°).[15] While the original structure description remains correct, this new cell creates a more regular environment for the SbO_6 and LiO_6 octahedra and a better fit to the experimental data. The copper containing compositions were also more interesting structurally because they exhibit a larger β angle in the monoclinic unit cell than that of other 2+ metal cations. Since the octahedra in the slabs of these structures are oriented to sit on one face, the axial bonds of the CuO_6 octahedra lie diagonally along the *ac* plane. The bond lengths therefore affect the β angle of the monoclinic unit cell as well as the *a* and *c* unit cell parameters. The larger lattice parameters exhibited for the copper compounds (a property that is unexpected when comparing ionic radii of Cu^{2+} with other M^{2+} cations for the honeycomb structures) is attributed to the Jahn-Teller distortion of Cu^{2+} in an octahedral coordination.

The discovery of $Na_3Cu_2SbO_6$ was first reported in 2005 by Smirnova et al. who indicated this material crystallized in the *C*2/*m* space group with lattice parameters *a* = 5.6759(1) Å, *b*= 8.8659(1) Å, *c* = 5.8379(1) Å and β = 113.289(1)°.[6] In contrast to the lithium analog, there is no mixing between the Na^+ (1.02 Å[13]) and Cu^{2+}, an affect due to the larger difference in the ionic radii, which also gives rise to the larger lattice parameters for the sodium analog. Comparing the structures of $Li_3Cu_2SbO_6$ and $Na_3Cu_2SbO_6$ helps to explain the difference in the observed magnetic

properties. As Li and Cu can mix, there are additional unpaired spins contributing to the observed magnetic properties.[6,8,14] First reports on the magnetic properties of $Na_3Cu_2SbO_6$ proposed an alternating chain model for super-exchange interactions in the honeycomb lattice which results in the observed spin gap behavior visible in the magnetic susceptibility plot vs. temperature. The plot of a spin gap presents an increase of the magnetic susceptibility with decreasing temperature and comes to a broad maximum before a downturn of the magnetic susceptibility towards zero (an example of this plot can be found in the next chapter, Figure 4.6. The presence of this spin gap behavior spurred a small controversy on how to describe the magnetic interactions in these distorted honeycomb structures. Although Miura et al. attempted to explain this behavior using heat capacity measurements, their comparison to the $Na_3Zn_2SbO_6$ compound is insufficient because this does not have any Jahn-teller active ions in the structure.[14,16] In 2007, Derakhshan et al. reinvestigated this material using high temperature magnetic susceptibility measurements and theoretical calculations to further characterize the prominent magnetic interactions within this compound. Their findings are depicted in Figure 3.2 where the strongest interactions were found to be along the *b*-axis where the longer green arrow (a) interactions are stronger than the shorter green arrow (b). The compound was again investigated by Koo et al. however they return to the conclusion made by Miura et al. where the interactions along (a) are antiferromagnetically coupled and the (b) interactions are ferromagnetically

coupled.[17] This same controversy and magnetic arrangement occurs for the $Na_2Cu_2TeO_6$ compound that is discussed in section 3.3.

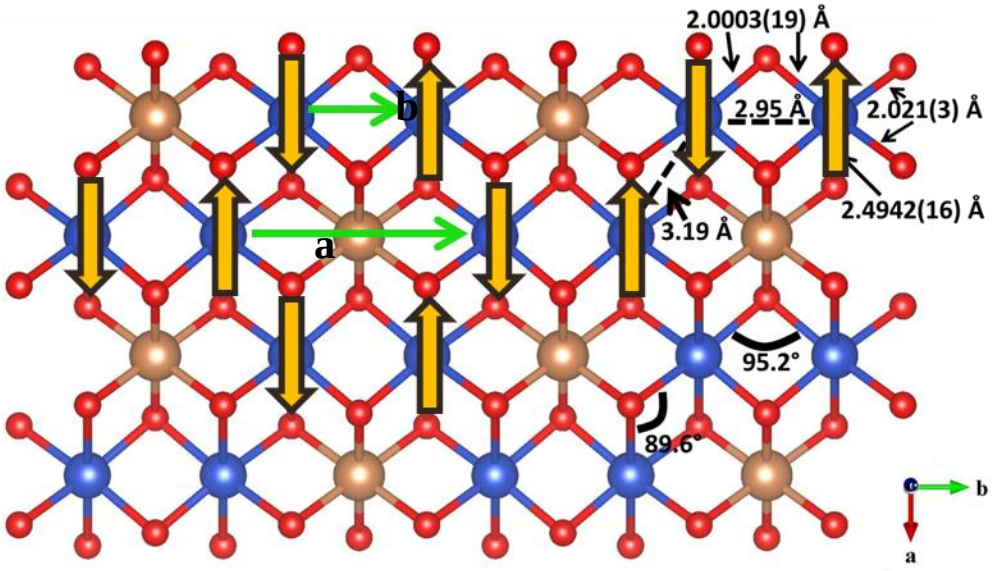

Figure 3.2 Dimer interactions in the Cu honeycomb lattice. Antimony is represented by tan spheres, copper by blue spheres and oxygen by red spheres. Important bond angles and distances are indicated to the right side of the figure.

Another new compound with honeycomb ordering of Cu^{2+} and Sb^{5+} was discovered in 2011 and has the composition Cu_5SbO_6.[11] This can be rewritten as $Cu_3^{+}Cu_2^{2+}SbO_6$ and has the delafossite structure with the monovalent copper ions in a linear coordination with oxygen. This material also exhibits a spin gap behavior with the maximum occurring at 189 K, a higher temperature than that of the previously discussed compounds. The higher temperature can be related to weaker dimer interactions in this compound compared to the antimony and tellurium compositions. These compounds differ in structure (FIGURE 3.1 a-b) but retain similar bond distances in the honeycomb layers.[18,6,11] This structural difference may give rise to the weaker interactions noticed in this compound.

The $A_3M_2SbO_6$ (A^+ = Li, Na; M^{2+} = Co, Ni, Mg, Zn) compositions have also been discussed regarding their structural and magnetic properties which arise from the d^8 Ni^{2+} and d^7 Co^{2+}. The Ni^{2+} containing compounds have a low temperature antiferromagnetic ordering but the Néel temperature shifts depending on the nature of the A^+ cation as well as changing the antimony with bismuth or tellurium.[5,10,12,19] The antiferromagnetic ordering for $Na_3Ni_2SbO_6$ was mentioned by Miura et al. in 2006, but no magnetic data was presented for this compound until the work presented in this dissertation.[14,20] Additionally, Miura et al. briefly discussed the magnetic properties of $Na_3Co_2SbO_6$, but this compound was not fully characterized until 2007 and a Néel temperature of 4.4 K was reported.[9,14] The structure and properties of $Na_3M_2SbO_6$ compositions were revisited by Politaev et al. in 2010, resulting in a discussion on the different structural models for these compounds. These authors also investigated the ion exchange compound $Ag_3Co_2SbO_6$ which is a delafossite material where Ag^+ is in the layer between the honeycomb ordered Co/Sb slabs.[10]

$Li_3Ni_2SbO_6$ has been investigated by multiple groups resulting in different structural characterizations. The first structural characterization used the *Fddd* space group but the discussion was limited.[2] This compound was not reinvestigated until a decade later where the structure was in agreement with the previous study and electrochemical properties were discussed.[7] A recent investigation by Zvereva et al. indicated that they could not reproduce the previous reports of the orthorhombic space group and determined this was another

monoclinic layered compound with honeycomb ordering in the $Ni_2SbO_6^{3-}$ slabs.[12] These authors also indicate this material has an antiferromagnetic ordering Néel temperature of 15 K. In comparison to the $Na_3Ni_2SbO_6$ compound (T_N = 18 K[20]), this transition is slightly lower but in good agreement. The presence of positive Weiss values indicates that these materials have short-range high temperature ferromagnetic interactions. Due to the structural relation of these compounds with that of Na_xCoO_2 and the superconductivity realized in the hydrated $Na_xCoO_2{\cdot}H_2O$ phase[21], Roudebush et al. investigated the hydrated materials $Na_xM_2SbO_6{\cdot}H_2O$ (M = Co(III) and Ni(III)).[22] The hydration of these compounds results in a loss of Na^+ ions within the layers and requires a partial oxidation of the M^{2+} to M^{3+}. The work described in Chapter 4 is based on the solid solutions in the compounds $Na_3M_{2-x}M'_xSbO_6$ (M, M' = Cu, Mg, Ni, Zn), which included the first magnetic susceptibility description for the Ni composition as well as structural characterization of the Mg end member as *C*2/*m*.[20] This work was the first report of the magnetic susceptibility of $Na_3Ni_2SbO_6$ and is in good agreement with the data published soon after by Roudebush et al.[20,22]

Heterovalent substitutions for the M^{2+} in the antimony compositions were first reported by Politaev et al. who reported on the composition Na_4FeSbO_6 (i.e., $Na_3NaFeSbO_6$) and its ion exchange product $Ag_3NaFeSbO_6$ which was not investigated in great detail.[23] These authors did not relate the former compound to that of the layered oxides with honeycomb ordering; this material was reinvestigated and discussed in Chapter 5 of this dissertation. Kumar et al. has

synthesized and reported the structural characterization of new layered compositions $Li_8M_2Sb_2O_{12}$ (M^{3+} = Al, Cr, Fe, Ga), but there are no property reports in this short communication.[24] A publication in the same timeframe reported on the discovery of the compound Li_4FeSbO_6 (i.e., $Li_3LiFeSbO_6$).[25] This material was thoroughly investigated to characterize the complex ordering within the slabs of $Li_{1/3}Fe_{1/3}Sb_{1/3}O_2^-$ which are separated by Li^+ cations filling voids in the interlayer space. This material exhibits an antiferromagnetic ordering Néel temperature at 3.6 K and crystallizes in the *C*2/*m* space group[25], similar to the other honeycomb ordered oxides discussed in this chapter and throughout this dissertation. In an attempt to investigate the solid solution between Li_4FeSbO_6 and Na_4FeSbO_6 only one new compound was realized with the composition $Na_3LiFeSbO_6$. A detailed discussion of this compound as well as the ion exchange product $Ag_3LiFeSbO_6$ can be found in Chapter 5.[26] An investigation on the compounds $Na_2NiMSbO_6$ (M = Al, Fe) was recently published but new honeycomb layered oxides were not found.[27]

The most characterized honeycomb ordered delafossites were first reported in 2002 with the compositions $CuM_{2/3}Sb_{1/3}O_2$ (M^{2+} = Mn, Co, Ni, Zn, Mg) and $AgM'_{2/3}Sb_{1/3}O_2$ (M'^{2+} = Ni, Zn).[4] The copper compositions were prepared via traditional ceramic synthesis and the silver compounds were prepared by ion exchange of the lithium analogs. Many of the compositions resulted in a mixture of the 3R and 2H delafossite polytypes or a disordered stacking arrangement. Roudebush et al. reinvestigated the $CuNi_{2/3}Sb_{1/3}O_2$ and $CuCo_{2/3}Sb_{1/3}O_2$ compositions and obtained ordered samples and investigated the magnetic susceptibility for both

compositions. These compounds were found to crystallize in the space group *C*2/*c* and both exhibit Néel temperatures at 22.3 K and 18.5 K respectively for the nickel and cobalt compositions.[4] The Néel temperature for the cobalt composition is higher than that described about for $Na_3Co_2SbO_6$ and is contributed to potentially stronger coupling through the Cu^+ layer.[28]

3.2 Compositions Containing Bi^{5+}

As mentioned previously, Greaves et al. reported on the $Li_3Zn_2XO_6$ (X = Bi, Sb) compounds but much of their attention was paid to the composition containing antimony. They reported the cell dimensions of $Li_3Zn_2BiO_6$ (a = 5.344(4) Å, b = 9.221(3) Å, c = 5.255(5) Å and β = 109.57(6)°) and $Li_4Zn_{1.5}BiO_6$ (a = 5.363(2) Å, b = 9.183(3) Å, c = 5.323(2)Å and β = 110.65(2)°) but little discussion was devoted to these compounds otherwise. The authors reported that the $Li_{3.5}Zn_{1.5}BiO_{5.75}$ compound had a desirable activation energy for Li^+ ion migration but the conductivity was lower than other materials because the structure has no cation vacancies for easy ion conduction.[1]

In Chapter 6, the adapted manuscript on the discovery and characterization of $Li_3Ni_2BiO_6$ as well as the delafossite exchange product $Ag_3Ni_2BiO_6$ is presented. The latter compound is to our knowledge the only delafossite compound containing Bi^{5+}. Although Greaves et al. first discussed compositions containing bismuth; their work could not be reproduced, so this study can be considered the first full characterization and report focused on bismuth containing compositions. The study

of partially substituted phases, O3-$Li_3NiMBiO_6$ (M^{2+} = Mg, Cu, Zn), is also discussed in this work. It is interesting to note in this short review that when copper is substituted, the lattice parameters of the *C2/*m space group did not follow the general trend with the other compositions when based on a simple ionic radius explanation. The β angle of the monoclinic cell is larger than expected and there was an increase in the *a* and *c* parameters with a decrease of the *b* parameter. This follows the same trend as previously discussed compositions that contain copper. Full substitution of Ni^{2+} in $Li_3Ni_2BiO_6$ with Cu^{2+}, Mg^{2+} and Zn^{2+} could not be obtained.[19]

Seibel et al. has more recently discovered and characterized the $Na_3M_2BiO_6$ compositions (M^{2+} = Ni, Mg, Zn). There is good structural agreement with these compounds and the previously discussed materials in that they can be indexed and refined to the *C*2/*m* space group.[29] The magnetism of the $Na_3Ni_2BiO_6$ compound correlates to the other compositions $Li_3Ni_2BiO_6$, $Li_3Ni_2SbO_6$ and $Na_3Ni_2SbO_6$ in the low temperature antiferromagnetic ordering and the Weiss constant is positive indicating ferromagnetic interactions are present as well.[12,19,20,29] The relationships of this behavior are discussed in Chapters 4 and 6.

3.3 Compositions Containing Te^{6+}

For the $Na_2M_2TeO_6$ compounds, three structures are known with the space groups *P*$6_3$22 (M = Co, Mg, Zn), *P*6_3/*mcm* (M = Ni) and *C* 2/*m* (M = Cu), which can be seen in Figure 3.3.[18,30] Excluding $Na_2Cu_2TeO_6$, these materials are known as P2

structures where the interlayer sites are partially filled by Na^+ ions and two layers are required to describe the hexagonal unit cell. In 2007, the layered phase P2-$Na_2Co_2TeO_6$ (i.e., $Na_{2/3}Co_{2/3}Te_{1/3}O_2$) was reported and it is structurally related to layered P2-Na_xCoO_2 where the Co^{2+}/Te^{6+} order within each slab.[9] Each TeO_6 octahedron is surrounded by six CoO_6 octahedra, which form a honeycomb-like network (Figure 3.3). More recently, the analogs with the composition P2-$Na_2M_2TeO_6$ (M^{2+} = Mg, Ni and Zn) were investigated.[30] Due to the partial filling and coordination of the interlayer sites, larger windows are available for fast ionic conduction[30] which ultimately lead to a recent study by Gupta et al. that investigated $Na_{2-x}M_2TeO_6$ (M^{2+} = Co, Ni) as electrode materials for Na ion batteries.[31] It was shown by Evstigneeva et al. that the nickel compound possesses a different stacking sequence of the slabs than that of the cobalt and zinc compounds.[30] This causes a structural transition from nickel (space group $P6_3/mcm$) to cobalt or zinc (space group $P6_322$) compounds which is described in the study of the solid solutions in Chapter 7.[32] Kumar et al. synthesized and characterized many new layered compositions of $Li_8M_2Te_2O_{12}$ (M^{2+} = Co, Cu, Ni, Zn) through conventional solid state methods.[24] These authors also reported more detailed investigations of $Li_3Cu_2TeO_6$ and $Li_3Ni_2TeO_6$ synthesized via low temperature ion exchange.[33] The copper variant forms the same monoclinic structure that of the $Na_2Cu_2TeO_6$ compound. The nickel compounds show multiple phases when prepared via ion exchange from the $Na_2Ni_2TeO_6$ and a metastable orthorhombic unit cell when prepared through direct solid state synthesis.[33]

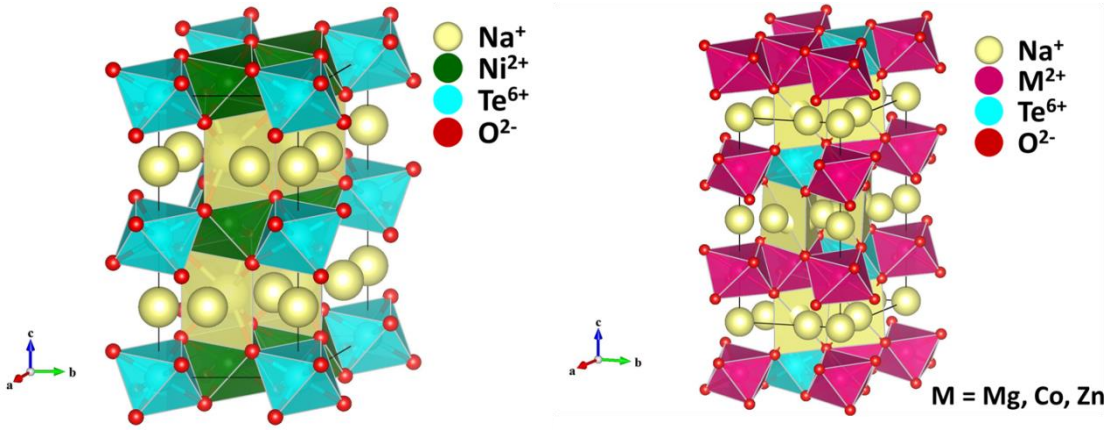

Figure 3.3 Structure of $Na_2Ni_2TeO_6$ space group *P*6$_3$/*mcm* (left) and $Na_2M_2TeO_6$ space group *P*6$_3$22 (right). In both cases, the light yellow Na^+ atoms are shown in all possible trigonal prismatic positions available in the interlayer space. Detailed structure analyses have not been successful in pinpointing exact locations.[30]

Xu et al. first reported on $Na_2Cu_2TeO_6$ which exhibits a spin gap behavior with a maximum magnetic susceptibility at 160 K. The spin gap behavior is the same as investigated by Derakhshan et al. which was discussed in detail in section 3.1.[16] They also describe this structure as a monoclinic unit cell with the *C*2/*m* space group, which is related to the antimony phases also described in section 3.1. The difference in structure compared to the other compounds containing tellurium is attributed to the Jahn-Teller distortion that accompanies Cu^{2+} in an octahedral coordination.

As with the antimony phases, heterovalent substitutions for M^{2+} within the $Na_2M_2TeO_6$ layered oxides were investigated by Nalbandyan et al. who discovered one new compound, $Na_2LiFeTeO_6$.[27] They studied the structure of this compound in the $P2_12_12_1$ space group and determined a honeycomb arrangement of LiO_6 and

FeO_6 around the TeO_6 octahedra. The interlayer Na^+ ions filling the prisms that share faces with TeO_6 octahedra are off center to accommodate the repulsion of the cations.[27]

3.4 References

[1] C. Greaves, S.M.A. Katib, Mater. Res. Bull. 25 (1990) 1175.
[2] G.C. Mather, R.I. Smith, J.M.S. Skakle, J.G. Fletcher, M.A. Castellanos R, M.P. Gutierrez, A.R. West, J. Mater. Chem. 5 (1995) 1177.
[3] J.M.S. Skakle, M.A. Castellanos R., S.T. Tovar, A.R. West, J. Solid State Chem. 131 (1997) 115.
[4] R. Nagarajan, S. Uma, M.K. Jayaraj, J. Tate, A.W. Sleight, Solid State Sci. 4 (2002) 787.
[5] O.A. Smirnova, M. Avdeev, V.B. Nalbandyan, V.V. Kharton, F.M.B. Marques, Mater. Res. Bull. 41 (2006) 1056.
[6] O.A. Smirnova, V.B. Nalbandyan, A.A. Petrenko, M. Avdeev, J. Solid State Chem. 178 (2005) 1165.
[7] X. Ma, K. Kang, G. Ceder, Y.S. Meng, J. Power Sources 173 (2007) 550.
[8] Y. Miura, R. Hirai, T. Fujita, Y. Kobayashi, M. Sato, J. Magn. Magn. Mater. 310 (2007) e389.
[9] L. Viciu, Q. Huang, E. Morosan, H.W. Zandbergen, N.I. Greenbaum, T. McQueen, R.J. Cava, J. Solid State Chem. 180 (2007) 1060.
[10] V.V. Politaev, V.B. Nalbandyan, A.A. Petrenko, I.L. Shukaev, V.A. Volotchaev, B.S. Medvedev, J. Solid State Chem. 183 (2010) 684.
[11] E. Climent-Pascual, P. Norby, N.H. Andersen, P.W. Stephens, H.W. Zandbergen, J. Larsen, R.J. Cava, Inorg. Chem. 51 (2011) 557.
[12] E.A. Zvereva, M.A. Evstigneeva, V.B. Nalbandyan, O.A. Savelieva, S.A. Ibragimov, O.S. Volkova, L.I. Medvedeva, A.N. Vasiliev, R. Klingeler, B. Buechner, Dalton Trans. 41 (2012) 572.
[13] R.D. Shannon, Acta Crystallogr. Sect. A 32 (1976) 751.
[14] Y. Miura, R. Hirai, Y. Kobayashi, M. Sato, J. Phys. Soc. Jpn. 75 (2006) 084707.
[15] V.B. Nalbandyan, M. Avdeev, M.A. Evstigneeva, J. Solid State Chem. 199 (2013) 62.
[16] S. Derakhshan, H.L. Cuthbert, J.E. Greedan, B. Rahaman, T. Saha-Dasgupta, Phys. Rev. B 76 (2007) 104403.
[17] H.-J. Koo, M.-H. Whangbo, Inorg Chem 47 (2007) 128.
[18] J. Xu, A. Assoud, N. Soheilnia, S. Derakhshan, H.L. Cuthbert, J.E. Greedan, M.H. Whangbo, H. Kleinke, Inorg. Chem. 44 (2005) 5042.
[19] R. Berthelot, W. Schmidt, S. Muir, J. Eilertsen, L. Etienne, A.W. Sleight, M.A. Subramanian, Inorg. Chem. 51 (2012) 5377.
[20] W. Schmidt, R. Berthelot, A.W. Sleight, M.A. Subramanian, J. Solid State Chem. 201 (2013) 178.
[21] K. Takada, H. Sakurai, E. Takayama-Muromachi, F. Izumi, R.A. Dilanian, T. Sasaki, Nature 422 (2003) 53.
[22] J.H. Roudebush, R.J. Cava, J. Solid State Chem. 204 (2013) 178.
[23] V.V. Politaev, V.B. Nalbandyan, Solid State Sci. 11 (2009) 144.

[24] V. Kumar, N. Bhardwaj, N. Tomar, V. Thakral, S. Uma, Inorg. Chem. 51 (2012) 10471.
[25] E.A. Zvereva, O.A. Savelieva, Y.D. Titov, M.A. Evstigneeva, V.B. Nalbandyan, C.N. Kao, J.-Y. Lin, I.A. Presniakov, A.V. Sobolev, S.A. Ibragimov, M. Abdel-Hafiez, Y. Krupskaya, C. Jähne, G. Tan, R. Klingeler, B. Büchner, A.N. Vasiliev, Dalton Trans. 42 (2013) 1550.
[26] W. Schmidt, R. Berthelot, L. Etienne, A. Wattiaux, M.A. Subramanian, Mater. Res. Bull. 50 (2014) 292.
[27] V.B. Nalbandyan, A.A. Petrenko, M.A. Evstigneeva, Solid State Ion. 233 (2013) 7.
[28] J.H. Roudebush, N.H. Andersen, R. Ramlau, V.O. Garlea, R. Toft-Petersen, P. Norby, R. Schneider, J.N. Hay, R.J. Cava, Inorg. Chem. (2013).
[29] E.M. Seibel, J.H. Roudebush, H. Wu, Q. Huang, M.N. Ali, H. Ji, R.J. Cava, Inorg. Chem. 52 (2013) 13605.
[30] M.A. Evstigneeva, V.B. Nalbandyan, A.A. Petrenko, B.S. Medvedev, A.A. Kataev, Chem. Mater. 23 (2011) 1174.
[31] A. Gupta, C. Buddie Mullins, J.B. Goodenough, J. Power Sources 243 (2013) 817.
[32] R. Berthelot, W. Schmidt, A.W. Sleight, M.A. Subramanian, J. Solid State Chem. 196 (2012) 225.
[33] V. Kumar, A. Gupta, S. Uma, Dalton Trans. 42 (2013) 14992.

Chapter 4

Solid Solution Studies of Layered Honeycomb-Ordered Phases O3-$Na_3M_2SbO_6$ (M = Cu, Mg, Ni, Zn)

4.1 Introduction

In this present study we focused our interest on the O3-$Na_3M_2SbO_6$ compounds and studied the solid solutions for M^{2+} = Cu, Mg, Ni, Zn. In these compounds the SbO_6 octahedron is surrounded by six MO_6 edge-sharing octahedra forming the honeycomb lattice (Figure 4.1). The Na^+ ions are intercalated within the M_2SbO_6 slabs and occupy an octahedral NaO_6 site. These compounds were synthesized using solid state method and were characterized using X-ray diffraction, magnetic susceptibility and diffuse reflectance. This is the first report on the solid solutions and optical studies for these compounds.

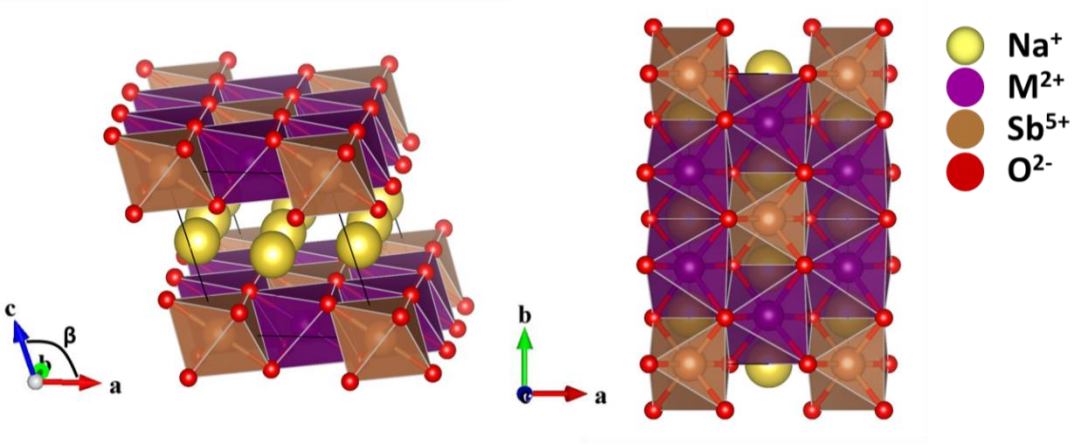

Figure 4.1 Representation of the O3-$Na_3M_2SbO_6$ structure. Left: Perspective along the *b* direction, indicating the stacking of the $M_{2/3}Sb_{1/3}O_2$ slabs with the Na^+ cations filling the octahedral interslab voids and the β angle between the *a* and *c* directions. Right: Perspective along the *c* direction, indicating the honeycomb ordering within the $M_{2/3}Sb_{1/3}O_2$ slabs with six MO_6 octahedra surrounding one SbO_6 octahedra. All the octahedral in this structure are edge sharing.

4.2 Results and discussion

4.2.1 XRD Studies of O3-$Na_3M_2SbO_6$ (M = Cu, Mg, Ni, Zn) and the Solid Solutions

The powder X-ray diffraction (PXRD) patterns for the compositions $Na_3M_2SbO_6$ (M = Cu, Mg, Ni, Zn) are shown in Figure 2. All of the patterns were indexed to the monoclinic space group *C2/m* and there were no traces of impurity phases. The refined lattice parameters are listed in Table 4.1. When M = Mg, Ni and Zn, the lattice parameters agree well with reported values (Table 4.1) and they also follow an expected trend based on the radii of the M^{2+} ion (Ni^{2+} = 0.69 Å, Mg^{2+} = 0.72 Å and Zn^{2+} = 0.74 Å).[1] Therefore there is only a slightly visible shifting of the *hkl* reflections which can be seen in Figure 4.2. It has been reported that these honeycomb layered materials can also be indexed using the $P3_112$ or the *C2/c* space groups; however Bréger *et al*. reports that the *C2/m* space group has the lowest calculated energy for the ordered honeycomb compounds.[2–4] With an ionic radius of 0.73 Å, it would be assumed that the lattice parameters for $Na_3Cu_2SbO_6$ would fall between those of the magnesium and zinc compositions. The copper composition however, has larger *a* and *c* lattice parameters, a smaller *b* lattice parameter and a much larger β angle than the other compositions. The PXRD pattern in Figure 4.2 indicates this difference with the shifted reflections of the monoclinic cell. This deviance from a linear trend cannot be explained by using the ionic radii. This change in the lattice constant trend is attributed to the Jahn-Teller (J-T) distortion that can occur with Cu^{2+} in an octahedral coordination.[4] The J-T

distortion of CuO_6 octahedra results in an axial extension and an equatorial compression of Cu – O bonds. As is seen in Figure 4.1, the MO_6 octahedra sit on a face and share edges with the other octahedral throughout the M_2SbO_6 slabs. The axial extension of the CuO_6 octahedron results in the smaller *b* parameter and the equatorial compression results in the larger *a* and *c* lattice parameters. This also creates the larger β angle and the highly shifted *hkl* reflections of the $Na_3Cu_2SbO_6$ composition. This Jahn-Teller structural distortion has been observed in other compounds containing copper, such as $Li_3NiCuBiO_6$ and $Li_3Cu_2SbO_6$.[5–7]

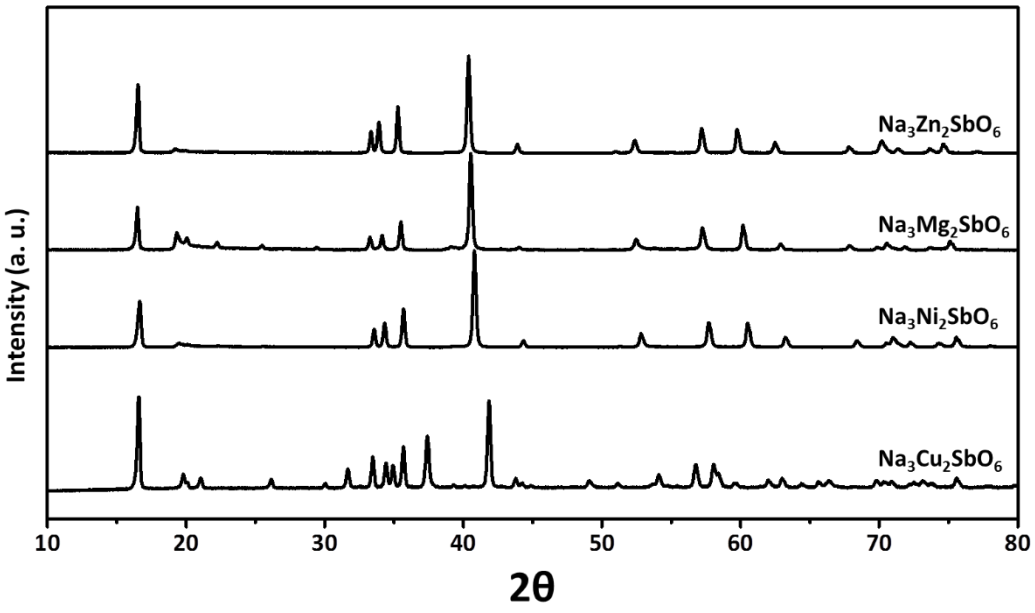

Figure 4.2 PXRD patterns of all O3-$Na_3M_2SbO_6$ where M = Cu, Mg, Ni, Zn. All patterns were indexed to the monoclinic space group *C2/m*. A broad asymmetry in the 17° to 30° 2θ region indicates the presence of some concentration of stacking faults in the Mg, Ni and Zn compounds. The reduced intensities for the Ni and Zn patterns in this region is related to low crystallinity and stacking faults that affect these *hkl* reflections. The dramatic shifting of the *hkl* reflections in the Cu compounds is caused by the Jahn-Teller distortion of the CuO_6 octahedra.

Table 4.1 Experimental and literature lattice parameters for $Na_3M_2SbO_6$ (M = Cu, Mg, Ni, Zn). *Only LeBail fits were performed in this work. Full refinement for these layered systems is difficult due to stacking defects and low crystallinity. **The lattice parameters reported for the magnesium and zinc compounds were transformed to the monoclinic phase based on the hexagonal parameters reported by Politaev *et al.*

Space Group: *C2/m*	a (Å)	b (Å)	c (Å)	β (°)	Volume (Å^3)	Reference
$Na_3Zn_2SbO_6$	5.3636(1)	9.2722(1)	5.6645(1)	108.47(1)	267.20(1)	This work.*
	5.3522	9.275	5.6718	108.34		[3]**
$Na_3Mg_2SbO_6$	5.3285(1)	9.1908(1)	5.6711(1)	108.30(1)	263.69(1)	This work.*
	5.317	9.21	5.680	108.18		[3]**
$Na_3Ni_2SbO_6$	5.3055(1)	9.1713(1)	5.6273(1)	108.35(1)	259.89(1)	This work.*
	5.3048(4)	9.1876(6)	5.6298(5)	108.300(8)		[3]**
$Na_3Cu_2SbO_6$	5.6691(1)	8.8448(1)	5.8252(1)	113.37(1)	268.12(1)	This work.*
	5.6759(1)	8.8659(1)	5.8379(1)	113.289(1)		[4]

It is noticed that the reflections in the PXRD patterns between 17° and 30° 2θ are very weak for the Zn^{2+} and Ni^{2+} compounds. The crystallinity of our compounds may have been hindered by our use of slightly lower temperature than that reported by Politaev *et al*. for synthesis. This did not however affect our profile matching to the *C2/m* space group. This 2θ region is also where stacking faults affect the resolution of the *hkl* reflections and create an asymmetric broadening of the affected reflections. The phenomenon is easily noticed in the PXRD pattern of the magnesium composition (Figure 4.2). This broadening is described as stacking defects along the monoclinic *c* axis and is present in the $Na_3Ni_2SbO_6$[3] parent compound as well as in other related "honeycomb" layered materials, e.g. in Li_2MnO_3.[2,8] These stacking faults arise in layered structures because of a variety of stacking sequences available for each layer which affects the intercalation site symmetry for the interslab ions as discussed earlier. The calculated energies

associated with the different stacking sequences of the *P3$_1$12* and the *C2/c* are only 1 meV and 2 meV, respectively, higher than that of the *C2/m* space group. Such closely related energies will result in stacking faults to arise in the layered structures. Bréger *et al.* found that in the Li_2MnO_3 compounds, the annealing time decreased the stacking faults more so than the annealing temperature and related these fault formations to slow kinetics of growth along the *c* direction. Due to the presence of stacking faults, it is difficult for Rietveld refinement therefore; the reported lattice parameters in this work are from LeBail profile refinement using a Pseudo-Voigt function.

As pure end members were obtained with similar experimental parameters, it is therefore reasonable to synthesize the intermediate compositions $Na_3M_{2-x}M'_xSbO_6$ (M, M' = Cu, Mg, Ni, Zn; $0 \leq x \leq 2$). As a general case and in order to lighten the study, only the PXRD for the solid solutions $Na_3Ni_{2-x}Mg_xSbO_6$ and $Na_3Cu_{2-x}Zn_xSbO_6$ are shown in Figures 4.3 and 4.4 respectively. As expected, the *a, b* and *c* parameters only slightly shift in a linear fashion due to the radii of the cations while the β angle is constant at approximately 108° for M = Ni, Mg, Zn. Indeed the unit cell increases from 259 Å^3 (for Ni^{2+}, 0.69 Å), 263 Å^3 (for Mg^{2+}, 0.72 Å) and 267 Å^3 (for Zn^{2+}, 0.74 Å).

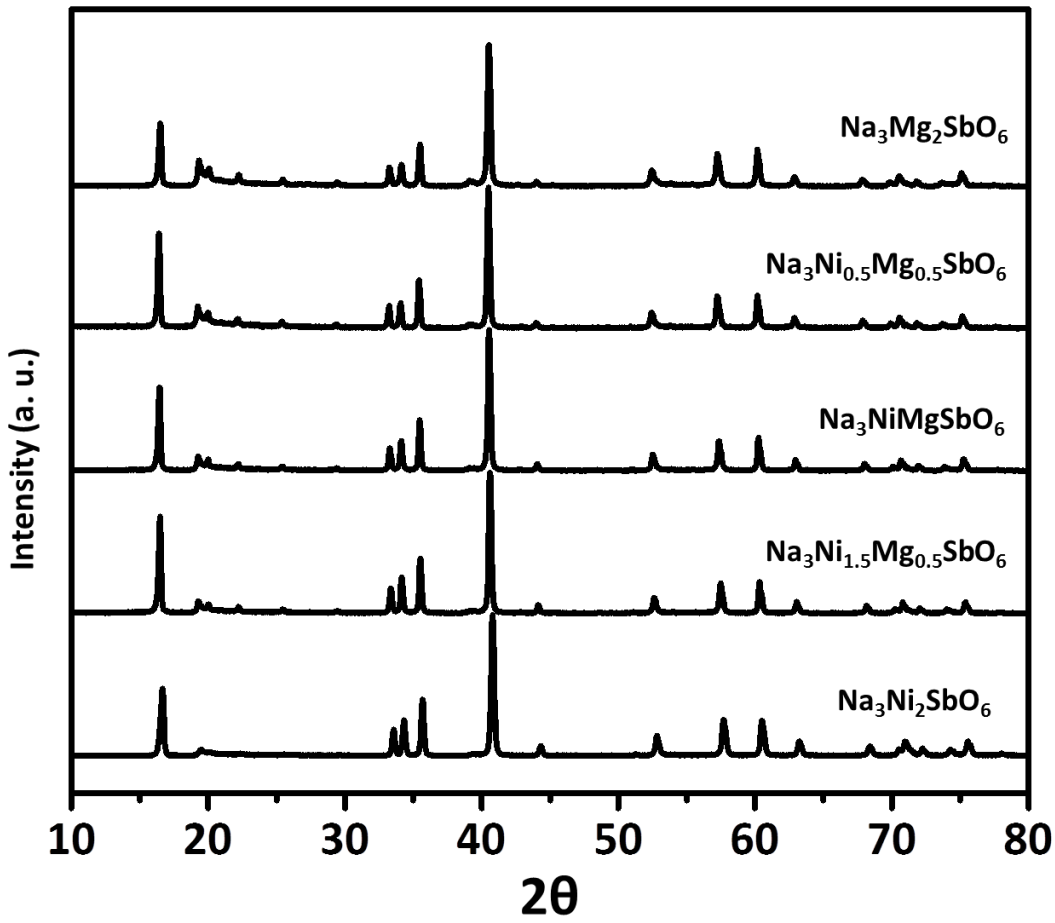

Figure 4.3 PXRD patterns for $Na_3Ni_{2-x}Mg_xSbO_6$ solid solution for *x* = 0, 0.5, 1, 1.5, 2. The slight shifting of the *hkl* positions is due to the ionic radius of the respective M^{2+} present here.

The solid solutions containing copper were also synthesized without impurity however the lattice parameters change more dramatically along the $Na_3Cu_{2-x}M_xSbO_6$ (M = Mg, Ni, Zn) series than those for the solid solutions not containing copper. As an example, the PXRD patterns for the series $Na_3Cu_{2-x}Zn_xSbO_6$ are shown in Figure 4.4a-b. In $Na_3Cu_2SbO_6$, the Cu^{2+} is Jahn-Teller (J-T) active which results in an elongation of the axial Cu – O bonds (affecting the *b* axis) and a contraction of the equatorial Cu – O bonds (affecting the *a* and *c* axes). The stretching of the axial

bonds and contraction of the equatorial bonds in the CuO_6 octahedra cause the β angle to become larger than that of the other M^{2+} compounds. The lattice parameter and β angle shifts are presented in Figure 4.5a-b. This trend related to the J-T activity of Cu^{2+} was previously noted in the similar phase $Li_3NiCuBiO_6$.[5] Dilution of the J-T active Cu^{2+} reduces the distortion in the M_2SbO_6 slabs. Therefore, the specific *hkl* reflections that are involved in the transition from the regular ZnO_6 octahedra to the distortion of the J-T CuO_6 octahedra clearly shifts along the solid solution $Na_3Cu_{2-x}Zn_xSbO_6$.

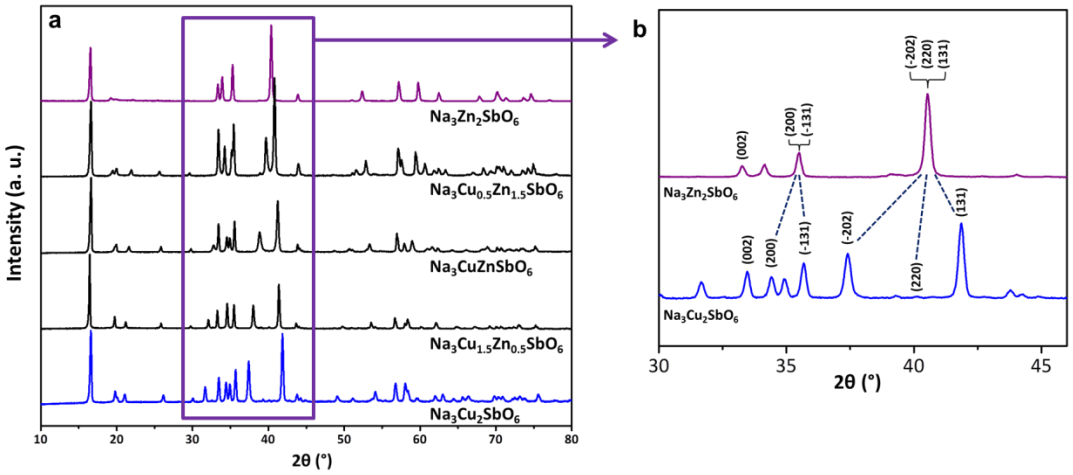

Figure 4.4a-b a) PXRD patterns for solid solution $Na_3Cu_{2-x}Zn_xSbO_6$, the highlighted section indicates the 2θ region that is highly affected by the transition from regular ZnO_6 octahedra to Jahn-Teller distorted CuO_6 octahedra. b) Evolution of the highly affected *hkl* positions resulting from the regular ZnO_6 octahedra vs. the J-T distorted CuO_6 octahedra within the monoclinic structure of the end member compositions.

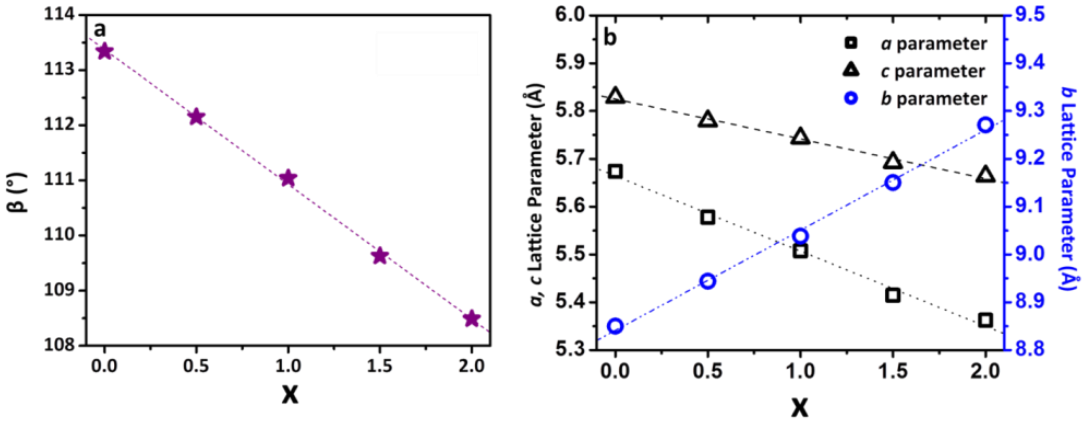

Figure 4.5a-b Lattice parameter evolution for the solid solution $Na_3Cu_{2-x}Zn_xSbO_6$ for *x* = 0, 0.5, 1. 1.5, 2. a) Evolution of the β angle as the Jahn-Teller active Cu^{2+} is diluted. b) Linear trends of the *a*, *b*, and *c* lattice paramteters, the direction of the lattice parameter shifting is a result of the distortion from J-T Cu^{2+} and is opposite of what would be expected from the ionic radii.

It is interesting to denote that in all the studied solid solutions, no superstructure due to additional ordering between M and M' cations were evidenced.

4.2.2 Magnetic Susceptibility:

It is interesting to study the magnetic properties as Ni^{2+} ($3d^8$) and Cu^{2+} ($3d^9$) have complex magnetic interactions depending on the nearest neighbors in the honeycomb ordering of these compounds. Previous reports indicate a spin gap behavior in $Na_3Cu_2SbO_6$, which is also present in the delafossite phase Cu_5SbO_6 (*i.e.* $Cu_3Cu_2SbO_6$) and O3-$Na_2Cu_2TeO_6$, due to Cu – Cu dimer formation in the Cu_2SbO_6 honeycomb layers.[9–13] Due to the honeycomb ordering of the Cu_2SbO_6 slabs and

the Jahn-Teller distortion of the CuO_6 octahedra, two copper neighbors come close enough to form Cu_2O_{10} dimers. The magnetic susceptibility plot can be seen in Figure 6 and shows a broad maximum at ~90 K, indicative of a spin gap behavior.[4,9,10,13] The high temperature data follows the Curie-Weiss law and was fit with $\chi = C/(T - \theta)$ between 150 and 300 K which revealed μ_{eff} = 2.55 μB and θ = -23 K. This effective magnetic moment is in agreement with the calculated theoretical magnetic moment μ_{theor} = 2.45 μ_B.

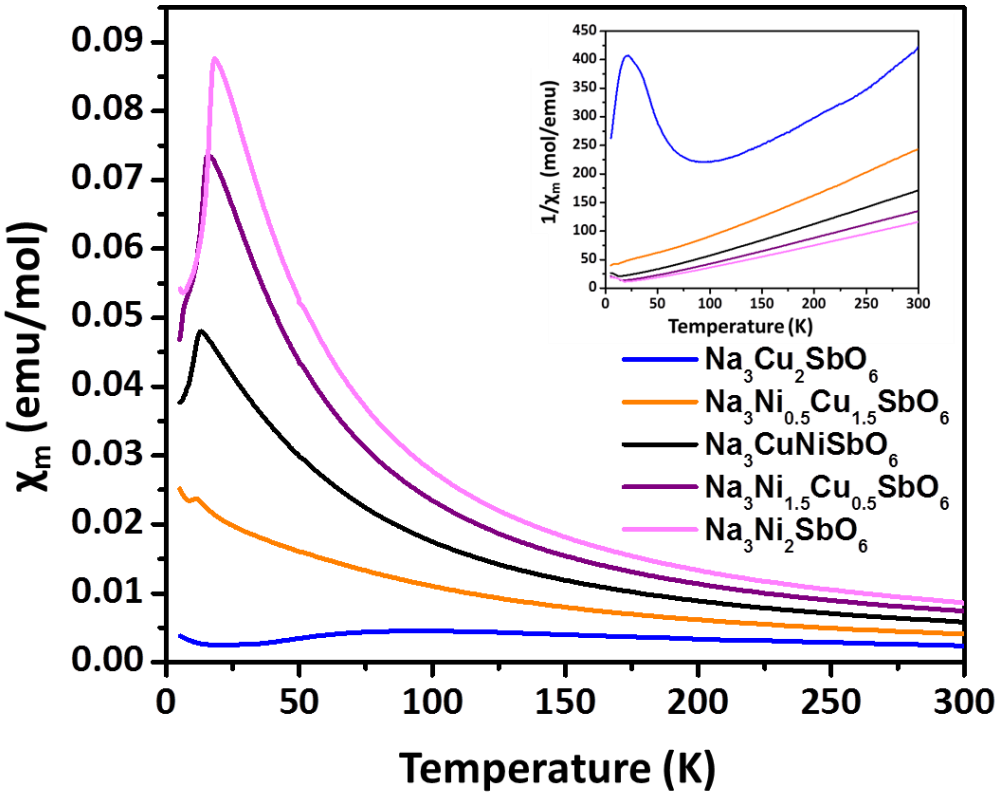

Figure 4.6 Magnetic susceptibility, χ vs. T, for $Na_3Ni_{2-x}Cu_xSbO_6$ with an inset showing the 1/χ vs. T plot for this solid solution. The high temperature data follows the Curie-Weiss law and is fit from 150 – 300 K to determine the μ_{eff} for each composition. The T_N present due to the $Na_3Ni_2SbO_6$ phase (pink line) slightly shifts to lower temperatures and disappears only at the $Na_3Cu_2SbO_6$ parent compound. The copper parent phase (blue line) indicates spin gap behavior which has been thoroughly discussed and reported previously.

There is no report on the magnetic behavior of $Na_3Ni_2SbO_6$, to our knowledge. The magnetic susceptibility evolution of $Na_3Ni_2SbO_6$ is also shown in Figure 4.6. At low temperatures the data indicates a long-range antiferromagnetic ordering with a $T_N \approx 18$ K. At high temperatures, the magnetic susceptibility data follows the Curie-Weiss law and the inverse susceptibility follows a linear trend. The effective magnetic moment for $Na_3Ni_2SbO_6$ is $\mu_{eff} = 4.45\ \mu_B$, which is in agreement with the theoretical value assuming Ni^{2+} spin-only contributions ($\mu_{theor} = 4.00\ \mu_B$). The Weiss constant is positive (15 K), indicating ferromagnetic short-range interactions. This data is in agreement with the related $Li_3Ni_2BiO_6$ and $Li_3Ni_2SbO_6$ compositions.[5,14] These Ni^{2+} containing compounds both contain an antiferromagnetic transition at low temperatures with $T_N = 5.5$ K[5] and 15 K[14], respectively. These compounds also show positive Weiss constants when fit with the Curie-Weiss law from 150 – 300 K which also indicates ferromagnetic interactions at high temperatures. The observed transition for the $Na_3Ni_2SbO_6$ composition is very close to that reported for $Li_3Ni_2SbO_6$ with a $T_N = 15$ K[14]; however both are higher than that for the $Li_3Ni_2BiO_6$ composition with a $T_N = 5.5$ K[5] and that of Na3Ni2BiO6 with a TN = 10.4 K.[15] Since Bi^{5+} (0.76 Å) is larger than Sb^{5+} (0.60 Å), the ionic size affects the T_N for these compounds. The larger Bi^{5+} causes this lower transition temperature because it further separates the Ni^{2+} ions and creates a longer distance for the Ni^{2+}–O–Ni^{2+} superexchange pathway. The 90° angle of the Ni^{2+}–O–Ni^{2+} pathway for the $A_3Ni_2SbO_6$ (A^+ = Li, Na) indicates ferromagnetic

interaction however Zvereva *et al.* discusses how the low temperature antiferromagnetic interactions would be arising from antiferromagnetic ordering between the layers.[14] As Bi^{5+} is larger than Sb^{5+}, this would decrease the covalency within the slabs and decrease the T_N, which is the result for these compounds.

The magnetic susceptibility evolution for the $Na_3Ni_{2-x}Cu_xSbO_6$ solid solution (x = 0, 0.5, 1, 1.5, 2) can be seen in Figure 4.6. Upon substitution of Ni^{2+} with Cu^{2+}, there are compositionally dependent magnetic contributions from both ions. It is noticed that the short-range antiferromagnetic interactions at low temperature are still present until x = 2, where we only have the $Na_3Cu_2SbO_6$ parent compound with a spin gap behavior. The μ_{eff} linearly decreases from 4.45 μ_B for the Ni^{2+} parent phase to 2.33 μ_B of the Cu^{2+} parent phase. These results agree with the μ_{theor} for each composition in this $Na_3Ni_{2-x}Cu_xSbO_6$ solid solution for every x = 0 – 2 in increments of 0.5.

The magnetic behavior of the $Na_3Cu_{2-x}M_xSbO_6$ phases (M = Mg or Zn) is shown in Figure 4.7a-b. The spin gap behavior of the $Na_3Cu_2SbO_6$ parent compound is completely suppressed upon 25% substitution of the non-magnetic ions. This is also noticed in the $Na_3Ni_{2-x}Cu_xSbO_6$ solid solution. The Cu^{2+} dilution lowers the influence of Cu – Cu dimer formations in the Cu_2SbO_6 layer. The substitution of Cu^{2+} with other elements disturbs the formation of Cu – Cu dimers and completely disrupts any possibility of the spin gap behavior. The μ_{eff} for the $Na_3Cu_{2-x}M_xSbO_6$ (M

= Mg, Zn) solid solutions for every x = 0 up to x = 1.5, in increments of 0.5, decreases linearly in accordance with μ_{theor}.

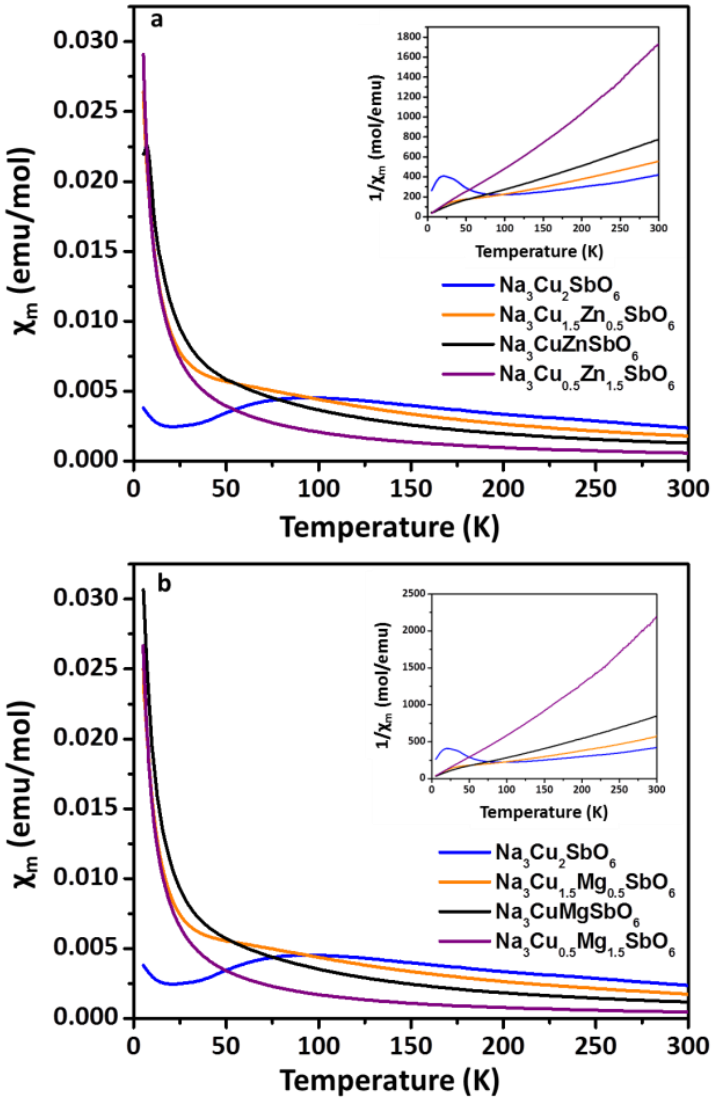

Figure 4.7a-b Magnetic susceptibility, χ vs. T, for $Na_3Cu_{2-x}M_xSbO_6$ (M = Mg, Zn) with an inset showing the 1/χ vs. T plot for these solid solutions. The high temperature data follows the Curie-Weiss law and is fit using χ = C/(T – θ) from 150 – 300 K to determine the μ_{eff} for each composition. The spin gap behavior present due to the $Na_3Cu_2SbO_6$ phase (blue line) disappears upon substitution.

The magnetic behavior of $Na_3Ni_{2-x}M_xSbO_6$ (M = Mg, Zn) phases is shown in Figure 4.8a-b. The substitution of the Ni^{2+} with non-magnetic M^{2+} cations involves a linear dilution of the magnetic moment. The resulting μ_{eff} for every x = 0.5 for each non-magnetic ion is in agreement with the theoretical moment for each composition. The long-range antiferromagnetic interaction at low temperature is suppressed with 25% substitution of the non-magnetic ions and is completely gone with higher substitution. This is in agreement with the $Li_3NiM'BiO_6$ (M' = Mg, Zn) magnetic susceptibility results and helps conclude that the antiferromagnetic ground state is from the $Ni^{2+} – O – Ni^{2+}$ interactions.[5]

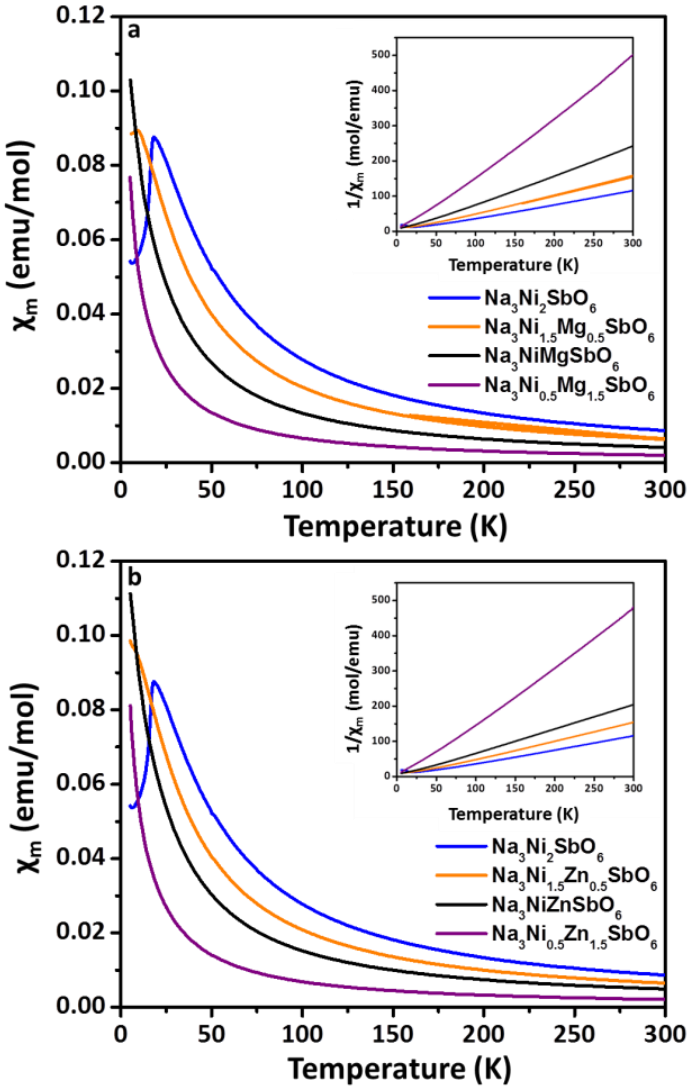

Figure 4.8a-b Magnetic susceptibility, χ vs. T, for $Na_3Ni_{2-x}M_xSbO_6$ (M = Mg, Zn) with an inset showing the 1/χ vs. T plot for these solid solutions. The high temperature data follows the Curie-Weiss law and is fit from 150 – 300 K by χ = C/(T – θ), to determine the μ_{eff} for each composition. The T_N present due to the $Na_3Ni_2SbO_6$ phase (blue line) slightly shifts to lower temperatures and disappears after 25% dilution with non-magnetic ions.

4.2.3 Optical Characterization:

Optical studies were performed in order to estimate the band gaps as the color change through the solid solutions indicates a change in this property. The Cu^{2+} and Ni^{2+} end members are green whereas the Mg^{2+} and Zn^{2+} are white. The diffuse reflectance raw data is transformed to absorbance using the Kubelka-Munk relation.[16] The band gap is estimated for each composition by extrapolating the x-intercept at the absorption onset in absorption vs. eV plot. Figure 9 includes the absorbance vs. eV spectra and Table 4.2 lists the estimated band gaps for each solid solution. It is noticed that the band gap can be tuned depending on the composition even between the white colors of the magnesium and zinc end members. All of the materials are insulating which is in agreement with the large band gaps extrapolated for these solid solutions.

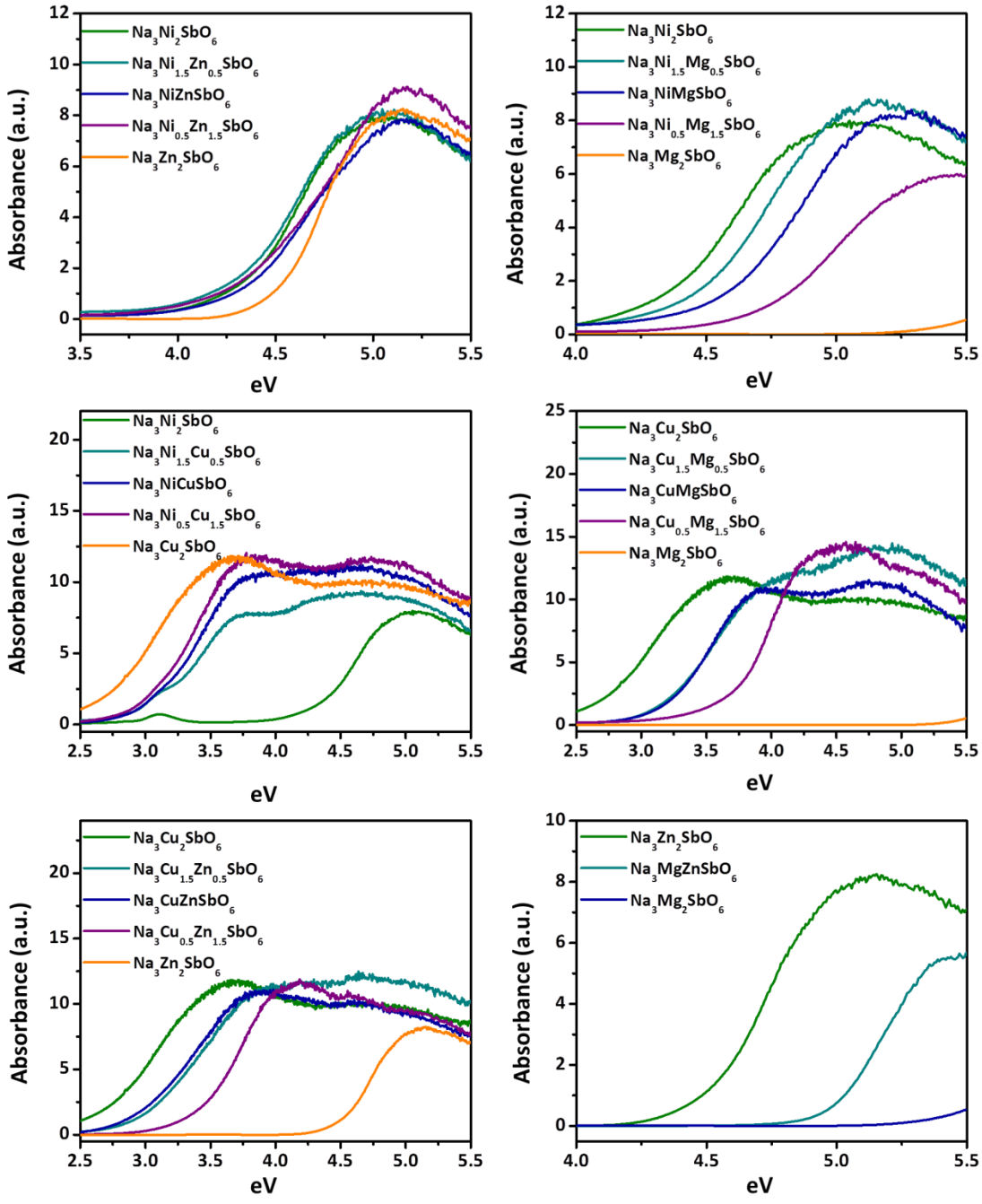

Figure 4.9 Transformed diffuse reflectance spectra in absorbance vs. eV for each $Na_3M_{2-x}M'_xSbO_6$ (M, M' = Cu, Mg, Ni, Zn) solid solution. The band gaps were extrapolated from the initial absorption onset to get the x-intercept.

Table 4.2 Estimated band gaps E_g (eV) extrapolated from transformed diffuse reflectance measurements. The band gaps are compositionally dependent.

Extrapolated Band Gaps (eV) for $Na_3M_{2-x}M'_xSbO_6$						
x	$Cu_{2-x}Zn_{x6}$	$Cu_{2-x}Mg_x$	$Ni_{2-x}Cu_x$	$Ni_{2-x}Zn_x$	$Ni_{2-x}Mg_x$	$Mg_{2-x}Zn_x$
0	2.62	2.62	4.29	4.29	4.29	5.38
0.5	2.89	3.11	2.86	4.20	4.41	-
1	2.86	3.13	2.98	4.28	4.49	4.97
1.5	3.37	3.65	2.98	4.25	4.66	-
2	4.49	5.38	2.62	4.49	5.38	4.49

4.3 Conclusions

This is the first report of the solid solutions for this $Na_3M_2SbO_6$ (M = Cu, Mg, Ni, Zn) family of compounds. The lattice parameter progression within the solid solutions follow an expected linear trend depending on the ionic size of the M^{2+} and M'^{2+} cations (M = Ni; M' = Mg, Zn). For the compositions containing the Jahn-Teller active Cu^{2+} ion the refined β angle decreases as expected upon the substitution of Mg^{2+}, Ni^{2+} and Zn^{2+}. The low temperature AFM transition for $Na_3Ni_2SbO_6$ disappears upon doping of the non-magnetic M^{2+} cations. The solid solution between Ni^{2+} and Cu^{2+} retain the low temperature antiferromagnetic interactions until the copper end member is reached. The spin gap behavior of $Na_3Cu_2SbO_6$ vanishes with minimal substitution of the other M^{2+}, as this behavior is attributed to ordered Cu – Cu dimers with the honeycomb structure. The estimated band gaps are large which agrees with the fact that these materials are all insulating at room temperature. It is important to explore all aspects of this family of compounds in light of the recent discoveries within this family. They show that these layered materials can be

extended to include a vast variety of stoichiometries and many different cations can achieve the honeycomb layering scheme seen in the compounds studied here.

4.4 Experimental Materials and Methods

Polycrystalline powder samples were prepared by solid state synthesis techniques. Sodium carbonate (Na_2CO_3, Spectrum Chemical 99.5%), antimony oxide (Sb_2O_3, J. T. Baker highly pure), copper oxide (CuO, Aldrich 99.99%), magnesium oxide (MgO, Alfa Aesar 99.95%), nickel oxide (NiO, Alfa Aesar 99.998%) and zinc oxide (ZnO, Aldrich 99.9%) were thoroughly ground together in the desired stoichiometric proportions. The sodium carbonate and the magnesium oxide were dried (120 °C and 900 °C respectively) prior to weighing to prevent moisture contamination. The pelletized samples were loaded onto an Au tray which was placed in an alumina boat. The samples were heated two times for 12 hrs at 900 °C (ramp rate of 5 °C min^{-1}) with intermediate grinding. After the heat treatment, the furnace was switched off and allowed to cool to room temperature before removal of the samples.

The powder samples were first characterized by X-ray diffraction (XRD) using a Rigaku Miniflex II diffractometer with Cu Kα radiation selected by a graphite monochromator on the diffracted beam. Powder samples were loaded onto an oriented Si single crystal “zero background” samples holder (MTI Corp.) to maximize he possibility of detecting minor impurity phases. Measurements were collected from 5° to 120° 2θ (step of 0.02°) with a 2 s fixed time.

Magnetism measurements were carried out on a Quantum Design physical property measurement system (PPMS) in the temperature range 3 – 300 K under a magnetic field of 1 T and zero field cooled conditions.

Diffuse reflectance measurements were carried out on packed powder samples with deuterium and halogen sources (200 – 1150 nm) passed through bifurcated fiber optic wire and magnesium oxide (MgO, Sigma Aldrich, 99.9%) as the white reference. The data was collected by the bifurcated optic cable and carried to an Ocean Optics HR4000 spectrophotometer. This setup is located in Oregon State University's Physics Department in Dr. David McIntyre's research group.[20]

4.5 Acknowledgement

Text and figures within this chapter have been used in part or whole from the publication:

Schmidt, W., Berthelot, R., Sleight, A.W., Subramanian, M.A., 2013. Solid solution studies of layered honeycomb-ordered phases O3–$Na_3M_2SbO_6$ (M = Cu, Mg, Ni, Zn). Journal of Solid State Chemistry 201, 178–185.

This work has been supported by NSF grant DMR 0804167. The authors want to thank Geneva Laurita (Oregon State University, Chemistry Department) for technical assistance during the optical measurements.

4.6 References

[1] R.D. Shannon, Acta Crystallogr., Sect. A: Found. Crystallogr. 32 (1976) 751.

[2] J. Bréger, M. Jiang, N. Dupré, Y.S. Meng, Y. Shao-Horn, G. Ceder, C.P. Grey, J. Solid State Chem. 178 (2005) 2575.
[3] V.V. Politaev, V.B. Nalbandyan, A.A. Petrenko, I.L. Shukaev, V.A. Volotchaev, B.S. Medvedev, J. Solid State Chem. 183 (2010) 684.
[4] O.A. Smirnova, V.B. Nalbandyan, A.A. Petrenko, M. Avdeev, J. Solid State Chem. 178 (2005) 1165.
[5] R. Berthelot, W. Schmidt, S. Muir, J. Eilertsen, L. Etienne, A.W. Sleight, M.A. Subramanian, Inorg. Chem. 51 (2012) 5377.
[6] V.B. Nalbandyan, M. Avdeev, M.A. Evstigneeva, J. Solid State Chem. 199 (2013) 62.
[7] J.M.S. Skakle, M.A. Castellanos R., S.T. Tovar, A.R. West, J. Solid State Chem. 131 (1997) 115.
[8] A. Boulineau, L. Croguennec, C. Delmas, F. Weill, Solid State Ionics 180 (2010) 1652.
[9] E. Climent-Pascual, P. Norby, N.H. Andersen, P.W. Stephens, H.W. Zandbergen, J. Larsen, R.J. Cava, Inorg. Chem. 51 (2011) 557.
[10] Y. Miura, R. Hirai, T. Fujita, Y. Kobayashi, M. Sato, J. Magn. Magn. Mater. 310 (2007) e389.
[11] Y. Miura, R. Hirai, Y. Kobayashi, M. Sato, J. Phys. Soc. Jpn. 75 (2006) 084707.
[12] H.-J. Koo, M.-H. Whangbo, Inorg. Chem. 47 (2007) 128.
[13] J. Xu, A. Assoud, N. Soheilnia, S. Derakhshan, H.L. Cuthbert, J.E. Greedan, M.H. Whangbo, H. Kleinke, Inorg. Chem. 44 (2005) 5042.
[14] E.A. Zvereva, M.A. Evstigneeva, V.B. Nalbandyan, O.A. Savelieva, S.A. Ibragimov, O.S. Volkova, L.I. Medvedeva, A.N. Vasiliev, R. Klingeler, B. Buechner, Dalton Trans. 41 (2012) 572.
[15] E.M. Seibel, J.H. Roudebush, H. Wu, Q. Huang, M.N. Ali, H. Ji, R.J. Cava, Inorg. Chem. 52 (2013) 13605.
[16] P. Kubelka, F. Munk,, Z. Tech. Phys. 12 (1931) 593.
[17] W. Schmidt, R. Berthelot, A.W. Sleight, M.A. Subramanian, Journal of Solid State Chemistry 201 (2013) 178.
[18] W. Schmidt, R. Berthelot, L. Etienne, A. Wattiaux, M.A. Subramanian, Materials Research Bulletin 50 (2014) 292.
[19] R. Berthelot, W. Schmidt, A.W. Sleight, M.A. Subramanian, Journal of Solid State Chemistry 196 (2012) 225.
[20] J.A. Russell, Measurement of Optical Bandgap Energies of Semiconductors, Master of Science in Physics, Oregon State University, 2011.

Chapter 5

Synthesis and Characterization of O3-$Na_3LiFeSbO_6$: A New Honeycomb-Ordered Layered Oxide

5.1 Introduction

Honeycomb ordered layered oxides are a growing family of compounds with many new compositions being reported. Zvereva *et al.* discovered Li_4FeSbO_6, where the $Li_{1/3}Fe_{1/3}Sb_{1/3}O_2$ slabs are mostly ordered in a honeycomb fashion isolating the SbO_6 octahedra from one another.[1] Also, Kumar et al. has synthesized and characterized many new layered compositions of $Li_8M_2Te_2O_{12}$ (M^{2+} = Co, Cu, Ni, Zn) and $Li_8M_2Sb_2O_{12}$ (M^{3+} = Al, Cr, Fe, Ga).[2] Another study into the heterovalent substitutions for M within the $Na_2M_2TeO_6$ layered oxides; Nalbandyan *et al.* discovered one new compound, $Na_2LiFeTeO_6$. These authors also investigated $Na_2NiMSbO_6$ (M = Al, Fe) but did not find a new honeycomb layered oxide.[3] Thus far the only successful report of heterovalent substitutions in the $Na_3M_2SbO_6$ family was by Politaev *et al*. who investigated the ternary phase diagram for Na_2O – Fe_2O_3 – Sb_2O_z and discovered Na_4FeSbO_6, a composition potentially related to the honeycomb layered structures. These authors also investigated the Ag exchange product and determined a composition of $Ag_3NaFeSbO_6$.[4]

This discussion is a report on the synthesis and characterization of a new compound in the honeycomb ordered layered oxide family, O3-$Na_3LiFeSbO_6$.

5.2 Results and Discussion

5.2.1: X-ray Diffraction

The powder X-ray diffraction pattern (PXRD) of $Na_3LiFeSbO_6$ indicates a single phase compound indexed to the monoclinic *C* 2/*c* space group (Figure 5.1), which is related to the $A_3M_2XO_6$ layered honeycomb ordered oxides. The chemical composition was analyzed by ICP-AES which confirmed $Na_3LiFeSbO_6$ with Na/Li = 3.00(5) as well as both Li/Fe and Fe/Sb close to 1. Lattice refinement using the Le Bail method gives the lattice parameters *a* = 5.3274(2) Å, *b* = 9.2049(2) Å, *c* = 11.377(3) Å and β = 108.47(1)°. The 18 – 33° 2θ reflections have a high sloping background, highlighted in the inset of Figure 5.1, indicative of a large degree of disorder and stacking faults within the layered structure. This PXRD pattern is similar to that of Na_4FeSbO_6 reported by Politaev et al.; however, they indexed the pattern to $P2_112$ space group which resulted in a mismatch of some super lattice reflections.[4] The PXRD pattern is shown in Figure 5.2 and we have successfully indexed this compound to the *C* 2/*c* space group with lattice parameters *a* = 5.4191(2) Å, *b* = 9.3977(2) Å, *c* = 11.530(3) Å and β = 108.35(1)°. The increase in lattice parameters for Na_4FeSbO_6 compared to $Na_3LiFeSbO_6$ is in good agreement with the difference in ionic radii of Na^+ (1.02 Å) and Li^+ (0.76 Å).[5]

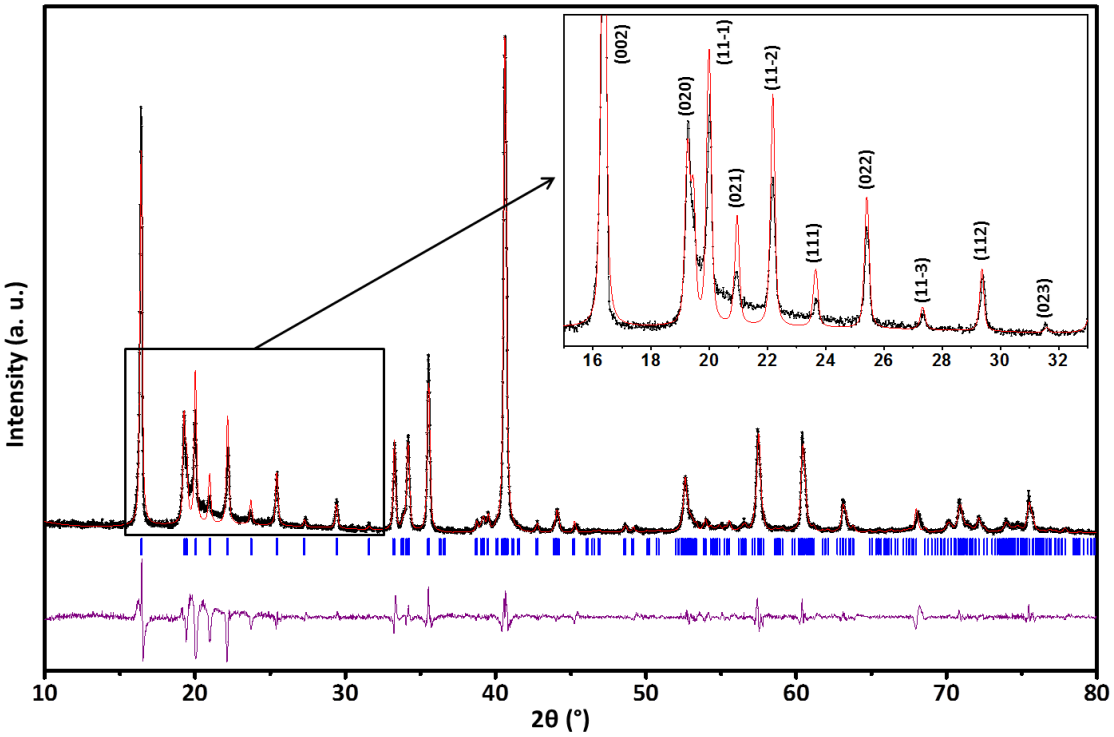

Figure 5.1 Experimental PXRD pattern of $Na_3LiFeSbO_6$ (experimental, calculated and difference profiles respectively as black, red and purple lines; Bragg positions shown with blue ticks). The large sloping background from 18 to 33° 2θ (highlighted in the inset) indicates there are stacking faults and a high degree of disorder in the structure.

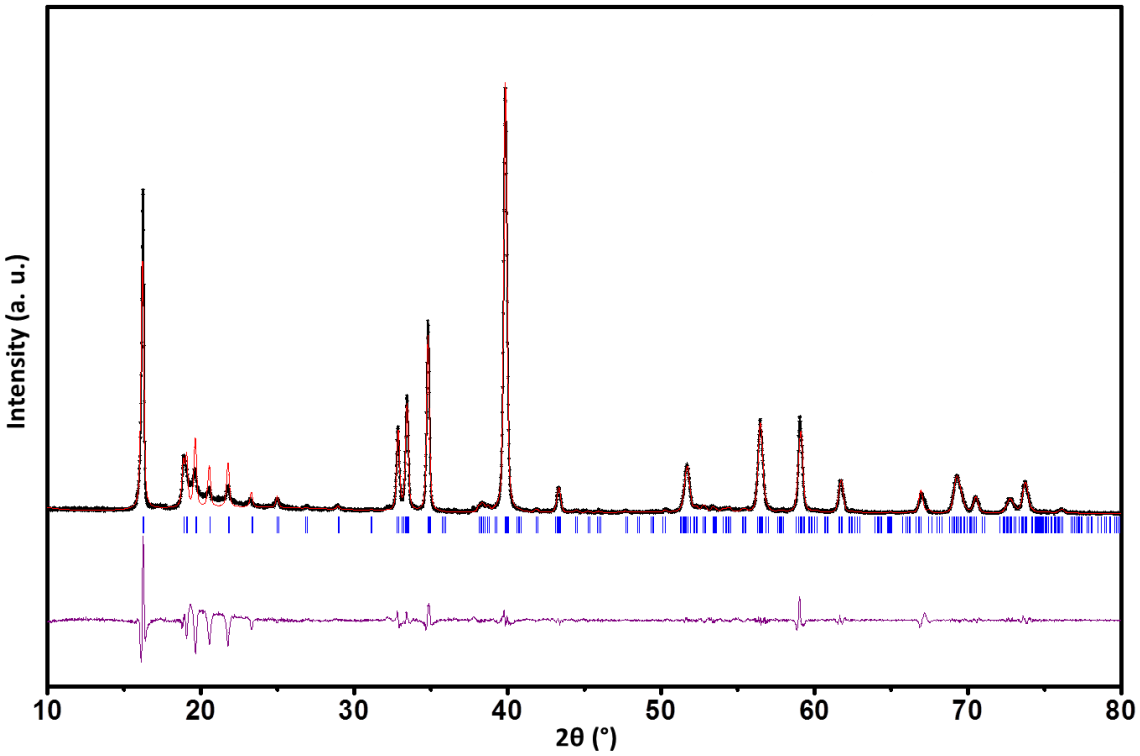

Figure 5.2 PXRD pattern for Na_4FeSbO_6. Experimental data, calculated fit, difference and Bragg positions are black stars, red, purple and blue lines respectively.

Although a complete structural analysis is difficult for disordered materials, this compound can be related to the honeycomb layered oxide materials. The slab ordering and monoclinic structure of $Na_3LiFeSbO_6$ are shown in the upper and lower images of Figure 5.3. The $LiFeSbO_6$ slabs are ordered in such a way that the SbO_6 octahedra are separated from one another according to Pauling's rules for edge sharing octahedra.[6] The honeycomb pattern around the SbO_6 is a disordered arrangement of Li and Fe indicated in the top image of Figure 5.3. This disorder is further investigated by ^{57}Fe Mössbauer spectroscopy to be discussed later. The

slabs are separated by the Na^+ ions located in octahedral positions between the slabs.

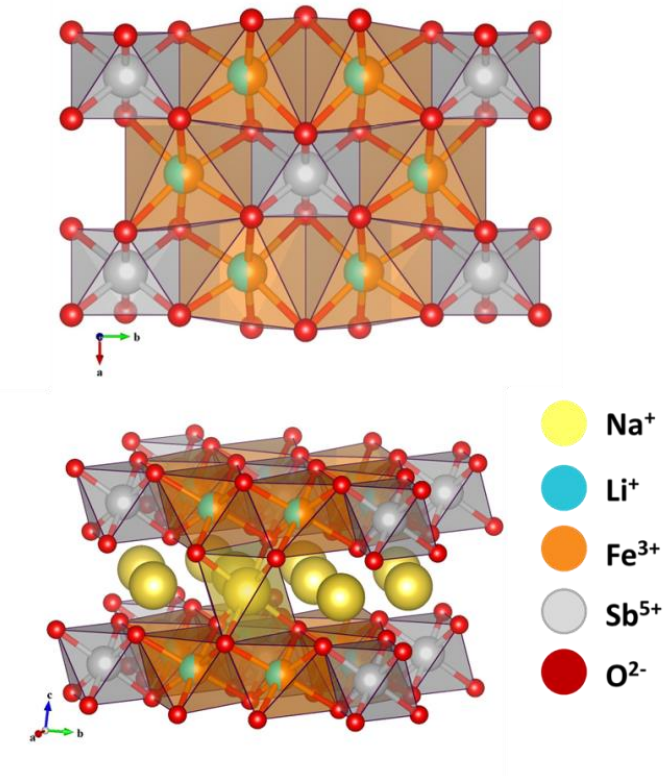

Figure 5.3 Ideal honeycomb arrangement within the slabs of $AM_{2/3}X_{1/3}O_2$ materials. Top image illustrates possible disorder in the honeycomb arrangement in the quaternary layered oxide materials. The bottom image shows the monoclinic cell with the octahedral interlayer sites filled by Na ions.

In our attempt to study the solid solution of Na_4FeSbO_6 and Li_4FeSbO_6, only $Na_3LiFeSbO_6$ was formed phase pure, whereas the other intermediate compounds $Na_2Li_2FeSbO_6$ and $Li_3NaFeSbO_6$ resulted in two phase products made up of the parent compounds. These hypothetical compositions could result in two situations: a mixing of both Li^+ and Na^+ in the interslab space and in the slabs or Li^+ filling the interslab space while Na^+ occupies an octahedral position in the slabs. Such a configuration would be difficult when considering the large difference in the ionic

radii of Li^+ (0.76 Å) and Na^+ (1.02 Å) in the 6-fold coordination.[5,7] Although Li^+ is slightly larger than the Fe^{3+} (H.S. 0.645 Å) and Sb^{5+} (0.60 Å) it is more likely that it will sit within the slabs and Na^+ will fill the interslab space which helps stabilize $Na_3LiFeSbO_6$ and prevents the other compositions from forming.[5]

5.2.2: Magnetic Susceptibility

The ZFC DC magnetic susceptibility (χ_m) and inverse susceptibility ($1/\chi_m$) vs. temperature curves for $Na_3LiFeSbO_6$ and $Na_3NaFeSbO_6$ are shown in Figure 5.4 (left and right, respectively). The Curie-Weiss fit for $Na_3LiFeSbO_6$ from 150 – 300 K resulted in an effective moment of 5.84 μ_B which agrees with the spin-only theoretical moment of one Fe^{3+} (S = 5/2, $\mu_{theor.}$ = 5.92 μ_B). The negative Weiss constant (θ = -7.90 K) indicates the presence of antiferromagnetic short range interactions, although long range ordering is not detected for this compound down to 5 K in contrast to a reported antiferromagnetic transition at T_N = 3.6 K in $Li_3LiFeSbO_6$.[1] This lack of long range order indicates disorder in the FeO_6 arrangement preventing any long range or superexchange interactions. For comparison, the magnetic susceptibility of $Na_3NaFeSbO_6$ is provided and the Curie-Weiss fit resulted in a μ_{eff} = 5.73 μ_B. This again is in good agreement with the spin-only contributions for high spin Fe^{3+}. Long range ordering was not observed above 5 K and the positive Weiss constant (θ = 3.70 K) indicates short range weak ferromagnetic interactions.

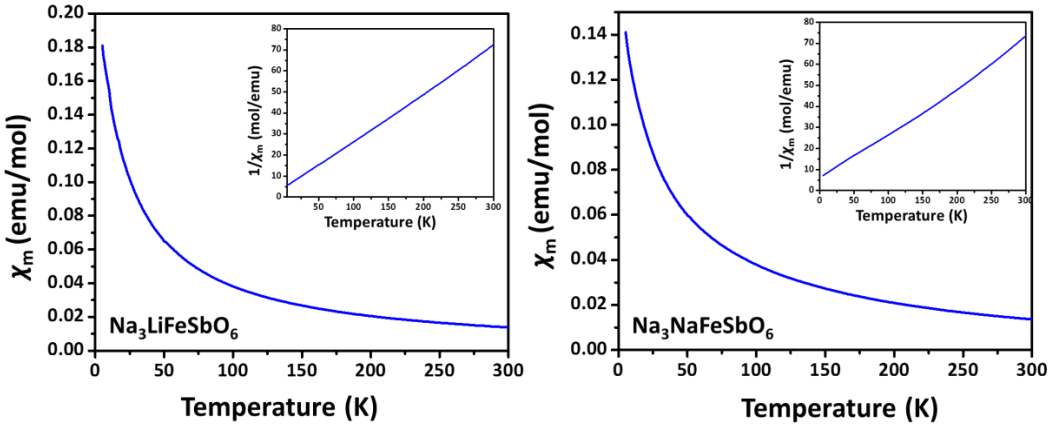

Figure 5.4 Magnetic susceptibility vs. temperature plots with inset plot of inverse magnetic susceptibility vs. temperature. The high temperature region 150 – 300 K was fit using the Curie-Weiss law $\chi_m = C/(T-\theta)$.

5.2.3: Mössbauer Spectroscopy

The ^{57}Fe Mössbauer spectrum for $Na_3LiFeSbO_6$ measured at room temperature indicates one paramagnetic doublet, Figure 5.5. Upon initial fitting of the data assuming a Lorentzian profile, the obtained Mössbauer parameters were δ = 0.343 mm/s, Γ = 0.33 mm/s and Δ = 0.53 mm/s. The isomer shift (δ) is characteristic for high-spin Fe^{3+} in an octahedral position. Thus, this preliminary fit using Lorentzian profile lines allowed the characterization of one doublet assigned to an iron that is in accordance with the expected crystallographic site. Nevertheless, the calculation led to a slightly larger value of linewidth compared to the value of the experimental width (Γ_{exp} = 0.25 mm/s) suggesting the existence of quadrupolar splitting distribution which may be associated to a local cationic disorder around the Fe nucleus. Thus, a second computation allowed the analysis of

spectra in terms of quadrupolar splitting distribution.[8] For this calculation, the half-height width Γ was fixed at 0.25 mm/s and the isomer shift was fixed at the value determined in the first treatment. The result of the refinement is shown in Figure 4. The average quadrupolar splitting determined by the second fitting is Δ = 0.59 mm/s and the width of this distribution confirms the existence of a cationic disorder around Fe. This is in agreement with the disorder evidenced in the PXRD pattern. The value of mean quadrupolar splitting is somewhat high indicating a slight deformation of the FeO_6 octahedron resulting from the difference in ionic radii of its neighbors Li^+ and Sb^{5+}.

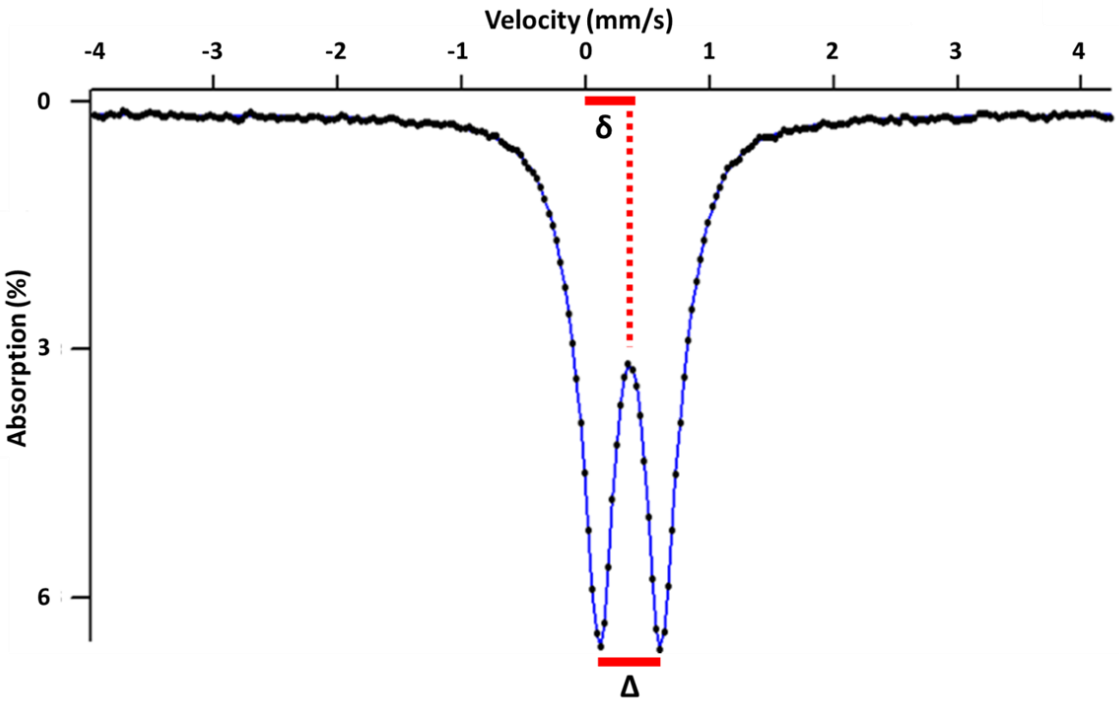

Figure 5.5 ^{57}Fe Mössbauer spectra for $Na_3LiFeSbO_6$ (black dotted line) and the calculated fit (blue solid line).

5.2.4: Optical Characterization

Diffuse reflectance measurements were carried out on $Na_3LiFeSbO_6$ and Na_4FeSbO_6 compositions, both of which are a light shade of orange when finely ground. The diffuse reflectance data was transformed to absorbance using the Kubelka-Munk relation.[9] Figure 5.6 shows the absorbance vs. eV spectra for the two compositions. The band gaps were estimated by extrapolating the absorption onset to the x-axis. The resulting band gaps were 3.19 eV and 3.18 eV for $Na_3LiFeSbO_6$ and Na_4FeSbO_6, respectively.

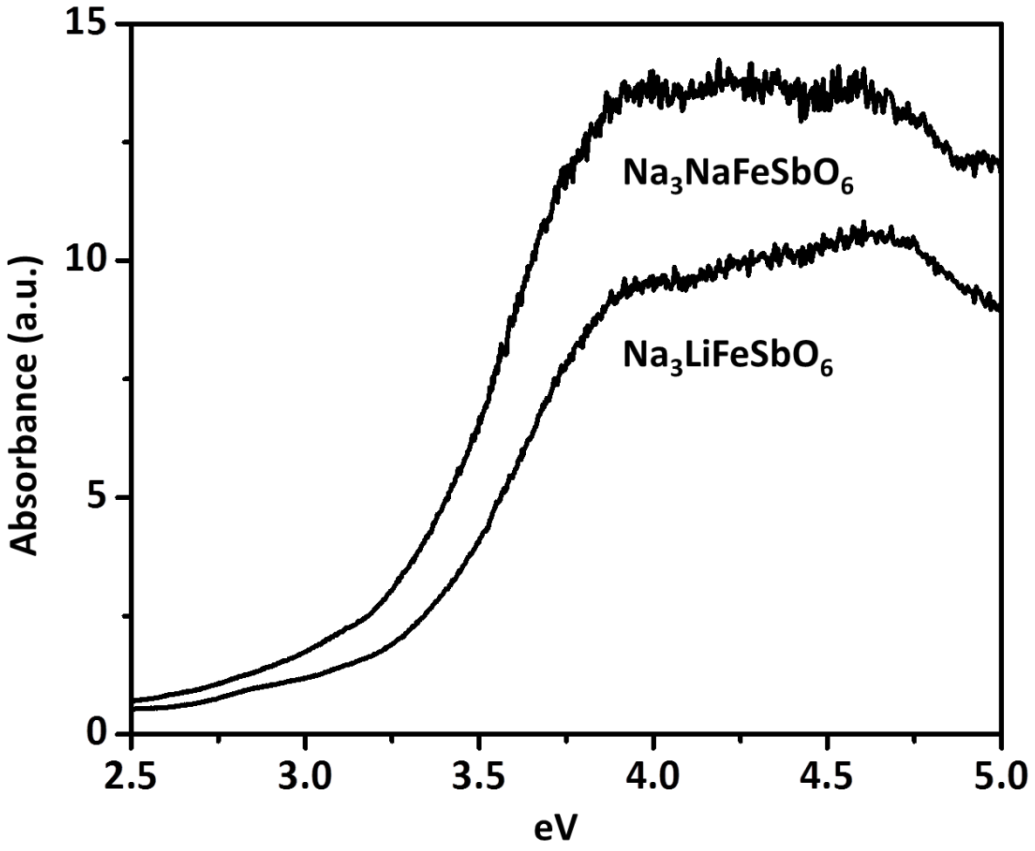

Figure 5.6 Diffuse reflectance measurement transformed to absorbance vs. eV for powder samples $Na_3LiFeSbO_6$ and $Na_3NaFeSbO_6$. The band gaps were estimated by extrapolating the x-intercept from the absorption onset.

5.2.5 Ion Exchange Compound

The refined lattice parameters for the ion exchange product $Ag_3LiFeSbO_6$ determined by Le Bail fitting to space group $P3_112$ were found to be a = 5.3289(2) Å and c = 18.732(1) Å. Comparison to the cell parameter values reported by Politaev et al. for $Ag_{2.5}Na_{1.5}FeSbO_6$ a = 5.450(1) Å and c = 18.775(2) Å are in agreement that the Na ions are exchanged by silver and there should be Li ions left in the layers. The a parameter is the most affected by the difference in ionic size and the c parameter is mostly governed by the Ag ions. This PXRD retains the broadened region between 18° and 23° 2θ as is found in the parent compound $Na_3LiFeSbO_6$. $Ag_3LiFeSbO_6$ is the nominal composition identified as attempt to perform ICP was unsuccessful.

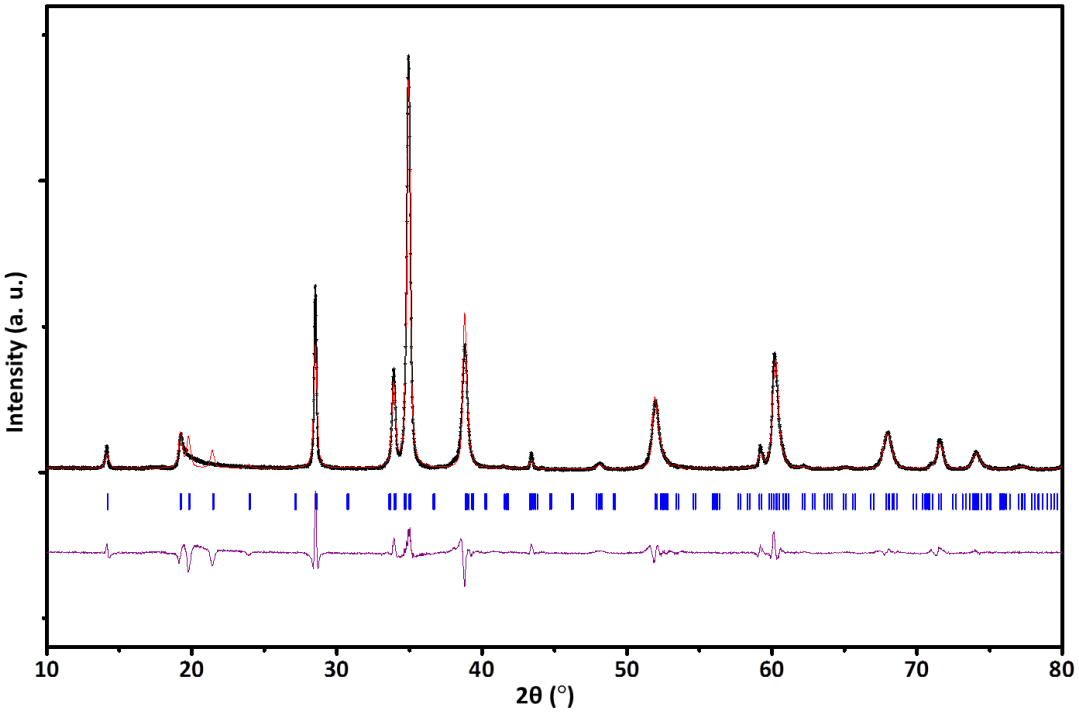

Figure 5.7 Experimental PXRD for the ion exchange product nominally $Ag_3LiFeSbO_6$.

5.3 Conclusions

In our search for compounds in the Na_4FeSbO_6 – Li_4FeSbO_6 system, a new composition $Na_3LiFeSbO_6$ was successfully obtained by solid state reaction. This layered oxide is characterized by a honeycomb ordering within the slab with each SbO_6 octahedron surrounded by LiO_6 and FeO_6 octahedra. This compound appears to be the only composition that forms between Na_4FeSbO_6 and Li_4FeSbO_6 as it is not possible to have Li^+ and Na^+ simultaneously in the interslab space. The monoclinic cell seems to be the best index for the XRD pattern; however, the presence of stacking faults may alter the fit and prevent a full refinement of the structure. This compound exhibits an effective magnetic moment in agreement with high spin Fe^{3+} assuming spin-only contributions. Long range magnetic ordering is not observed, as was not expected due to the high degree of disorder in this compound. ^{57}Fe Mössbauer spectroscopy indicates a cationic disorder around Fe verifying a random arrangement of Li and Fe in the honeycomb lattice.

5.4 Experimental Materials and Methods

Polycrystalline powder samples of $Na_3LiFeSbO_6$ and Na_4FeSbO_6 were prepared by solid state synthesis techniques. Sodium carbonate (Na_2CO_3, Spectrum Chemical 99.5%), antimony oxide (Sb_2O_3, J. T. Baker high purity) and lithium carbonate (Li_2CO_3, Aldrich 99.6%) were thoroughly ground together in the desired stoichiometric proportions. The sodium carbonate and lithium carbonate were

dried at 120 °C prior to weighing to prevent moisture contamination. The pelletized samples were loaded into an alumina boat and heated for 48 hrs at 1000 °C (ramp rate of 5 °C min^{-1}) with one intermediate grinding. After the heat treatment, the furnace was allowed to cool to room temperature before removal of the samples. Ion exchange samples were prepared by mixing silver nitrate ($AgNO_3$, Alfa Aesar 99.9%) in a 5:1 mole ratio to the parent compound $Na_3LiFeSbO_6$. This mixture was heated in a covered porcelain crucible at 250°C for 24 hours. The product was washed with ~800 mL of warm deionized water two times then collected via vacuum filtration. The powder product was then dried overnight at ~60°C.

The chemical compositions were determined by ICP-AES on a Varian 720 ES instrument. Powder samples (~10 mg) were dissolved in a high-quality hydrochloric acid solution heated at 70 °C with constant stirring. These measurements were performed by Laetitia Etienne at the CNRS, ICMCB – Bordeaux.

The powder samples were characterized by X-ray diffraction (XRD) using a Rigaku Miniflex II diffractometer with Cu Kα radiation selected by a graphite monochromator on the diffracted beam. Powder samples were loaded onto an oriented Si single crystal “zero background” samples holder (MTI Corp.) to maximize he possibility of detecting minor impurity phases. Measurements were collected from 5° to 120° 2θ (step of 0.02°) with a 2 s fixed time.

Zero field cooled (ZFC) DC magnetization data were collected with a Quantum Design Physical Property Measurement System (PPMS) using the ACMS mode. Measurements were collected from 5 to 300 K under a 0.5 T magnetic field.

Diffuse reflectance measurements were carried out on packed powder samples with deuterium and halogen sources (200 – 1150 nm) passed through bifurcated fiber optic wire and magnesium oxide (MgO, Sigma Aldrich, 99.9%) as the white reference. The data was collected by the bifurcated optic cable and carried to an Ocean Optics HR4000 spectrophotometer. This setup is located in Oregon State University's Physics Department in Dr. David McIntyre's research group.[10]

In order to evaluate Fe^{3+} local environments of the studied ferrite compounds, ^{57}Fe Mössbauer spectra were collected at 293 K. Both analyses are in transmission mode and were obtained with a conventional constant acceleration spectrometer (HALDER) with rhodium matrix source. As the samples contain about 10 mg natural iron per cm^3, the line broadening due to thickness of samples can be neglected. The spectra refinement was performed in two steps. First, the fitting of Mössbauer patterns as a series of Lorentzian profile peaks allowed the calculation of position (δ), amplitude and width (Γ) of each peak: thus, experimental hyperfine parameters were determined for the various iron sites. Second, spectra analysis was made in terms of quadrupolar splitting distribution P(Δ) with the Hesse and Rubartsch method [8]; Γ and δ were fixed at values determined in the first refinement. This method, which was used because of the line broadening notably observed, leads to a peak shape different from a Lorentzian profile which is characteristic of disordered compounds with a site distribution.

5.5 Acknowledgements

Portions of this chapter are directly used (text and figures) from the publication:

Schmidt, W., Berthelot, R., Etienne, L., Wattiaux, A., Subramanian, M.A., 2014. Synthesis and characterization of O3-$Na_3LiFeSbO_6$: A new honeycomb ordered layered oxide. Materials Research Bulletin 50, 292–296.

This work has been supported by NSF grant DMR 0804167.

5.6 References

[1] E.A. Zvereva, O.A. Savelieva, Y.D. Titov, M.A. Evstigneeva, V.B. Nalbandyan, C.N. Kao, J.-Y. Lin, I.A. Presniakov, A.V. Sobolev, S.A. Ibragimov, M. Abdel-Hafiez, Y. Krupskaya, C. Jähne, G. Tan, R. Klingeler, B. Büchner, A.N. Vasiliev, Dalton Trans. 42 (2013) 1550.
[2] V. Kumar, N. Bhardwaj, N. Tomar, V. Thakral, S. Uma, Inorg. Chem. 51 (2012) 10471.
[3] V.B. Nalbandyan, A.A. Petrenko, M.A. Evstigneeva, Solid State Ion. 233 (2013) 7.
[4] V.V. Politaev, V.B. Nalbandyan, Solid State Sci. 11 (2009) 144.
[5] R.D. Shannon, Acta Crystallogr. Sect. A 32 (1976) 751.
[6] L. Pauling, J. Am. Chem. Soc. 51 (1929) 1010.
[7] W.C. Sheets, E.S. Stampler, M.I. Bertoni, M. Sasaki, T.J. Marks, T.O. Mason, K.R. Poeppelmeier, Inorg. Chem. 47 (2008) 2696.
[8] J. Hesse, A. Rubartsch, J. Phys. [E] 7 (1974) 526.
[9] P. Kubelka, F. Munk,, Z. Tech. Phys. 12 (1931) 593.
[10] J.A. Russell, Measurement of Optical Bandgap Energies of Semiconductors, Master of Science in Physics, Oregon State University, 2011.

Chapter 6

New Layered Compounds with Honeycomb-Ordering: $Li_3Ni_2BiO_6$, $Li_3NiM'BiO_6$ (M' = Mg, Cu, Zn) and the delafossite $Ag_3Ni_2BiO_6$

6.1 Introduction

In their report on the honeycomb-ordered layered phase $Li_3Zn_2SbO_6$, Greaves et al. briefly mentioned the synthesis of an isostructural $Li_3Zn_2BiO_6$ phase, but they did not study it in detail.[1] It is to our knowledge the only Bi^{5+} - based compound in the $A_3M_2XO_6$ family. Following this work, we tried to complete the $Li_3M_2BiO_6$ series with M standing for all the above-mentioned divalent cations. In this paper, we report the first synthesis and the first characterizations of a new honeycomb-ordered layered $Li_3Ni_2BiO_6$ phase and substituted $Li_3NiM'BiO_6$ (M' = Mg, Cu and Zn) analogs, as well as a new delafossite $Ag_3Ni_2BiO_6$ prepared by topotactic ionic exchange following a molten salt method. The electrochemical properties of $Li_3Ni_2BiO_6$ as positive electrode material of Li-ion battery are also presented.

6.2 Results and Discussion

6.2.1 Structural Analysis

Greaves et al. reported the synthesis of $Li_3Zn_2BiO_6$ with a heat treatment at 600°C under oxygen flow.[1] By following these conditions with the nominal $Li_3Ni_2BiO_6$ composition, we obtained a dark green pellet and noticed a mass loss of approximately 10.5%. This value matches with the theoretical mass loss according to equation 1:

$3/2\ Li_2CO_3 + 2\ NiO + ½\ Bi_2O_3 + 5/2\ O_2 \rightarrow Li_3Ni_2BiO_6 + 3\ CO_2$ (1)

Figure 6.1 shows the XRD pattern of the final product. All the diffraction peaks can be indexed by a profile matching with the monoclinic space group *C*2/*m* and cell parameters *a* = 5.2581(4) Å, *b* = 9.116(1) Å, *c* = 5.1969(8) Å and β = 109.33°. The XRD pattern is very similar to that obtained for $Li_3Ni_2SbO_6$[2] and $Na_3Ni_2SbO_6$.[3] According to these observations, the formation of a $Li_3Ni_2BiO_6$ phase adopting the same layered structure with a Ni^{2+}/Bi^{5+} honeycomb ordering (FIGURE 6.2) can be assumed. In addition, ICP-AES analysis show the cationic ratios Ni/Bi ≈ 2 and Li/(Ni + Bi) ≈ 1, agreeing with the expected composition $Li_3Ni_2BiO_6$.

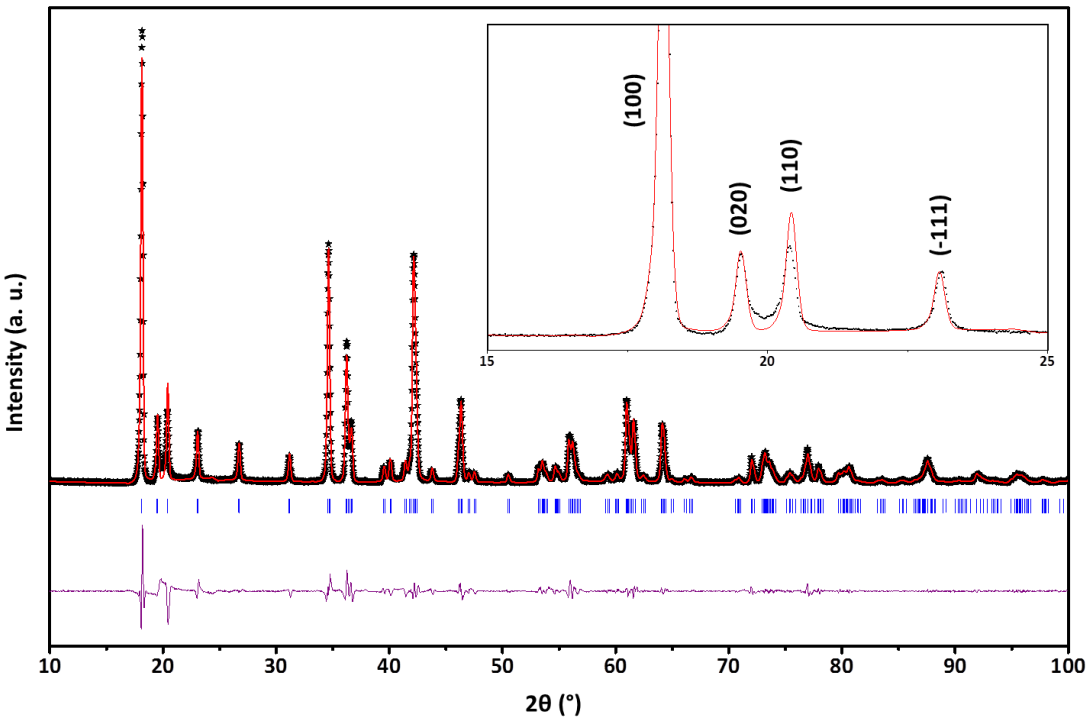

Figure 6.1 Experimental XRD pattern of $Li_3Ni_2BiO_6$ (observed, calculated and difference profiles, respectively as black stars and red and purple lines; Bragg positions as blue vertical lines). The inset focuses on the 15 - 25° 2θ region to highlight the peak broadening due to stacking faults which avoid a good profile fitting.

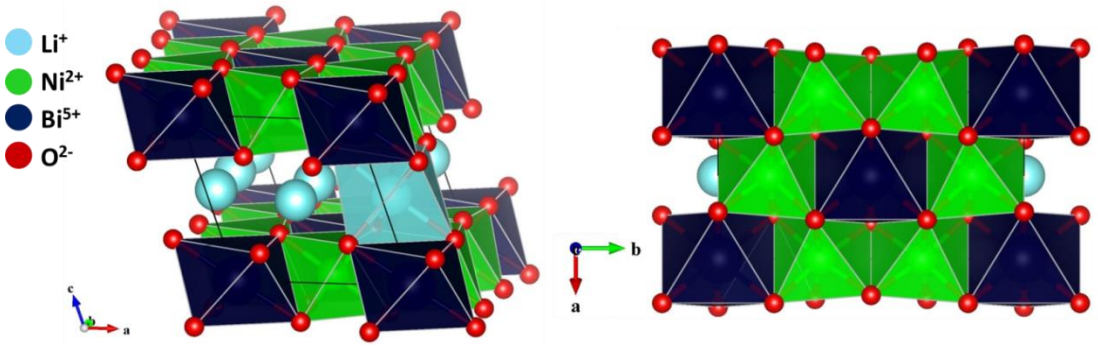

Figure 6.2 Structure of $Li_3Ni_2BiO_6$, monoclinic view (left) and top view for honeycomb ordering (right).

However, the profile of the XRD pattern could not be refined satisfactorily using a pseudo-Voigt function since some peaks exhibit significant asymmetric line broadening, especially in the 15 – 25° 2θ region (inset Figure 6.2). This phenomenon was already noticed for similar layered compounds, such as $Na_3Ni_2SbO_6$[3] and Li_2MnO_3,[4,5] for which it was found that stacking defects along the monoclinic *c* axis caused this broadening. In a recent study concerning Li_2MnO_3, Boulineau et al. observed that the broadening decreases progressively with an increase in temperature.[5] The synthesis temperature influence on the $Li_3Ni_2BiO_6$ XRD pattern was then studied for various temperatures from 550 to 900°C. With a long treatment at low temperature, the broadening is so significant that the diffractions peaks (020), (110), (-111) and (021) are convoluted in a unique asymmetric diffuse peak (Figure 6.3a-b). A decrease of the broadening was noticed for synthesis temperatures higher than 700°C; however, the final products are black and their XRD patterns show some impurities, especially $LiBiO_2$ and some lithium-doped nickel oxides (Figure 6.3a-b).

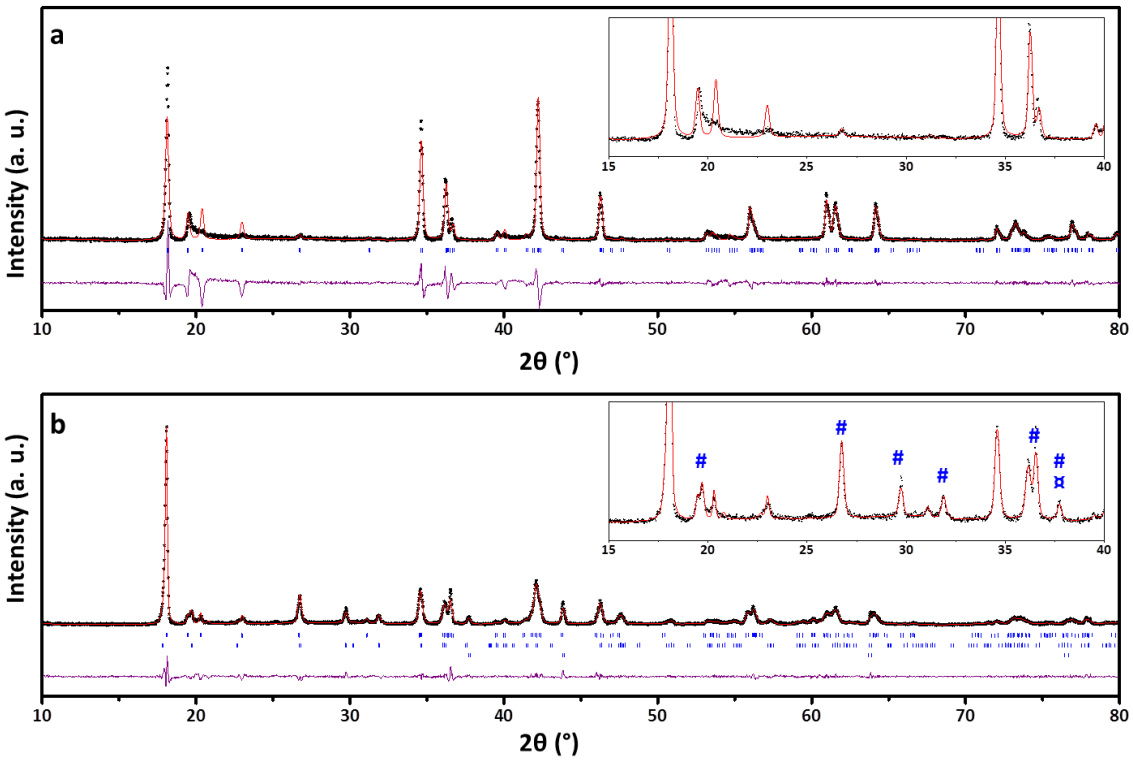

Figure 6.3 Experimental XRD patterns of $Li_3Ni_2BiO_6$ obtained (a) after 24 h at 500°C and (b) after 12 h at 900°C. In the first case, the broadening due to the stacking defects is important and one diffuse peak is clearly visible (inset for a), while at 900°C all the diffraction peaks are well defined but some impurities are already present (inset for b, # for $LiBiO_2$, ¤ for $Li_xNi_{1-x}O$ oxide). Observed, calculated and difference profiles are respectively in black stars, red and purple lines. Bragg positions are in vertical blue lines.

Table 6.1 presents the cell parameters of $Li_3Ni_2BiO_6$ and compares them to those of similar honeycomb-ordered layered compounds. It is observed that the increase of the cell parameters *a*, *b*, and *c* is directly related to an increase of the ionic radii of M^{2+} and/or X^{5+}: ie., the sum $r(M^{2+}) + r(X^{5+})$. As the Bi^{5+} ionic radius is larger than that of Sb^{5+},[6] $Li_3Ni_2BiO_6$ and $Li_3Zn_2BiO_6$ phases have larger cell parameters compared to those of phases containing the Sb^{5+} cation.

Table 6.1 Cell parameter comparison between different $Li_3M_2XO_6$ compounds.[a]

Composition	$r(M^{2+}) + r(M^{5+})$ (Å)	a (Å)	b (Å)	c (Å)	β (°)	Volume (Å^3)
Li_2MnO_3	1.29	4.937	8.532	5.030	109.46	199.8
$Li_3Ni_2SbO_6$	1.29	5.1828	8.9677	5.1577	109.696	225.7
$Li_3Zn_2SbO_6$	1.34	5.259	9.036	5.209	110.49	231.9
$Li_3Ni_2BiO_6$	1.49	5.2581(4)	9.11691)	5.1969(8)	109.33(1)	235.1(9)
$Li_3Zn_2BiO_6$	1.50	5.344	9.221	5.255	109.57	245.0

[a]The ionic radii sums $r(M^{2+}) + r(M^{5+})$ are calculated using data from Shannon et al.[6]

SEM analysis was carried out in order to visualize the grain size and morphology of $Li_3Ni_2BiO_6$. As shown in Figure 6.4, the particle size distribution is relatively homogeneous with an average size of less than 1 μm. The layered character that can be usually seen in some lamellar AMO_2 compounds is not very significant here. However, the general flakelike grain shape is evident.

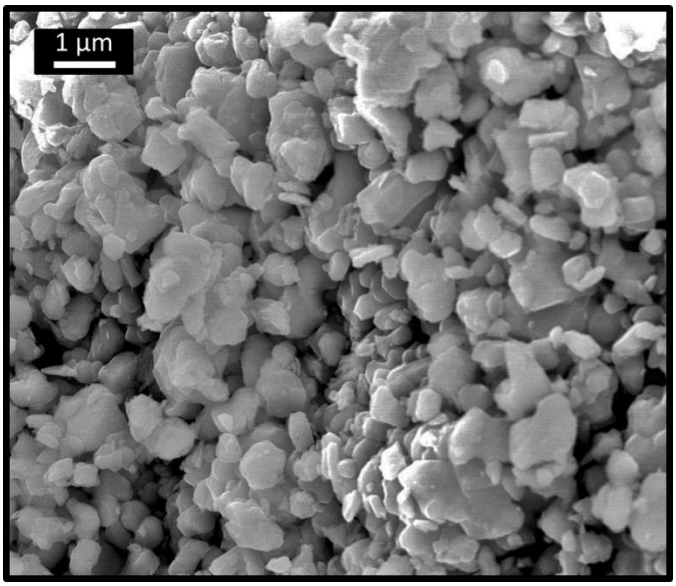

Figure 6.4 SEM picture of an $Li_3Ni_2BiO_6$ powder sample.

The presence of the light elements, lithium and oxygen, as well as the stacking defects prevents a reliable structural characterization by the Rietveld technique from the XRD patterns. That explains why only profile-matching refinements are provided in this study. However, it seemed interesting to try and quantify the stacking defects by simulating their influence on and XRD pattern. This was performed by Dr. Romain Berthelot with the DIFFaX program developed by Treacy and Newsam.[7] DIFFaX requires defining primary blocks of $Li_3Ni_2BiO_6$ that are then stacked following right or faulted vectors. Following previous works on Li_2MnO_3,[4,5] a unique type of block constituted by a slab and an interslab space has been considered. The experimental cell parameters of $Li_3Ni_2BiO_6$ are coupled with the atomic positions from $Li_3Ni_2SbO_6$.[1] Each block was then stacked over the previous one according to three possible vectors, (0; 0; 1), (1/2; -1/6; 1) and (1/6; -1/6; 1) in the monoclinic system. The exclusive occurrence of one of these vecotrs leads to a perfect stacking, while their alternation involves stacking defects. Figure 6.5 presents the simulated XRD patterns from an ideal to a completely disordered structure (i.e., from 0 to 100% of defects). A broadening of all the diffraction peaks (except the 00*l* ones) is clearly evident. In the same time the intensity of the (110), (-111), (021) and (111) peaks significantly decreases. The diffraction peak (110), which is more intense than (020) peak for the ideal $Li_3Ni_2BiO_6$, becomes smaller for more than 5% of stacking defects (Figure 6.5), which is in good agreement with what is experimentally observed in the inset of Figure 6.1. This simulation process enables us to estimate the stacking defects in $Li_3Ni_2BiO_6$ between 5 and 10%.

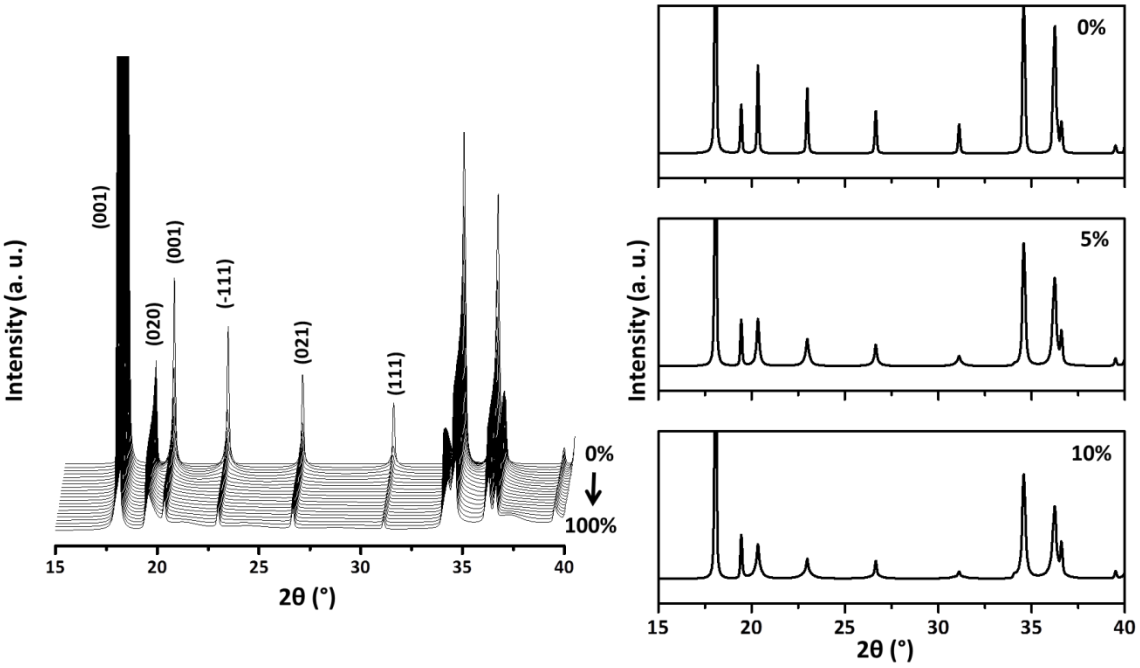

Figure 6.5 Simulated XRD patterns of $Li_3Ni_2BiO_6$ with stacking fault amounts from 0 to 100% (left) and for 0, 5 and 10% (right).

Ni^{2+} is not the only M^{2+} cation that can accommodate the octahedral site within the slabs in layered compounds. For example, with $Na_2M_2TeO_6$, M can be Mg, Mn, Co, Cu or Zn.[8,9] During our study, we were unable to reproduce the work of Greaves et al. to obtain a pure $Li_3Zn_2BiO_6$ phase, and our attempts for form other $Li_3M_2BiO_6$ (with M = Mg, Mn, Co, Cu) phases were not successful. Other compositions with a partial substitution of Ni^{2+} were then tried, especially the series $Li_3NiM'BiO_6$. The formation of single phases for the compositions $Li_3NiMgBiO_6$, $Li_3NiCuBiO_6$ and $Li_3NiZnBiO_6$ is clearly shown by XRD (Figure 6.6). No extra peaks that could be linked to an additional Ni^{2+}/M'^{2+} ordering within the honeycomb lattice are visible. The M'^{2+} cations are randomly located in the same site of the Ni^{2+}

cations, and there is no intermixing with Bi^{5+} cations. The peak broadening observed for $Li_3Ni_2BiO_6$ at low 2θ angles is also present in the XRD patterns; therefore, a small amount of stacking faults can be assumed for all these $Li_3NiM'BiO_6$ phases. All powder samples are dark green.

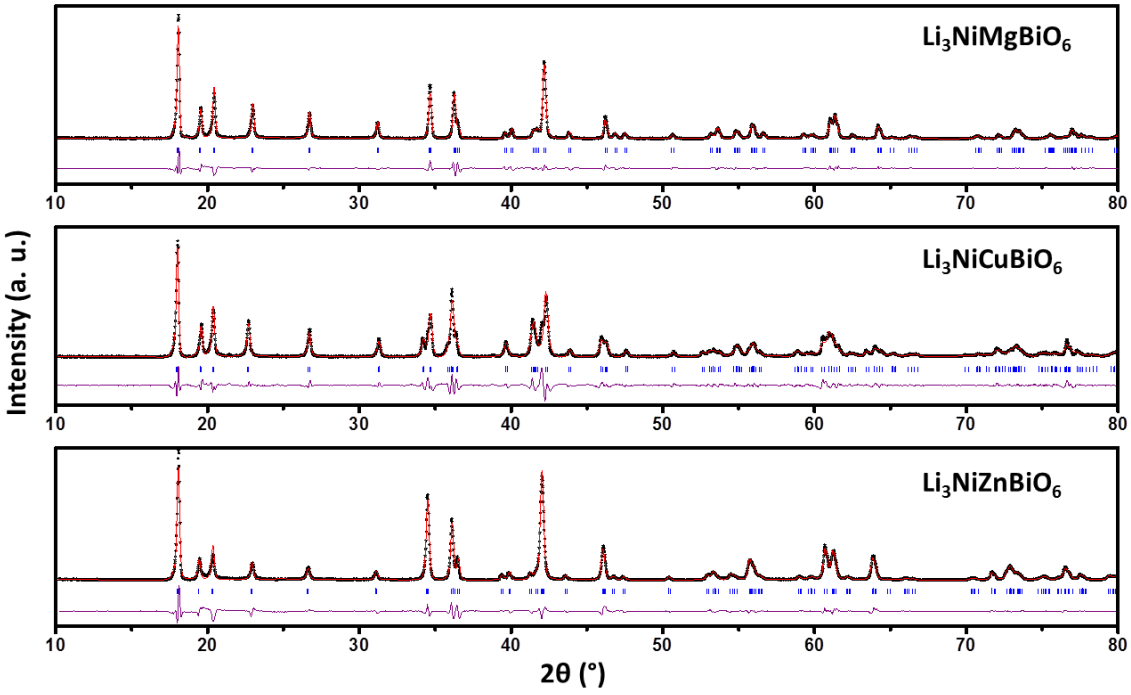

Figure 6.6 Experimental XRD patterns of a) $Li_3NiMgBiO_6$, b) $Li_3NiCuBiO_6$ and c) $Li_3NiZnBiO_6$. Observed, calculated and difference profiles are given respectively by black stars and red and purple lines. Bragg positions are given by blue vertical lines.

Table 6.2 presents the cell parameters of these three phases, obtained by profile-matching refinements using the same *C*2/*m* space group. As was observed in Table 6.1, the cell parameter evolution is related to the ionic radii of M^{2+}, M'^{2+} and Bi^{5+}. Therefore, for $Li_3NiM'BiO_6$ phases, the substitution of half the Ni^{2+} cations by slightly larger cations, such as Mg^{2+}, Cu^{2+} and Zn^{2+},[6] translates to greater unit cell

parameters. This general cell parameter trend is, however, not fully respected for $Li_3NiCuBiO_6$, which is indeed characterized by larger *a* and *c* and smaller *b* parameters and a significantly different β angle. This result may be related to an active Janh-Teller effect of the Cu^{2+} involving local CuO_6 octahedral distortion.

Table 6.2 Cell parameters of different $Li_3NiM'BiO_6$ phases (space group *C*2/*m*) and comparison with the $Li_3Ni_2BiO_6$ and $Li_3Zn_2BiO_6$.[a]

Composition	$r(Ni^{2+}) + r(M^{2+})$ Å)	a (Å)	b (Å)	c (Å)	β (°)	Volume (Å^3)
$Li_2Ni_2BiO_6$	1.38	5.2581(4)	9.11691)	5.1969(8)	109.33(1)	235.1(9)
$Li_3NiMgBiO_6$	1.41	5.2612(7)	9.097(1)	5.2212(6)	109.62(1)	235.4(9)
$Li_3NiCuBiO_6$	1.42	5.314(1)	9.087(2)	5.269(1)	110.55(1)	238.2(9)
$Li_3NiZnBiO_6$	1.43	5.2831(8)	9.150(1)	5.226(1)	109.61(1)	237.9(9)
$Li_3Zn_2BiO_6$	1.48	5.344	9.221	5.255	109.57	245.0

[a]The ionic radii sums $r(Ni^{2+}) + r(M'^{2+})$ are calculated using data from Shannon et al.[6] The cell parameter evolution follows a regular trend according to the different ionic radii, except for $Li_3NiCuBiO_6$.

6.2.2 Magnetism

In the $Li_3Ni_2BiO_6$ and $Li_3NiM'BiO_6$ (with M' = Mg, Zn) phases, only the Ni^{2+} cations ($3d^8$, S = 1) contribute to the magnetic behavior, whereas in $Li_3NiCuBiO_6$, Cu^{2+} cations ($3d^9$, S = ½) also contribute. The temperature-dependent magnetic susceptibility data for a polycrystalline sample of $Li_3Ni_2BiO_6$ are shown in Figure 6.7. It exhibits a general paramagnetic behavior and the inverse of the magnetic susceptibility follows a linear trend that has been fitted between 150 and 300 K with the Curie-Weiss law $\chi = C/(T - \theta)$. The effective magnetic moment μ_{eff} is 4.34 μ_B (i.e., 3.07 μ_B/Ni^{2+}), which is in good agreement with the theoretical value, assuming the magnetism results from Ni^{2+} cations with spin-only contributions (μ_{theor} = 4.00 μ_B, i.e.

2.83 μ_B/Ni^{2+}). The Weiss constant is positive (27 K) indicating ferromagnetic short-range interactions.

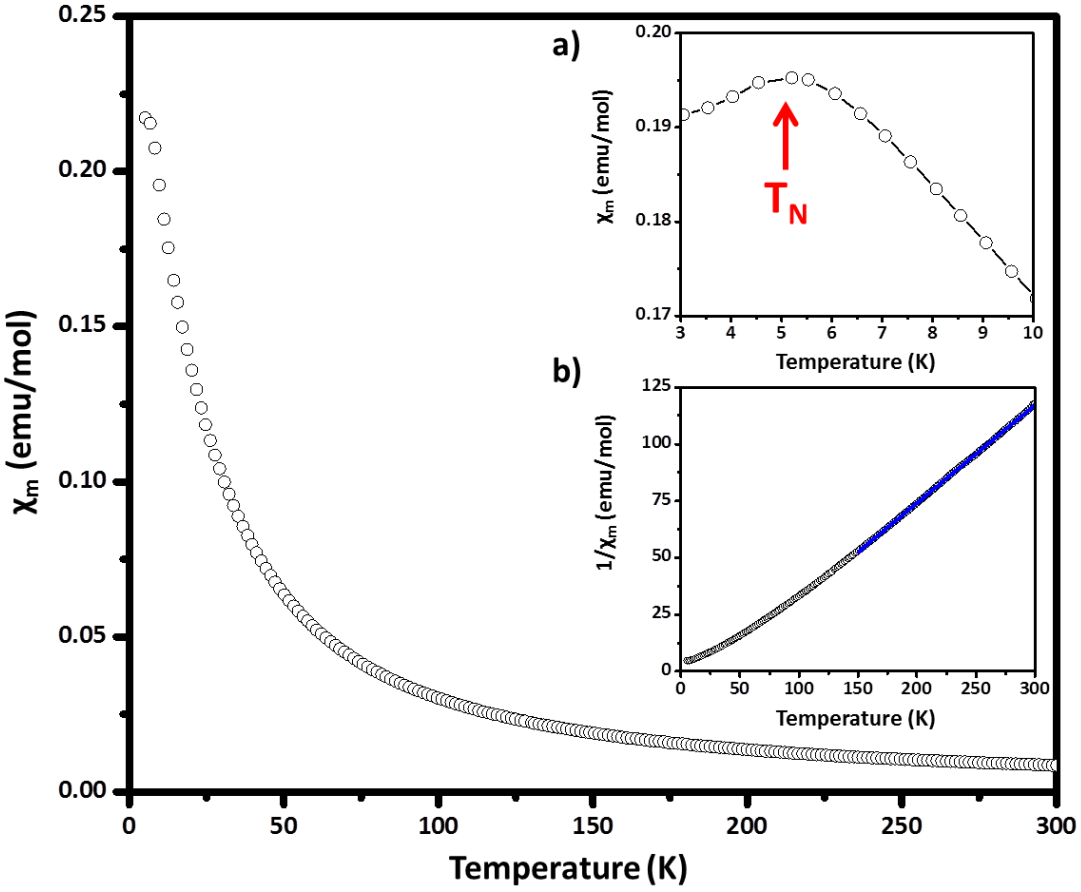

Figure 6.7 Magnetic susceptibility evolution in the temperature range 5 - 300 K for $Li_3Ni_2BiO_6$. The low-temperature AFM ordering is evienced in the inset (a). The linear evolution of the inverse susceptibility can be fitted using a Curie-Weiss law (inset (b), blue line).

The slightly higher experimental value of the effective moment can be explained by the spin-orbit coupling, which will often increase the observed moment in the case of elements with more than half-filled *d* orbitals.[10–13] In their recent study on the similar honeycomb-ordered layered $Li_3Ni_2SbO_6$ phase, Zvereva et al. observed an effective moment of 4.3 μ_B and found a significantly positive Weiss

constant (8 K),[2] which is in good agreement with the results obtained on $Li_3Ni_2BiO_6$. However, the authors used in their study and additional temperature-independent term χ_0 in their Curie-Weiss law fitting: $\chi = C/(T - \theta) + \chi_0$. For $Li_3Ni_2SbO_6$, the weak positive value of χ_0 was attributed to the predominance of Ni^{2+} Van Velck paramagnetic contributions over diamagnetic contributions. Therefore, magnetic data of $Li_3Ni_2BiO_6$ were fitted a second time taking into account this additional term. The resulting negative value of χ_0 slightly increases the total effective moment to 4.52 μ_B (Table 6.3) and demonstrates that Ni^{2+} Van Vleck paramagnetic contributions may not be as predominant as they are in $Li_3Ni_2SbO_6$. In addition, it is interesting to note that the total effective moment now matches well with that expected by using a Ni^{2+} moment of 3.2 μ_B, as in commonly observed in the literature.[11,14,15] At very low temperature, an antiferromagnetic ordering is present, with a maximum of the magnetic susceptibility (Néel temperature) around 5.5 K (Figure 6.7, inset a). This transition was also noticed in $Li_3Ni_2SbO_6$ at a slightly higher temperature (15 K).[2]

Table 6.3 Magnetic data obtained for $Li_3Ni_2BiO_6$ and $Li_3NiM'BiO_6$ phases from the Curie-Weiss law fitting from 150 to 300 K, with or without the temperature-independent term χ_0.

	$Li_2Ni_2BiO_6$	$Li_3NiMgBiO_6$	$Li_3NiCuBiO_6$	$Li_3NiZnBiO_6$
Theoretical Moment				
μ_{theor} based on spin-only contributions (μ_B)	4.00	2.83	3.32	2.83
μ_{theor} based on reported moments for Ni^{2+} (3.2 μ_B) and Cu^{2+} (1.9 μ_B)	4.52	3.2	3.72	3.2
Curie-Weiss Fitting				
Curie constant C (emu mol^{-1})	2.33(4)	1.005(1)	1.419(2)	1.042(1)
Weiss constant θ (K)	27.1(2)	37.4(2)	-0.7(2)	33.2(2)
fitting factor R^2 (%)	99.989	99.987	99.986	99.987
effective moment μ_{eff} (μ_B)	4.34	2.84	3.38	2.90
Curie-Weiss wih χ_0 Fitting				
Curie constant C (emu mol^{-1})	2.53(2)	1.06(1)	1256(3)	0.962(6)
Weiss constant θ (K)	20.1(6)	33.3(8)	11.3(2)	39.6(5)
χ_0 (10^{-4} emu mol^{-1})	-5.3(4)	-1.5(3)	3.99(9)	2.3(2)
fitting factor R^2 (%)	99.9996	99.99	99.999	99.9995
effective moment μ_{eff} (μ_B)	4.52	2.92	3.18	2.79

The temperature-dependent magnetic susceptibility data for polycrystalline samples of $Li_3NiM'BiO_6$ (M' = Mg, Cu, Zn) are shown in Figure 6.8. They all exhibit a paramagnetic behavior over the whole temperature range. As for $Li_3Ni_2BiO_6$, magnetic data were fitted following a Curie-Weiss law and the results are gathered in Table 6.3. For $Li_3NiMgBiO_6$ and $Li_3NiZnBiO_6$, elimination of half the nickel by nonmagnetic cations obviously decreases the total effective magnetic moment (2.84 and 2.90 μ_B, respectively). The values are close to the spin-only theoretical values as the spin-orbit coupling decreases with a lower amount of Ni^{2+}. In $Li_3NiCuBiO_6$, the experimental total effective moment value of 3.38 μ_B agrees with the assumption of Ni^{2+} and Cu^{2+} cations with spin-only contributions (μ_{theor} = 3.32 μ_B). The second Curie-Weiss fitting with the additional term χ_0 does not significantly modify the calculated values of the effective moments. The only noticeable change is the Weiss constant observed for $Li_3NiCuBiO_6$, which shifts to 11 K. This positive value is more

consistent with those obtained for $Li_3NiMgBiO_6$ and $Li_3NiZnBiO_6$. It is interesting to note that no antiferromagnetic ordering was evinced at very low temperature for all $Li_3NiM'BiO_6$ phases, which suggests that the antiferromagnetic ground state stems from $Ni^{2+} – O – Ni^{2+}$ interactions.

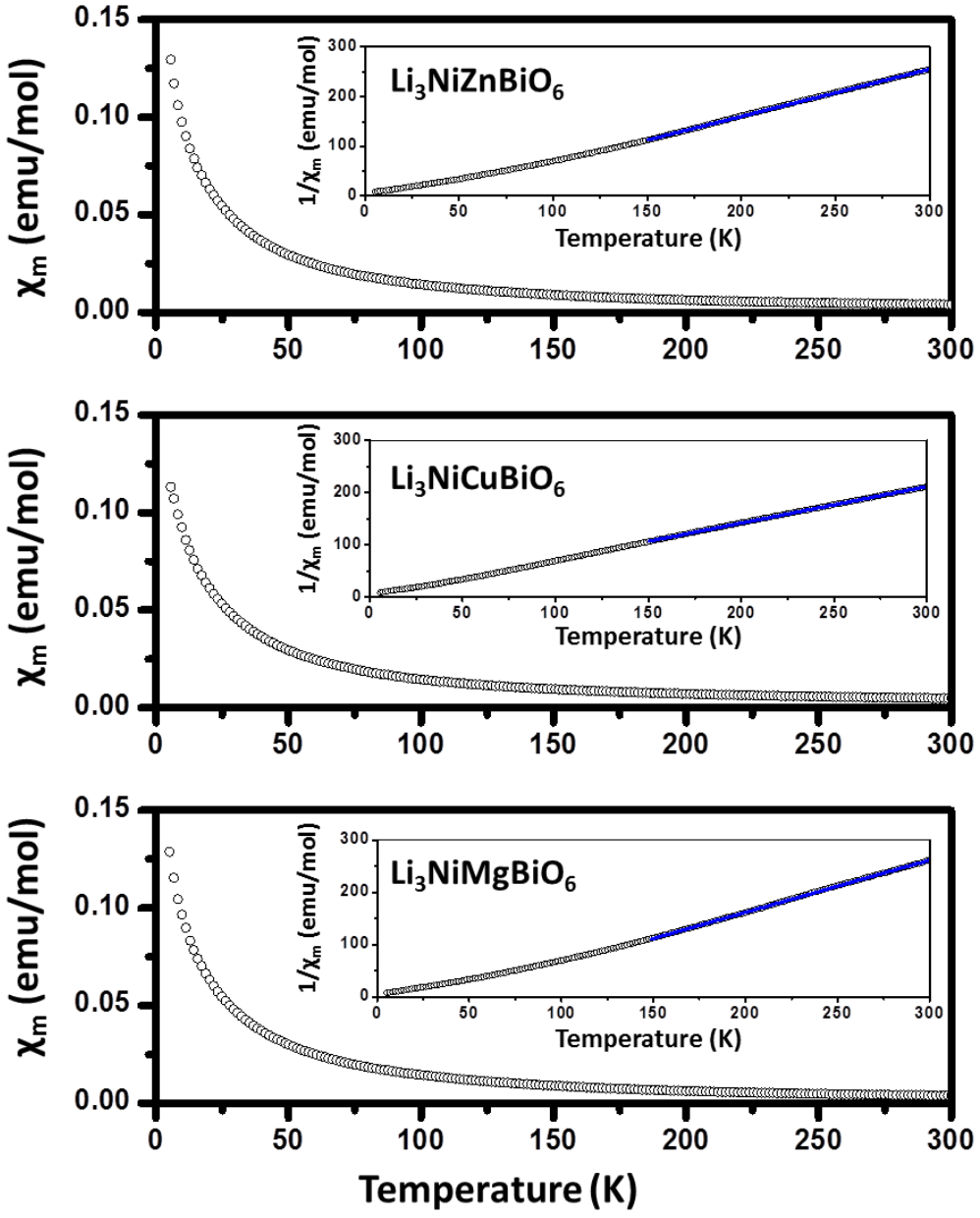

Figure 6.8 Magnetic susceptibility of substituted $Li_3NiMBiO_6$ (M^{2+} = Zn, Cu, Mg) compounds.

6.2.3 Electrochemistry

The layered structure with the presence in the slabs of Ni^{2+} cations that can be oxidized during lithium extraction allows an investigation of the electrochemical properties of $Li_3Ni_2BiO_6$. However, because of its high molar mass, the study represents more a fundamental interest. Figure 6.9 shows the first electrochemical cycling obtained in a galvanostatic mode with $Li_3Ni_2BiO_6$ as the positive electrode of a lithium battery. The initial potential of 3.37 V vs Li^+/Li dramatically drops by starting the cycling in discharge. Therefore, it appears impossible to intercalate lithium ions in the initial material, which confirms the $Li_3Ni_2BiO_6$ composition as totally filled in the interslab space. The electrochemical curve does not present any plateau during the cycling, showing that the material remains a single phase. Only 0.75 lithium ions can be extracted ruing the first charge up to 4.6 V vs Li^+/Li, while 0.45 can be intercalated in the first discharge. The first discharge capacity is 81.7mAh g^{-1}, which is significantly lower than a theoretical value of 181.5 mAh g^{-1} but very close to what was obtained for the similar honeycomb-ordered layered phase $Li_3Ni_2SbO_6$ (92 mAh g^{-1}).[16] After this first charge/discharge cycling, the capacity still decreases to 22 mAh g^{-1} after 10 cycles.

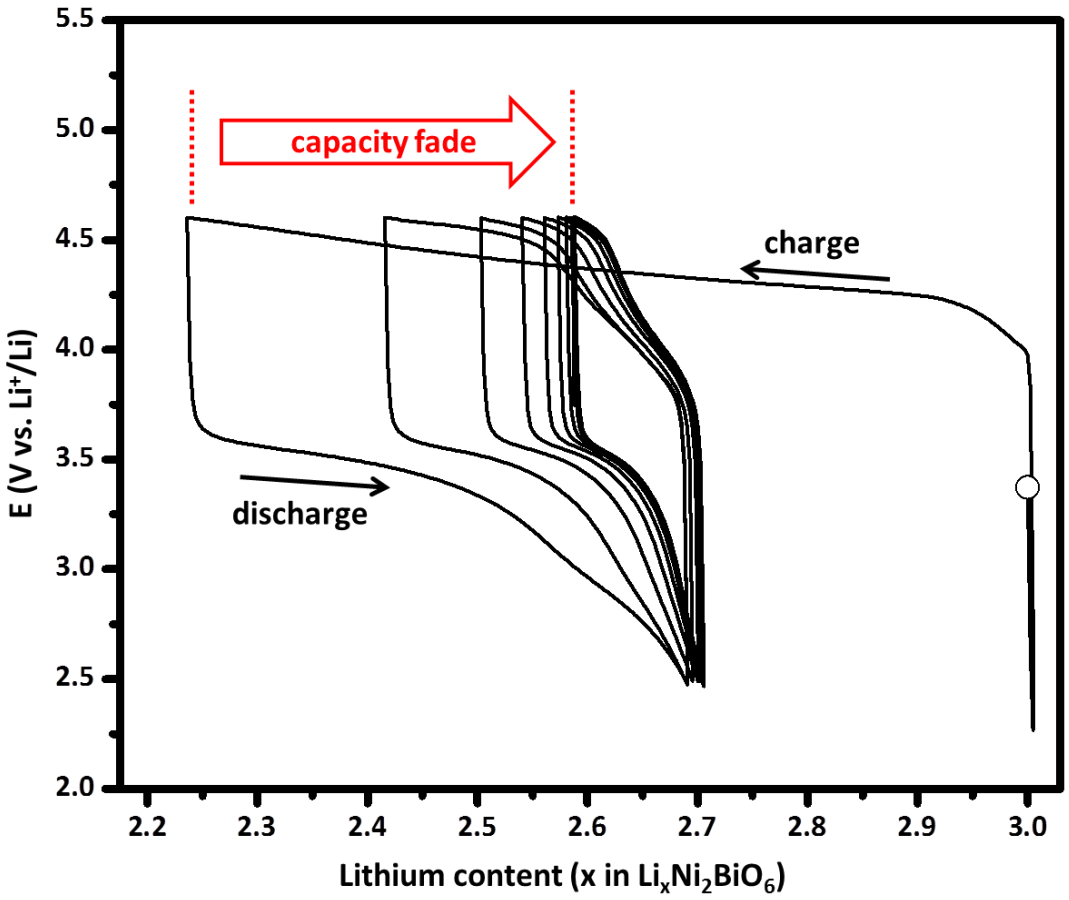

Figure 6.9 Electrochemical behavior of $Li_3Ni_2BiO_6$ as the positive electrode material of a lithium battery. The starting point is marked by the empty circle. The charge and discharge rate is C/20.

The electrochemical deintercalation and intercalation of lithium ions are possible; however, the capacity is very limited. In their study of the electrochemical properties of $Li_3Ni_2SbO_6$, Ma et al. reported that the Li/Ni interlayer mixing (originally negligible) dramatically increases up to 10% during the glavanostatic cycling.[16] The authors investigated the nickel migration into lithium vacancies and found a relatively low migration barrier which makes possible this Li/Ni mixing and leads to rapid capacity fade. Therefore, the capacity decrease observed for $Li_3Ni_2BiO_6$ can be explained by similar Li/Ni interlayer mixing.

6.2.4 Delafossite Exchange Product $Ag_3Ni_2BiO_6$

New structures obtained by topotactic ionic exchanges are known to be very influenced by the stacking nature of the precursor, especially the crystallographic site accommodated by A^+ cations. For example, three different $AgCoO_2$ polytypes can obtained by ion exchange usin O3-$LiCoO_3$, P2-Na_xCoO_2 or the mixed layered phase OP4-$Li_xNa_yCoO_2$.[17] In the case of delafossite $AgNiO_2$, topotactic exchanges from $ANiO_2$ precursors (A = Li, Na, K with an O3 stacking) lead to the rhombohedral polytype.[18–20] The hexagonal polytype can be alternatively prepared by coprecipitation method.[21]

The topotactic process can affect the slab positions, but any possible cation ordering within the slabs remains the same. This has been verified by Politaev et al. when they reported the synthesis of honeycomb-ordered $Ag_3Co_2SbO_6$ delafossite from the layered precursor $Na_3Co_2SbO_6$.[3] Indeed, an enlarged cell (compare to the hexagonal for $AgCoO_2$) was necessary to take into account the superstructure peaks related to the Co^{2+}/Sb^{5+} ordering.

In the present study the molten salt ion exchange was performed using $Li_3Ni_2BiO_6$ as the layered precursor. The final product obtained after washing and drying is black. The corresponding XRD powder pattern is shown in Figure 6.10. It can be indexed using the space group $P3_112$, the same as for $Ag_3Co_2SbO_6$. The cell parameters, obtained by profile-matching refinement, are a = 5.4012(8) Å and c = 18.795(4) Å. In comparison with $AgNiO_2$ delafossite (a = 5.090 Å and c = 18.37 Å, experimental values from Shin et al.[20] are adapted in an enlarged cell), the larger a

and *c* parameters are explained by the larger ionic radii, especially Bi^{5+}, but also Ni^{2+} in comparison to Ni^{3+}.[6] However, some weak impurity diffraction peaks of bismutite $Bi_2O_2(CO_3)$ are noticed in the XRD pattern (inset Figure 6.10). Also, a very small amount of the precursor $Li_3Ni_2BiO_6$ is still present. This result was expected as it is always very difficult to totally exchange Li^+ in the octahedral site by Ag^+ in a dumbbell configuration.[22] Preliminary ball milling of the $Li_3Ni_2BiO_6$ powder in order to reduce the grain size or repetition of the exchange treatment slightly improved the exchange yield, but it finally appeared impossible to exchange all of the precursor. ICP analysis shows a cationic ratio Li/(Ni + Bi) lower than 0.1. Therefore, more than 90% of the lithium ions have been exchanged during the molten salt treatment, which is a very acceptable yield.

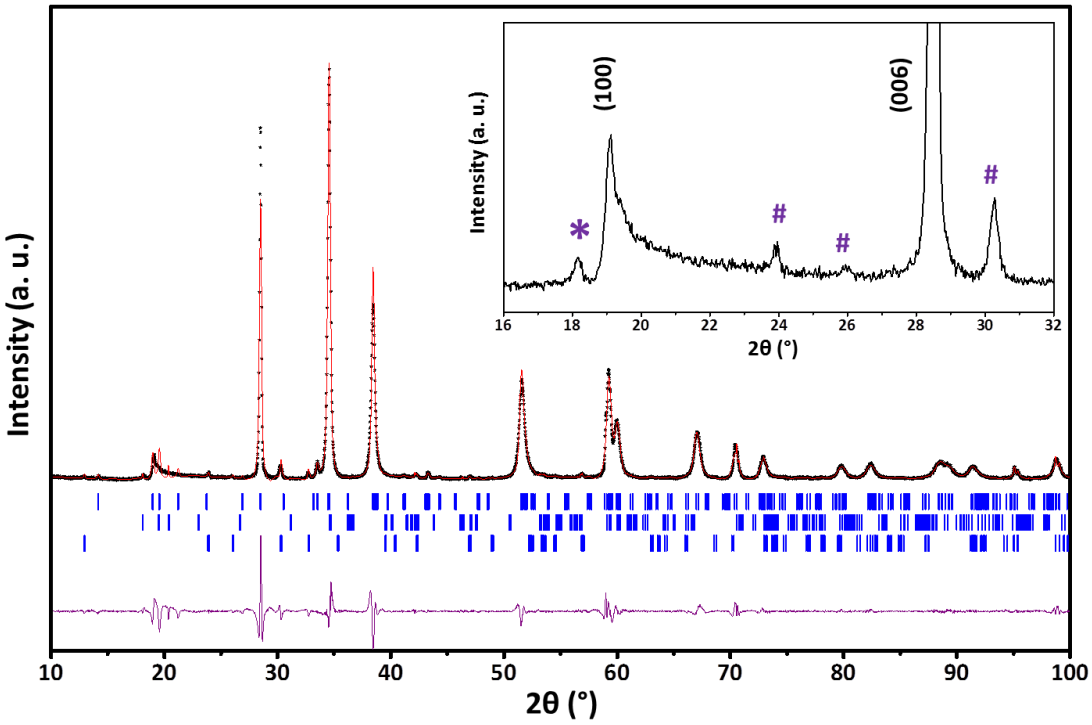

Figure 6.10 Experimental XRD pattern of $Ag_3Ni_2BiO_6$ (observed, calculated (profile matching) and difference profiles given respectively as black stars and red and purple lines; Bragg positions as blue vertical lines). The inset highlights the peak broadening on the right side of the (100), explained by stacking faults. Impurities are marked by the following symbols: * for remaining $Li_3Ni_2BiO_6$ and # for bismutite $Bi_2O_2(CO_3)$.

$Ag_3Ni_2BiO_6$ is, to the best of our knowledge, the first reported delafossite which contains a Bi^{5+} cation. Its structure is shown in Figure 6.11. As the stacking nature of $Li_3Ni_2BiO_6$ is O3 (O3S regarding the honeycomb ordering), $Ag_3Ni_2BiO_6$ structure is the D3 delafossite polytype (or D3S). A slab-gliding process is necessary during the topotactic ionic exchange in order to create the linear dumbbell site that silver cations can accommodate.[23] The diffuse and asymmetric peak (also present in the case of $Ag_3Co_2SbO_6$[3]) is obviously related to stacking defects. It seems to be more visible than in $Li_3Ni_2BiO_6$, as supplementary faults may occur during the ionic

exchange and are added to the initial stacking faults of the precursor. These stacking faults prevent deeper structural characterization.

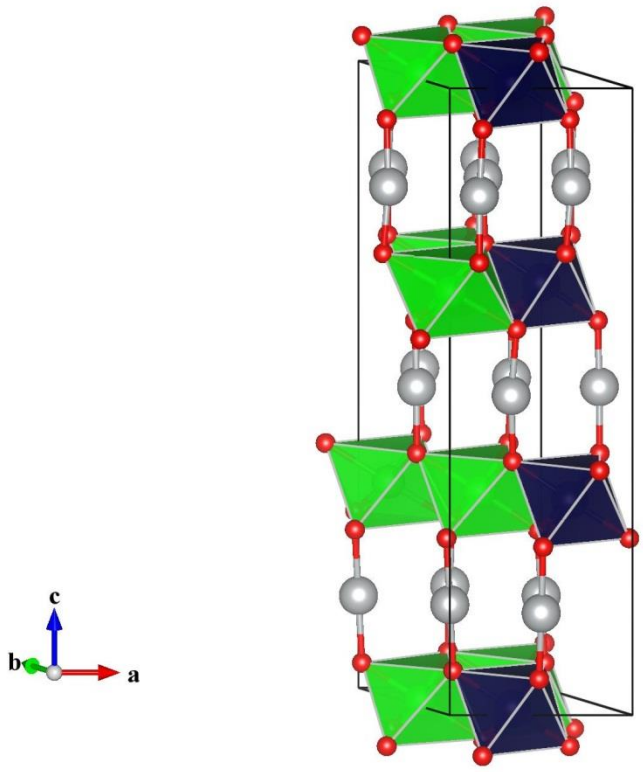

Figure 6.11 Representation in a perspective view of the $Ag_3Ni_2BiO_6$ delafossite structure. The honeycomb Ni^{2+}/Bi^{5+} ordering is evidenced within the $Ni_{2/3}Bi_{1/3}O_2$ slabs (green and dark blue edge-shared octahedra), while Ag cations (gray) occupy dumbbell linear sites.

Compounds obtained by ionic exchange are known to have a relatively weak thermal stability. TGA was the performed on $Ag_3Ni_2BiO_6$ to determine its stability and to compare it with that of similar compounds. Figure 6.12 shows the mass evolution until 800°C. The unique and significant mass loss just about 400°C stands for the decomposition of the delafossite compound. This value is very close to the decomposition temperature of $AgNiO_2$.[19] The post-TGA products were

determined by XRD to be nickel and bismuth oxides as well as silver metal. Therefore, the mass loss is attributed to oxygen departure according to equation 2 and its experimental value of 5.4%:

$Ag_3Ni_2BiO_6 \rightarrow ½\ Bi_2O_3 + 2\ NiO + 3\ Ag + 5/4\ O_2$ (2)

perfectly matches with a theoretical loss of 5.36%. As there is only one mass loss, the reductions of silver and bismuth occur in the same temperature range. Note that this TGA analysis neglected the minor aforementioned impurities present in the final product.

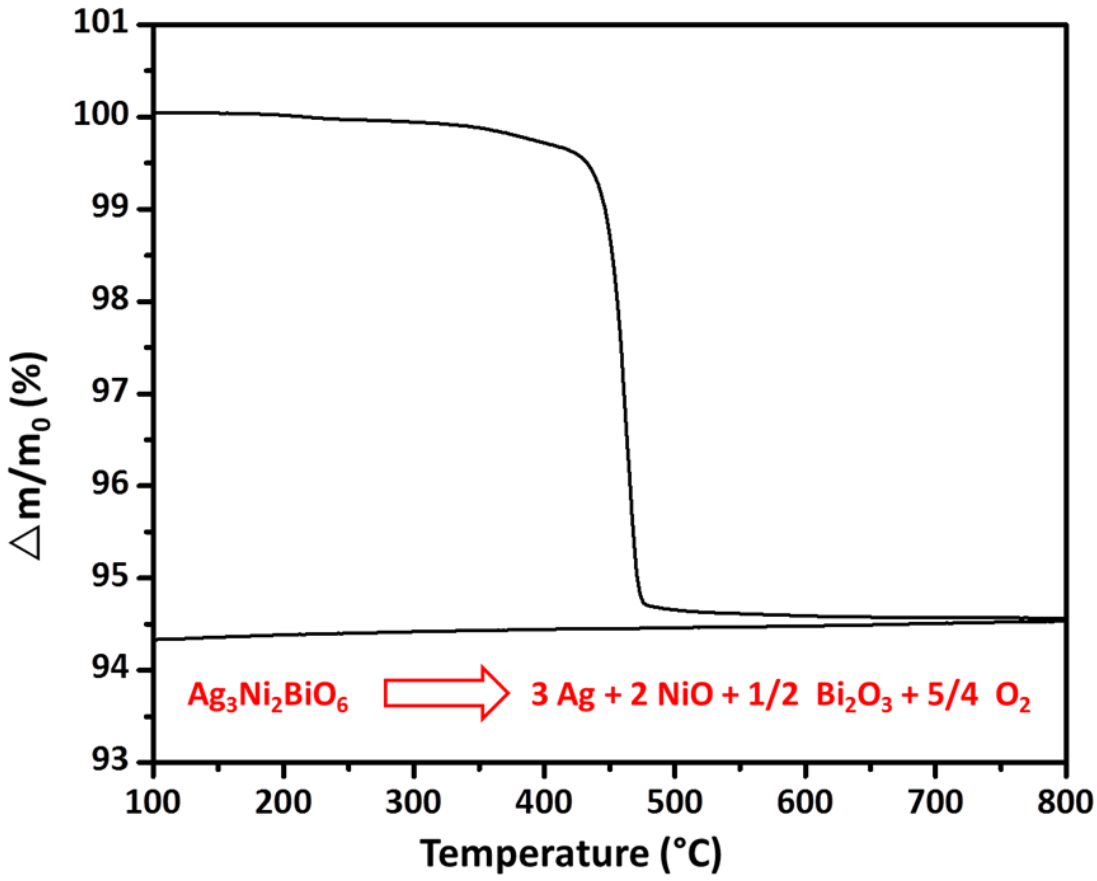

Figure 6.12 Thermogravimetric analysis evidencing the weak stability of the delafossite $Ag_3Ni_2BiO_6$ formed by ionic exchange.

6.3 Conclusions

The new layered compound $Li_3Ni_2BiO_6$ was prepared by a conventional solid state reaction. Its lamellar structure is analogous to that of several other $A_3M_2XO_6$ compounds and is characterized by a honeycomb ordering between Ni^{2+} and Bi^{5+} cations within the slabs. $Li_3Ni_2BiO_6$ crystallizes in a monoclinic cell (space group *C*2/*m*) with the parameters *a* = 5.2581(4) Å, *b* = 9.116(1) Å, *c* = 5.1969(8) Å, and β = 109.33(1)°. However, some stacking faluts are present and weakly alter some specific diffraction peaks. A DIFFaX simulation enables us to estimate a stacking defect concentration of approximately 5%. $Li_3Ni_2BiO_6$ presents a paramagnetic behavior at high temperature and an antiferromagnetic transition at 5.5 K. As with the $Li_3Ni_2SbO_6$ analogue, the electrochemical deintercalation and intercalation of lithium ions is possible; however, the batter capacity is rather limited, certainly due to Li/Ni mixing occurring durind the electrochemical cycling.

Three other phases have been successfully prepared by substitution half of the Ni^{2+} cations by Mg^{2+}, Cu^{2+} and Zn^{2+}. They are isostructural with $Li_3Ni_2BiO_6$ and present a paramagnetic behavior with, however, no evidence of antiferromagnetic transitions down to 3 K.

By topotactic molten salt ion exchange, the new delafossite phase $Ag_3Ni_2BiO_6$ was obtained from $Li_3Ni_2BiO_6$. It crystallized in hexagonal symmetry with the cell parameters *a* = 5.4012(8) Å and *c* = 18.795(4) Å, and it is still characterized by the

Ni^{2+}/Bi^{5+} honeycomb ordering. As for other delafossites obtained by ion exchange, $Ag_3Ni_2BiO_6$ has limited thermal stability, as it decomposes above 400°C.

6.4 Experimental Materials and Methods

Polycrystalline samples were prepared by conventional solid-state reactions. Lithium carbonate (Li_2CO_3, Aldrich 99.6%), nickel oxide (NiO, Alfa Aesar 99.998%) and bismuth oxide (Bi_2O_3, Aldrich 99.99%) were thoroughly ground together in an agate mortar in stoichiometric proportions to obtain $Li_3Ni_2BiO_6$. In order to avoid any moisture contamination, lithium carbonate was dried overnight at ~120°C before weighing. The pale green nominal mixture was then pelletized and heated in a gold crucible in air or O_2 flow over 12-48 hours (with intermediate grinding) in the temperature range 550° - 900°C with a heating rate of +2°C min^{-1}. At the end of the thermal treatment, the furnace was switched off and the samples remained in the furnace during the cool down. Other compositions $Li_3NiM'BiO_6$ (with M' = Mg, Cu, Zn) were prepared under the same thermal conditions by mixing magnesium oxide (MgO, Alfa Aesar 99.95%), copper oxide (CuO, Aldrich 99.95%) or zinc oxide (ZnO, Aldrich 99.9%) with the previous precursors in stoichiometric proportions.

Ion exchange was performed by mixing the obtained product $Li_3Ni_2BiO_6$ with silver nitrate ($AgNO_3$, Alfa Aesar 99.9%) in a large excess (ratio $Ag^+/Li^+ \approx 5$). The mixture was placed in a porcelain crucible and heated overnight at 230° - 250°C to ensure the melting of the nitrate. The resulting product was then thoroughly

washed with hot distilled water with magnetic stirring to dissolve the remaining nitrates and the filtered and finally dried overnight in an oven at ~50°C.[24]

The chemical compositions of the samples were determined by ICP-AES on a Varian 720 ES instrument. Powder samples (~10 mg) were dissolved in a high-quality hydrochloric acid solution heated at 70 °C with constant stirring.[24,25] These measurements were performed by Laetitia Etienne at the CNRS, ICMCB – Bordeaux.

The powder samples were characterized by X-ray diffraction (XRD) using a Rigaku Miniflex II diffractometer with Cu Kα radiation selected by a graphite monochromator on the diffracted beam. Powder samples were loaded onto an oriented Si single crystal "zero background" samples holder (MTI Corp.) to maximize he possibility of detecting minor impurity phases. Measurements were collected from 5° to 120° 2θ (step of 0.02°) with a 2 s fixed time.

Magnetism measurements were carried out on a Quantum Design physical properties measurement system (PPMS) in the temperature range 5 – 300 K under a magnetic field of 1 T and zero-field cooled conditions. A second run was slowly performed from 3 to 20 K to clarify the very low temperature behavior.

Electrochemical studies were carried out with Li_{metal}/liquid electrolyte/$Li_3Ni_2BiO_6$ cells. Merck Chemicals LP30 was used as the liquid electrolyte (1 M $LiPF_6$ in ethylene carbonate/diethyl carbonate 1/1). The positive electrode consisted of a mixture of 88 wt% of the active material (i.e., $Li_3Ni_2BiO_6$), 2 wt% of polytetrafluoroethylene, and 10 wt% of graphite/carbon black mix (1/1) to improve

the general conductivity. Lithium sheet was used as the negative electrode. The cells were assembled in an argon-filled glovebox. The batteries were relaxed one night before operating in galvanostatic mode at a C/20 rate (i.e., 20 h is required to remove 3 electrons/mol of $Li_3Ni_2BiO_6$). After cycling, the positive electrode was washed with dimethyl carbonate in order to perform XRD. This experiment was carried out by collaborators at the CNRS, Université de Bordeaux, ICMCB.

The thermal stability of $Ag_3Ni_2BiO_6$ was determined by TGA using a Mettler Toledo TGA 850 instrument. Sample powders were heated to 800°C in air for 2 h (heating and cooling set to respectively +5 and -5° min^{-1}) and XRD was performed on the final product to identify the remaining phases.

Scanning electron microscopy (SEM) analysis was performed with a FEI Quanta 600F microscope. Sample powders were spread onto a conductive carbon tape that was metalized with Au/Pd sputtering to avoid charging.

6.5 Acknowledgements

Portions of this chapter are directly used (text and figures) from the publication:

Berthelot, R., Schmidt, W., Muir, S., Eilertsen, J., Etienne, L., Sleight, A.W., Subramanian, M.A., 2012. New Layered Compounds with Honeycomb Ordering: $Li_3Ni_2BiO_6$, $Li_3NiM'BiO_6$ (M' = Mg, Cu, Zn), and the Delafossite $Ag_3Ni_2BiO_6$. Inorganic Chemistry 51, 5377–5385.

This work was supported by NSF Grant DMR 0804167.

6.6 References

[1] C. Greaves, S.M.A. Katib, Mater. Res. Bull. 25 (1990) 1175.
[2] E.A. Zvereva, M.A. Evstigneeva, V.B. Nalbandyan, O.A. Savelieva, S.A. Ibragimov, O.S. Volkova, L.I. Medvedeva, A.N. Vasiliev, R. Klingeler, B. Buechner, Dalton Trans. 41 (2012) 572.
[3] V.V. Politaev, V.B. Nalbandyan, A.A. Petrenko, I.L. Shukaev, V.A. Volotchaev, B.S. Medvedev, J. Solid State Chem. 183 (2010) 684.
[4] J. Bréger, M. Jiang, N. Dupré, Y.S. Meng, Y. Shao-Horn, G. Ceder, C.P. Grey, J. Solid State Chem. 178 (2005) 2575.
[5] A. Boulineau, L. Croguennec, C. Delmas, F. Weill, Solid State Ion. 180 (2010) 1652.
[6] R.D. Shannon, Acta Crystallogr. Sect. A 32 (1976) 751.
[7] M.M.J. Treacy, J.M. Newsam, M.W. Deem, Proc. R. Soc. Lond. Ser. Math. Phys. Sci. 433 (1991) 499.
[8] L. Viciu, Q. Huang, E. Morosan, H.W. Zandbergen, N.I. Greenbaum, T. McQueen, R.J. Cava, J. Solid State Chem. 180 (2007) 1060.
[9] M.A. Evstigneeva, V.B. Nalbandyan, A.A. Petrenko, B.S. Medvedev, A.A. Kataev, Chem. Mater. 23 (2011) 1174.
[10] J.B. Goodenough, Magnetism and the Chemical Bond, John Wiley & Sons: Interscience Publishers, New York-London, 1963.
[11] N.W. Ashcroft, N.D. Mermin, Solid State Physics, Brooks/Cole, Belmont, CA, 1976.
[12] P.A. Cox, The Electronic Structure and Chemistry of Solids, Oxford Science Publications, Oxford, U. K., 1987.
[13] C. Kittel, Introduction to Solid State Physics, 8th ed., Wiley, Hoboken, NJ, 2005.
[14] J.H. Van Vleck, The Theory of Electric and Magnetic Susceptibilities, Oxford University Press, Oxford,, 1952.
[15] R. Kubo, T. Nagamiya, Solid State Physics, McGraw-Hill, New York, 1969.
[16] X. Ma, K. Kang, G. Ceder, Y.S. Meng, J. Power Sources 173 (2007) 550.
[17] R. Berthelot, M. Pollet, D. Carlier, C. Delmas, Inorg. Chem. 50 (2011) 2420.
[18] P.N. Bityutskii, V.I. Khitrova, J. Struct. Chem. 9 (1969) 921.
[19] A. Wichainchai, P. Dordor, J.P. Doumerc, E. Marquestaut, M. Pouchard, P. Hagenmuller, A. Ammar, J. Solid State Chem. 74 (1988) 126.
[20] Y.J. Shin, J.P. Doumerc, P. Dordor, C. Delmas, M. Pouchard, P. Hagenmuller, J. Solid State Chem. 107 (1993) 303.
[21] T. Sörgel, M. Jansen, Z. Für Anorg. Allg. Chem. 631 (2005) 2970.
[22] R. Berthelot, M. Pollet, J.-P. Doumerc, C. Delmas, Inorg. Chem. 50 (2011) 6649.
[23] R. Berthelot, M. Pollet, J.-P. Doumerc, C. Delmas, Inorg. Chem. 50 (2011) 4529.

[24] R. Berthelot, W. Schmidt, S. Muir, J. Eilertsen, L. Etienne, A.W. Sleight, M.A. Subramanian, Inorg. Chem. 51 (2012) 5377.
[25] W. Schmidt, R. Berthelot, L. Etienne, A. Wattiaux, M.A. Subramanian, Mater. Res. Bull. 50 (2014) 292.

Chapter 7
Study of Solid Solutions Between the Layered Honeycomb-Ordered Phases $Na_2M_2TeO_6$ (M = Co, Ni, Zn)

7.1 Introduction

The family of P2-$Na_2M_2TeO_6$ (M = Co, Ni, Zn) has been discussed previously; however, the solid solutions between these compounds was interesting because of a structural transition that occurs due to the different stacking sequences. All compounds crystallize in a hexagonal unit cell however, a different stacking sequence is observed for the nickel (space group $P6_3/mcm$) containing composition compared to the zinc and cobalt compositions (space group $P6_322$) causing a structural transition to occur when nickel is substituted by zinc or cobalt which was monitored using X-ray diffraction. Magnetic susceptibility indicates high temperature paramagnetic behavior in all compositions with low temperature antiferromagnetic transitions in the compounds containing nickel or cobalt. This transition is suppressed upon zinc substitution. An interesting color transition from pink to light green to white was observed for M = Co, Ni, Zn, respectively, and was examined using diffuse reflectance spectroscopy.

7.2 Structural Analysis

Evstigneeva et al. used a conventional solid reaction process with a mixture of $NaNO_3/Na_2CO_3$ for the sodium precursor and MO and TeO_2 oxides. Their thermal treatments were performed in air at around 800 – 820°C during few hours. They

reported a pure phase for M = Ni, Zn; however, some impurities were noticed for M = Co, Mg.[1] In parallel, Viciu et al. obtained a pure $Na_2Co_2TeO_6$ phase by using a long time treatment (8 days in total) under nitrogen atmosphere.[2] As our initial attempts in reproducing the latter synthesis protocol were unsuccessful, an air atmosphere was selected for all the investigated compounds.

Figure 7.1 shows the XRD powder patterns obtained from nominal compositions $Na_2M_2TeO_6$ (M = Ni, Co, Zn) after a heat treatment of 24 h at 900°C under air, with an intermediate grinding as mentioned in the Experimental section. All the products are phase pure and diffraction peaks can be indexed in the corresponding space groups with refined cell parameters in agreement with the literature: $P6_3/mcm$ for $Na_2Ni_2TeO_6$ (with a = 5.2004(6) Å and c = 11.139(2) Å) and $P6_322$ for both $Na_2Zn_2TeO_6$ and $Na_2Co_2TeO_6$ (with a = 5.2783(6) Å and c = 11.256(2) Å and a = 5.2726(6) Å and c = 11.230(2) Å, respectively). The difference in the stacking sequence of the octahedral layers between these two structure types can be seen in Figure 7.2 and was discussed in Chapter 3.3. When comparing the XRD patterns in the 15 – 36° 2θ region (insets of FIG 7.1), the difference in the superstructure peak intensities is clear: $Na_2Co_2TeO_6$ and $Na_2Zn_2TeO_6$ are characterized by visible *l*-odd-indexed peaks (101 and 103) and weak *l*-even-indexed peaks (100 and 102), whereas only the latter ones are intense in the $Na_2Ni_2TeO_6$ pattern, as reported in the literature.[1] $Na_2Ni_2TeO_6$ is a light green product, whereas $Na_2Co_2TeO_6$ is pink and $Na_2Zn_2TeO_6$ is white. Our next step was the investigation of intermediate compositions $Na_2M_{2-x}M'_xTeO_6$ (M, M' = Ni, Zn, Co).

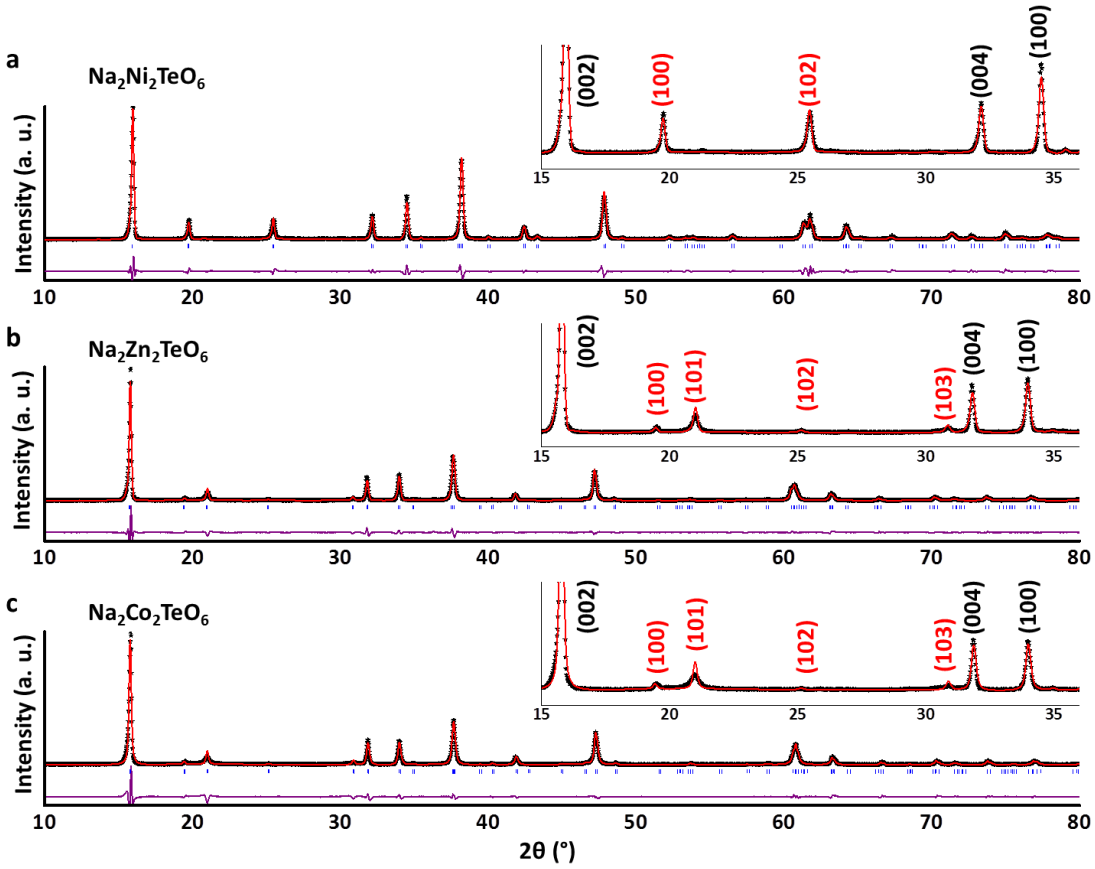

Figure 7.1 Experimental XRD patterns of the end members of a) $Na_2Ni_2TeO_6$, b) $Na_2Zn_2TeO_6$ and c) $Na_2Co_2TeO_6$. Observed, calculated (full profile matching with pseudo-Voigt function) and difference profiles are, respectively, in black stars, red line and purple line. Bragg positions are in green vertical lines. The insets from 15° to 36° 2θ highlight the differences in the superstructure peak intensities (red index).

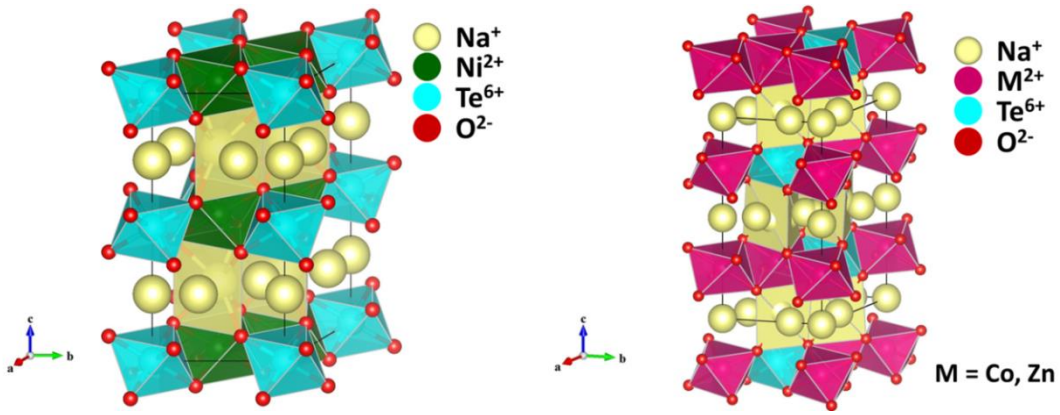

Figure 7.2 Structures of $Na_2Ni_2TeO_6$ space group *P*6_3/*mcm* (left) and $Na_2M_2TeO_6$ space group $P6_322$ (right). In the nickel composition, the octahedral layers are stacked to form columns of tellurium and nickel octahedra along the *c* direction. In the other compositions, the layers are stacked to have alternating columns of the M^{2+} and tellurium and columns of only M^{2+} along the *c* direction.

Figure 7.3 and 7.4 shows the XRD patterns obtained for the nominal compositions $Na_2Ni_{2-x}Zn_xTeO_6$ and $Na_2Ni_{2-x}Co_xTeO_6$. For each composition, the diffraction peaks can be indexed in an enlarged hexagonal cell characteristic of layered compounds with honeycomb ordering. All the compositions are single-phase; two complete solid solutions are therefore evidenced. As nickel is substituted by either zinc or cobalt, the diffraction peak positions slightly shift to low 2θ angles indicating a global increase of the cell parameters. The structural transition between $Na_2Ni_2TeO_6$ and both $Na_2Zn_2TeO_6$ and $Na_2Co_2TeO_6$ is clearly highlighted by the evolution of the superstructure diffraction peak intensities in the 18-36° 2θ region, with especially the drastic decrease of the (102) for a weak amount of substitution (after x = 0.15 and x = 0.2, respectively). The (101) peak intensity then progressively increases to become higher than the (100) when more than half nickel has been replaced ($x \geq 1$). After this limit, the structure of

$Na_2Zn_2TeO_6$ and $Na_2Co_2TeO_6$ (space group $P6_322$) is clearly adopted, Figure 7.4. Note that no extra superstructure diffraction peaks related to potential Ni/Zn or Ni/Co ordering within the honeycomb network was detected.

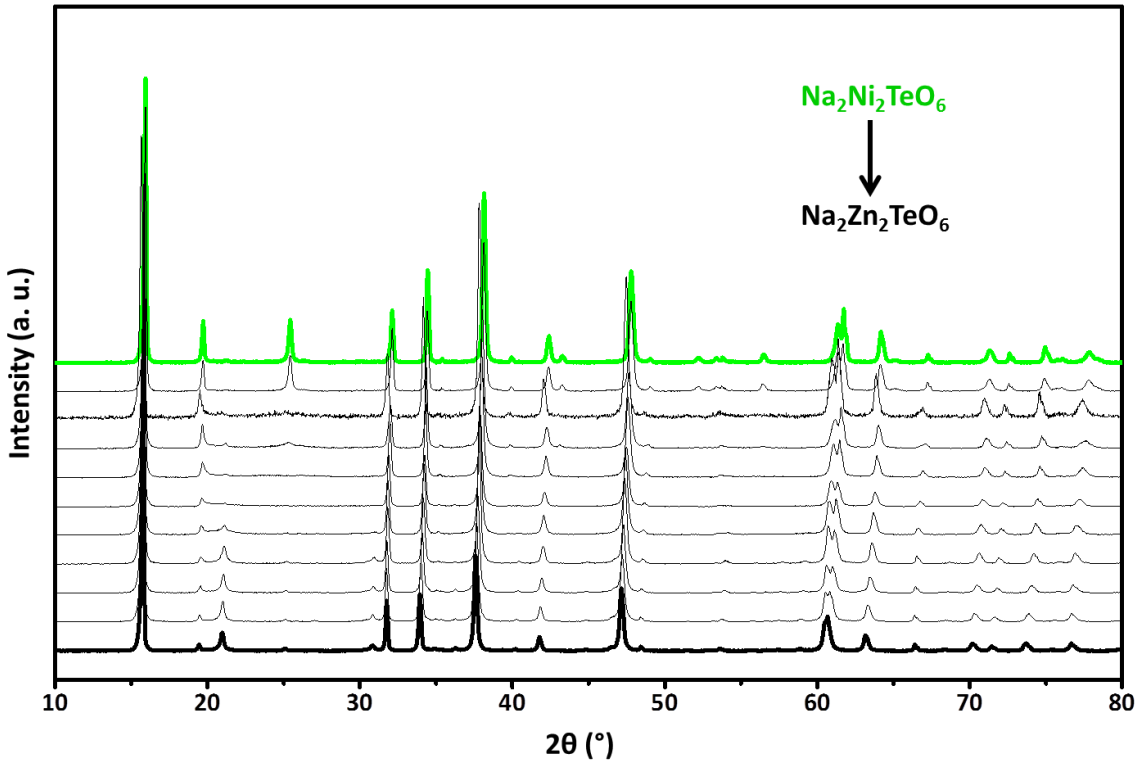

Figure 7.3 The XRD patterns obtained for the $Na_2Ni_{2-x}Zn_xTeO_6$ compositions show a complete solid solution with a structural transition from $Na_2Ni_2TeO_6$ (bold green line, space group *P*6_3/*mcm*) to $Na_2Zn_2TeO_6$ (bold black line, space group *P*$6_3$22). XRD patterns are normalized by the intensity of the main peak (002). The zinc content represented in the figure is *x* = 0, 0.15, 0.2, 0.25, 0.5, 0.75, 1, 1.25, 1.5, 1.75, 2.

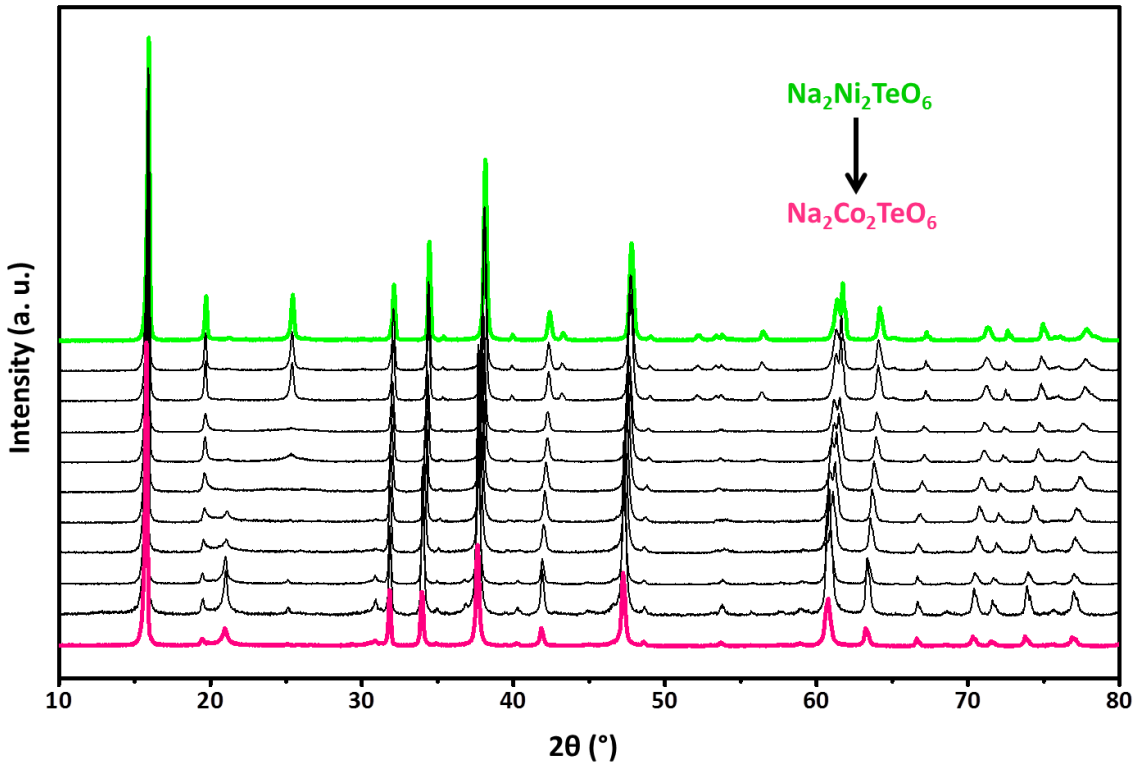

Figure 7.4 The XRD patterns obtained for the $Na_2Ni_{2-x}Co_xTeO_6$ compositions show a complete solid solution with a structural transition from $Na_2Ni_2TeO_6$ (bold green line, space group *P*6$_3$/*mcm*) to $Na_2Co_2TeO_6$ (bold pink line, space group *P*6$_3$22). XRD patterns are normalized by the intensity of the main peak (002). The cobalt content represented in the figure is *x* = 0, 0.15, 0.2, 0.25, 0.5, 0.75, 1, 1.25, 1.5, 1.75, 2.

The hexagonal cell parameter evolutions, obtained through profile matching refinement using a pseudo-Voigt function, are shown at the same scale in FIGURE 7.5. Both *a* and *c* parameters progressively increase as nickel is replaced by zinc or cobalt, which was expected regarding the difference in ionic radii ($^{VI}Ni^{2+}$ = 0.69 Å, $^{VI}Zn^{2+}$ = 0.74 Å, $^{VI}{}_{HS}Co^{2+}$ = 0.745 Å)[3] and therefore the cell parameters of the three end members. In both these solid solutions, the cell parameter evolution is regular and no peculiar anomaly that would be related to the structural transition is observed.

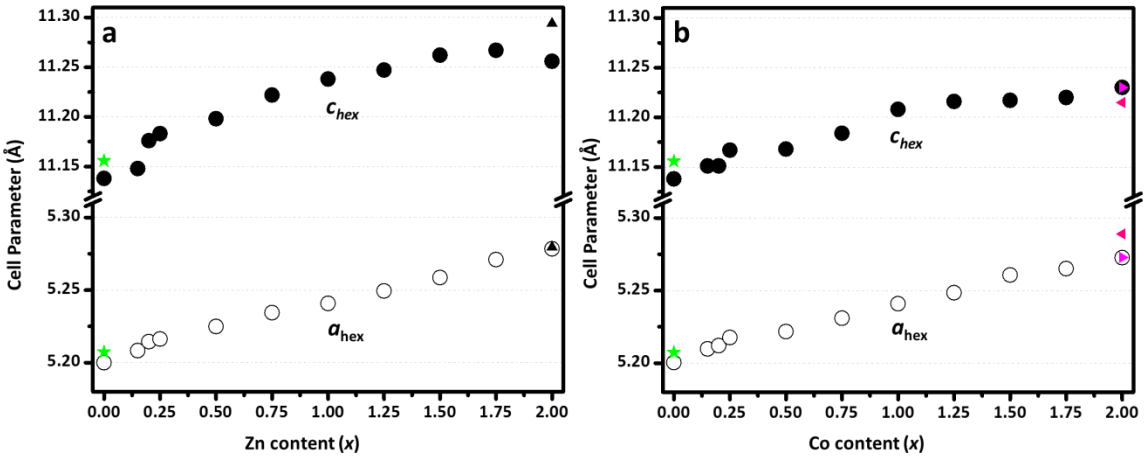

Figure 7.5 Cell parameter evolution for the solid solutions a) $Na_2Ni_{2-x}Zn_xTeO_6$ and b) $Na_2Ni_{2-x}Co_xTeO_6$. The green filled stars correspond to the literature values for $Na_2Ni_2TeO_6$[1] and the pink filled left caret[2] and magenta filled right caret[1] are the literature values for $Na_2Co_2TeO_6$. The error bars for this data are smaller than the symbol size.

Figure 7.6 shows the XRD patterns obtained for the nominal composition $Na_2Co_{2-x}Zn_xTeO_6$. Here also, all the compositions are single-phase. However, there is no structural transition as diffractions peaks can be clearly indexed with the same space group ($P6_322$) for the whole range of composition, as it was expected regarding the structure of the two end members. No extra superstructure diffraction peaks related to a potential Co/Zn ordering within the honeycomb network were noticed for any investigated compositions. The evolution of the hexagonal cell parameters refined by profile matching is shown in FIGUER 7.6 at the same scale as in FIGURES 7.5. In agreement with the similar ionic radii for Zn^{2+} and Co^{2+}, both of the cell parameter evolutions are very weak along the solid solution. The *a* parameter value remain fairly constant, whereas a tiny increase of the *c* parameter is observed.

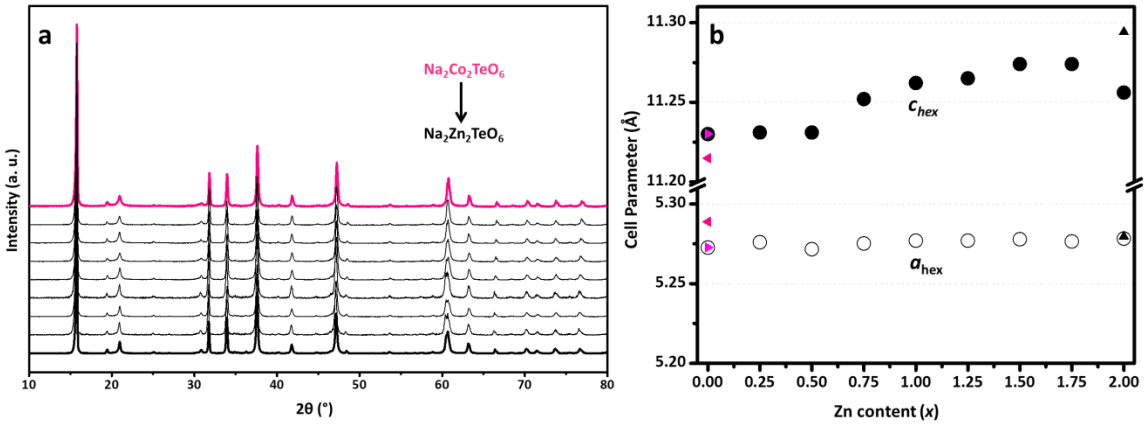

Figure 7.6 The XRD patterns obtained for the $Na_2Co_{2-x}Zn_xTeO_6$ solid solution (a) show a complete solid solution without any structural transition as both $Na_2Co_2TeO_6$ (bold pink line) and $Na_2Zn_2TeO_6$ (bold black line) crystallize in the space group $P6_322$. The variation of the cell parameters (b) a_{hex} and c_{hex} is very weak compared to the other solid solutions. The XRD patterns are normalized by the intensity of the main peak (002). Error bars for the cell parameters are smaller than the symbols. For the cell parameters (b), the left pink filled carets[2] and right magenta filled carets[1] are the literature values for $Na_2Co_2TeO_6$. The top pointing black filled carets are the literature values for $Na_2Zn_2TeO_6$.[1] The zinc content x is shown for $0 \leq x \leq 2$ at every 0.25 interval.

7.3 Magnetism

As both Ni^{2+} ($3d^8$) and Co^{2+} ($3d^7$) possess unpaired electrons, it is therefore interesting to study the magnetic susceptibility dependence with temperature of the end members $Na_2Ni_2TeO_6$ and $Na_2Co_2TeO_6$. The magnetic behavior of the latter phase has been reported[2]; however, to the best of our knowledge, the magnetic properties of $Na_2Ni_2TeO_6$ were not reported in the literature.

Figures 7.7, 7.8 and 7.9 show the temperature dependent magnetic susceptibility for polycrystalline samples of the solid solutions $Na_2Ni_{2-x}Zn_xTeO_6$, $Na_2Co_{2-x}Zn_xTeO_6$ and $Na_2Ni_{2-x}Co_xTeO_6$. All the compositions exhibit a general paramagnetic behavior at high temperature as the inverse of the magnetic

susceptibility follows a linear trend (insets of Figures 7.7 to 7.9). The linear domain is longer for $Na_2Ni_{2-x}Zn_xTeO_6$ than for the solid solutions containing cobalt. Therefore, Curie-Weiss law fittings were performed from 100 to 300 K for $Na_2Ni_{2-x}Zn_xTeO_6$ and from 150-200 to 300 K for both $Na_2Co_{2-x}Zn_xTeO_6$ and $Na_2Ni_{2-x}Co_xTeO_6$. Curie-Weiss law fittings were performed by the addition of an additional temperature-independent term χ_0 to take into account the diamagnetic contribution: $\chi = C/(T - \theta) + \chi_0$. Corresponding magnetic data are provided in Tables 7.1 to 7.3. Similar fittings were reported in the literature for $Na_2Co_2TeO_6$ and $Na_3Co_2SbO_6$.[2]

For pure $Na_2Ni_2TeO_6$, the total effective magnetic moment μ_{eff} is 3.48 μ_B per nickel which is in fairly good agreement with the theoretical value assuming the magnetism results from Ni^{2+} cations with spin-only contributions ($3d^8$, S = 1 and $\mu_{theor} = 2.83\ \mu_B/Ni^{2+}$). The slightly higher experimental value of the effective moment can be explained by the spin-orbital coupling which will increase the observed moment in the case of elements with more than half-filled *d* orbitals. Indeed an experimental value of 3.2 μ_B is often found in the literature.[4–7] A similar experimental value was also recently found in the analogue phase $Li_3Ni_2BiO_6$.[8] As nickel is progressively replaced by the non-magnetic zinc in the $Na_2Ni_{2-x}Zn_xTeO_6$ solid solution, the magnetic susceptibility value is logically lower. The value of the effective moment per nickel slightly decreases but remains higher than the theoretical value with spin-only contributions (Table 7.1).

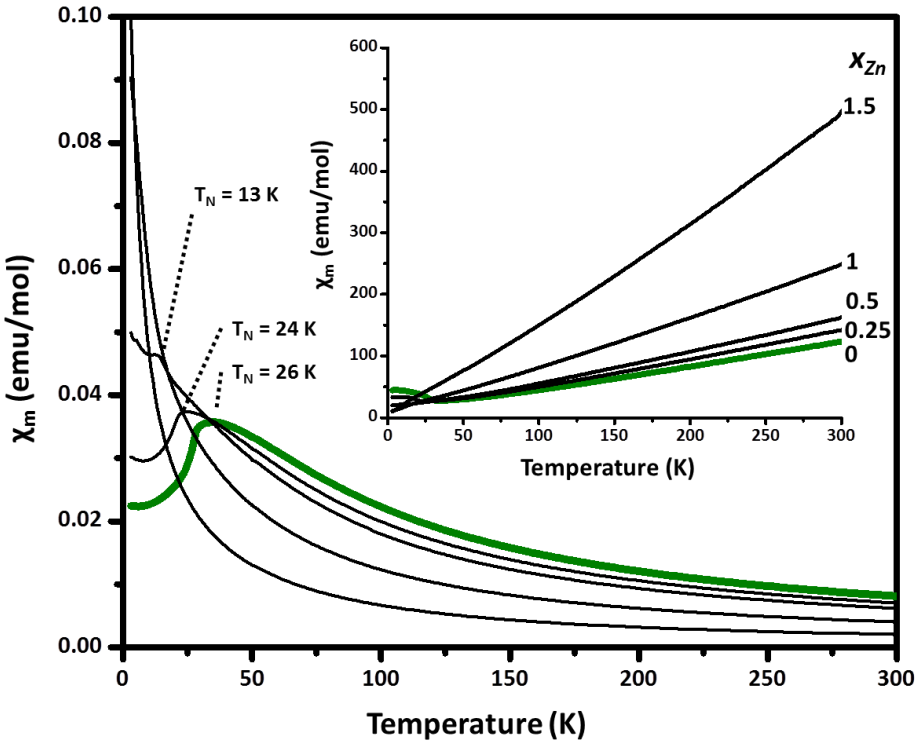

Figure 7.7 The magnetic susceptibility evolutions of different $Na_2Ni_{2-x}Zn_xTeO_6$ polycrystalline samples show a decrease of the magentic signal with zinc substitution. The low-temperature antiferromagnetic transition of $Na_2Ni_2TeO_6$ (bold green line) also progressively weakens. The paramagnetic behavior at high temperature is evidenced for all the compositions by the linear evolution of the inverse susceptibility fitted from 100 to 300 K by a Curie-Weiss law (inset). Corresponding magnetic data are presented in Table 1.

Table 7.1 Magentic data (effective moment μ_{eff}, Weiss constant θ and diamagneitc contribution χ_0) obtained through the solid solution $Na_2Ni_{2-x}Zn_xTeO_6$ with Curie-Weiss fitting. The theoretical moment is $\mu_{theor.}$ = 2.83 μ_B/Ni^{2+} assuming spin-only contributions (Ni^{2+}: 3d^8, S = 1).

Zn content (*x*)	$\mu_{eff.}$ (μ_B/Ni^{2+})	θ (K)	χ_0 (emu/mol)
0	3.48	-28	1.1×10^{-3}
0.25	3.42	-22	-9.0×10^{-4}
0.5	3.42	-17	-7.3×10^{-4}
1	3.28	-7.6	-4.4×10^{-4}
1.5	3.37	-0.6	-3.2×10^{-4}
2	-	-	-

For pure $Na_2Co_2TeO_6$, the effective moment μ_{eff} is found to be 5.60 μ_B per cobalt, in very good agreement with what was previously reported (5.64 μ_B[2]) and

also with experimental values usually found in the literature for Co^{2+} in high-spin configuration (4.8 μ_B[4–7]). For the same reasons as Ni^{2+}, the experimental value is slightly higher than the theoretical value assuming spin-only contribution ($_{HS}Co^{2+}$ $3d^7$, S = 3/2, μ_{theor} = 3.87 μ_B/Co^{2+}). As for the solid solution $Na_2Co_{2-x}Zn_xTeO_6$ (Figure 7.8), the substitution of cobalt by the non-magnetic zinc involves a lower magnetic susceptibility; however, the value of the effective moment per cobalt is very stable (Table 7.2).

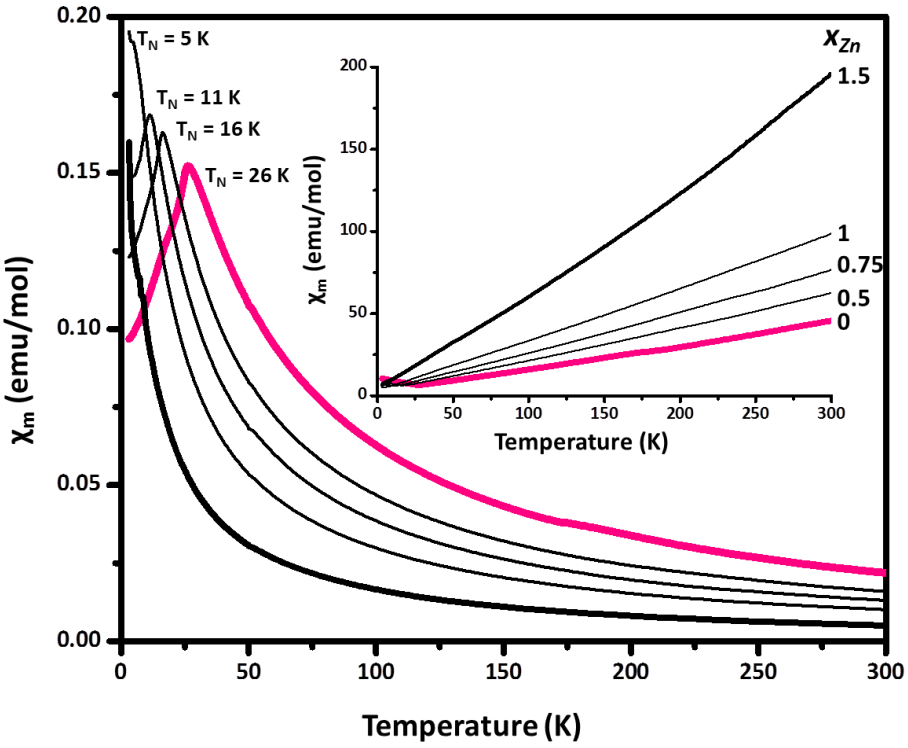

Figure 7.8 The magnetic susceptibility evolutions of different $Na_2Co_{2-x}Zn_xTeO_6$ polycrystalline samples show a decrease of the magnetic signal with zinc substitution. The low-temperature antiferromagnetic transition of $Na_2Co_2TeO_6$ (bold pink line) also progressively weakens. The paramagnetic behavior at high temperature is evidenced for all the compositions by the linear evolution of the inverse susceptibility fitted from 150 – 200 to 300 K by a Curie-Weiss law (inset). Corresponding magnetic data are presented in Table 2.

Table 7.2 Magnetic data (effective moment μ_{eff}, Weiss constant θ and diamagneitc contribution χ_0) obtained through the solid solution $Na_2Co_{2-x}Zn_xTeO_6$ with Curie-Weiss fitting. The theoretical moment is $\mu_{theor.}$ = 3.87 μ_B/Co^{2+} assuming spin-only contributions (Co_{HS}^{2+}: 3d^7, S = 3/2).

Zn content (*x*)	$\mu_{eff.}$ (μ_B/Co^{2+})	θ (K)	χ_0 (emu/mol)
0	5.60	-9.4	3.3×10^{-4}
0.5	5.45	-14	-1.5×10^{-3}
0.75	5.30	-10	-1.0×10^{-3}
1	5.31	-13	-1.1×10^{-3}
1.5	5.68	-12	-1.3×10^{-3}
2	-	-	-

At low temperature, both $Na_2Ni_2TeO_6$ and $Na_2Co_2TeO_6$ are characterized by a local maximum in the magnetic susceptibility (Néel temperatures are 34 and 26 K, respectively). Similar antiferromagnetic transitions were reported for the other Ni^{2+} honeycomb-ordered analogue phases, $Li_3Ni_2SbO_6$ and $Li_3Ni_2BiO_6$,[8,9] and by Viciu et al. for $Na_2Co_2TeO_6$.[2] Note that these authors also detected another weak transition around 17 K, possibly attributed to spin reorientation, which is also slightly visible in our experimental data. For both solid solutions the AFM transition progressively vanished (with a decrease of the Néel temperature) as nickel or cobalt is replaced by zinc (Figure 7.7 and 7.8). However, the AFM transition lasts longer in the $Na_2Co_{2-x}Zn_xTeO_6$ solid solution compared to $Na_2Ni_{2-x}Zn_xTeO_6$, up to x = 1 and x = 0.5, respectively. The case of $Na_2Ni_{2-x}Co_xTeO_6$ is different from the two above mentioned solid solutions as there is no end member without any magnetic contribution. The AFM transition reported for $Na_2Ni_2TeO_6$ and $Na_2Co_2TeO_6$ is still present for intermediate compositions, with an unchanged Néel temperature (Figure 7.9). The effective moment logically increases as nickel is replaced by cobalt,

and the value still fairly matches with spin-only contribution theoretical value (Table 7.3). For all compositions, the Weiss constant θ is negative in agreement with the predominance of AFM interactions (Tables 7.1 and 7.2). The Weiss constant evolution is however different from one solid solution to another. For $Na_2Ni_{2-x}Zn_xTeO_6$, it progressively increases up to close to zero with zinc substitution, whereas it remains stable for $Na_2Co_{2-x}Zn_xTeO_6$.

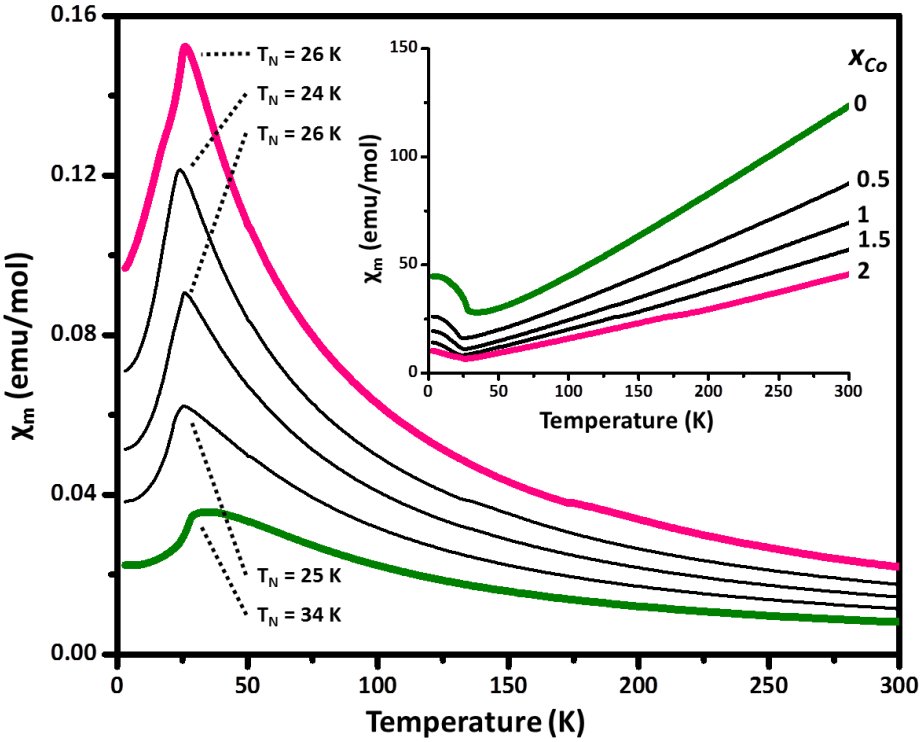

Figure 7.9 The magnetic susceptibility evolutions of polycrystalline samples of different $Na_2Ni_{2-x}Co_xTeO_6$ compositions show a decrease of the magnetic signal with cobalt substitution. However, the low-temperature antiferromagnetic transition of $Na_2Ni_2TeO_6$ (bold green line) and $Na_2Co_2TeO_6$ (bold pink line) remains present through the solid solution, with especially a stable Néel temperature. The paramagnetic behavior at high temperature is evidenced for all the compositions by the linear evolution of the inverse of the susceptibility fitter from 150 – 200 to 300 K by a Curie-Weiss law (inset). Corresponding magnetic data are presented in Table 3.

Table 7.3 Magnetic data (effective moment μ_{eff}, Weiss constant θ and diamagneitc contribution χ_0) obtained through the solid solution $Na_2Ni_{2-x}Co_xTeO_6$ with Curie-Weiss fitting. The theoretical moment $\mu_{theor.}$ assumes spin-only contributions from both Ni^{2+} and Co^{2+}.

Co content (*x*)	$\mu_{theor.}$ (μ_B)	$\mu_{eff.}$ (μ_B)	θ (K)	χ_0 (emu/mol)
0	4.00	4.92	-28	1.1×10^{-3}
0.5	4.67	5.83	-26	-1.5×10^{-3}
1	4.79	6.30	-13	-1.3×10^{-3}
1.5	5.97	6.65	-2.8	-5.7×10^{-4}
2	7.74	7.92	-9.4	3.3×10^{-4}

7.4 Optical Characterization

As it was previously mentioned, the three end members $Na_2Ni_2TeO_6$, $Na_2Co_2TeO_6$ and $Na_2Zn_2TeO_6$ exhibit different colors: light green, dark pink and white, respectively. The color of $Na_2Ni_2TeO_6$ is in agreement with what is observed for other layered phases containing Ni^{2+} cations, $Li_3Ni_2XO_6$ (X = Bi, Sb).[8,9] The pink color of $Na_2Co_2TeO_6$ was also reported by Evstigneeva et al., whereas Viciu et al. mentioned a similar light pastel hue that can be linked to a unique valence of the cobalt ions.[1,2] Figure 7.10d shows the color of different powder samples of the three investigated solid solutions and the corresponding diffuse reflectance spectra. For $Na_2Ni_{2-x}Zn_xTeO_6$, the color variation is very weak and goes from light green to white, with a tiny shifting of the absorption band. The solid solutions containing cobalt are more interesting as the color change is more important. $Na_2Co_2TeO_6$ reflectance spectrum is characterized by two distinct absorption bands (Figure 7.10a-b). The main one is centered around 300 nm (UV region) and the second on is centered around 500 nm (green region). In both $Na_2Ni_{2-x}Co_xTeO_6$ and Na_2Co_{2-}

$_x$Zn$_x$TeO$_6$, the dark pink color of $Na_2Co_2TeO_6$ progressively lightens with zinc or nickel substation, leading to interesting different nice light pink hues. The comparison of the reflectance spectra shows a displacement of the main absorption band to lower wavelength and a decrease (without any shifting) of the second band.

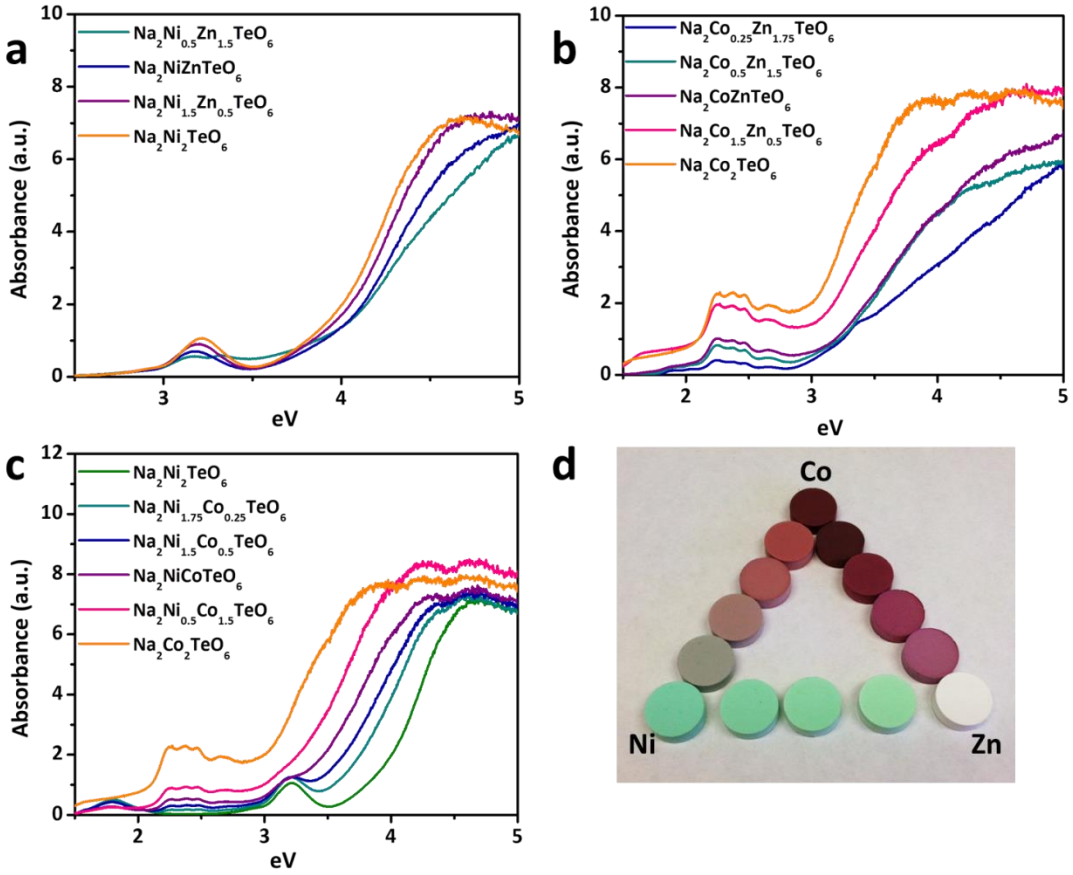

Figure 7.10 The diffuse reflectance spectra for the solid solutions are (a) $Na_2Ni_{2-x}Co_xTeO_6$, (b) $Na_2Co_{2-x}Zn_xTeO_6$ and (c) $Na_2Ni_{2-x}Zn_xTeO_6$. The composition of the pellets in (d) correspond to the compositions labeled in the spectra of (a), (b) and (c).

7.5 Conclusions

Three solid solutions between the layered honeycomb ordered $Na_2M_2TeO_6$ (M = Ni, Co, Zn) have been investigated through X-ray diffraction, magnetism and

optical measurements. Although no unexpected peculiar behavior was noticed, this study is interesting as it clearly shows how the cationic substitution influences several distinct features with different corresponding level of transitions. From a structural point of view, the substitution of nickel by zinc or cobalt involves a structural transition with very low amount of nickel replacement. From the magnetic point of view, the evolution of the effective moments matches well the cationic substitution for the three investigated solids solutions. However in the same time, a transition is observed between compositions characterized by an AFM ordering at low temperature and those which only present a paramagnetic behavior on the whole temperature range. Finally, the color variations do not present any drastic and unpredicted change as the color varies in a regular way according to the particular color of the three end members.

7.6 Experimental Materials and Methods

Polycrystalline samples with nominal compositions $Na_2Ni_{2-x}Zn_xTeO_6$, $Na_2Ni_{2-x}Co_xTeO_6$ and $Na_2Co_{2-x}Zn_xTeO_6$ ($0 \leq x \leq 2$) were prepared by conventional solid state reaction. Sodium carbonate (Na_2CO_3, Spectrum Chemical 99.5%), nickel oxide (NiO, Alfa Aesar 99.998%), cobalt oxide (Co_2O_3, Alfa Aesar 99.7%), zinc oxide (ZnO, Sigma Aldrich 99.9%) and tellurium oxide (TeO_2, Acros Organics 99+%) were thoroughly ground together in an agate mortar in stoichiometric proportions. In order to avoid any moisture contamination, sodium carbonate was dried overnight at ~120°C before weighing. Powder mixtures were then pelletized and heated in a gold

crucible in air for 24 h at 900°C with one intermediate grinding after 12 h. The heating rate was set to +2°C min^{-1} and at the end of each thermal treatment, the furnace was switched off and samples remained in the furnace during the cool down.

The powder samples were first characterized by X-ray diffraction (XRD) using a Rigaku Miniflex II diffractometer with Cu Kα radiation selected by a graphite monochromator on the diffracted beam. Powder samples were loaded onto an oriented Si single crystal "zero background" samples holder (MTI Corp.) to maximize he possibility of detecting minor impurity phases. Measurements were collected from 5° to 120° 2θ (step of 0.02°) with a 2 s fixed time.

Magnetism measurements were carried out on a Quantum Design physical property measurement system (PPMS) in the temperature range 3 – 300 K under a magnetic field of 1 T and zero field cooled conditions.

Diffuse reflectance measurements were carried out on packed powder samples with deuterium and halogen sources (200 – 1150 nm) passed through bifurcated fiber optic wire and magnesium oxide (MgO, Sigma Aldrich, 99.9%) as the white reference. The data was collected by the bifurcated optic cable and carried to an Ocean Optics HR4000 spectrophotometer. This setup is located in Oregon State University's Physics Department in Dr. David McIntyre's research group.[10]

7.7 Acknowledgements

Portions of this chapter are used from (text and adapted figures) the publication:

Berthelot, R., Schmidt, W., Sleight, A.W., Subramanian, M.A., 2012. Studies on solid solutions based on layered honeycomb-ordered phases P2-$Na_2M_2TeO_6$ (M=Co, Ni, Zn). Journal of Solid State Chemistry 196, 225–231.

This work has been supported by NSF grant DMR 0804167. The authors want to thank Geneva Laurita (Oregon State University, Chemistry Department) for technical assistance during the optical measurements.

7.8 References

[1] M.A. Evstigneeva, V.B. Nalbandyan, A.A. Petrenko, B.S. Medvedev, A.A. Kataev, Chem. Mater. 23 (2011) 1174.
[2] L. Viciu, Q. Huang, E. Morosan, H.W. Zandbergen, N.I. Greenbaum, T. McQueen, R.J. Cava, J. Solid State Chem. 180 (2007) 1060.
[3] R.D. Shannon, Acta Crystallogr. Sect. A 32 (1976) 751.
[4] J.B. Goodenough, Magnetism and the Chemical Bond, John Wiley & Sons: Interscience Publishers, New York-London, 1963.
[5] N.W. Ashcroft, N.D. Mermin, Solid State Physics, Brooks/Cole, Belmont, CA, 1976.
[6] P.A. Cox, The Electronic Structure and Chemistry of Solids, Oxford Science Publications, Oxford, U. K., 1987.
[7] C. Kittel, Introduction to Solid State Physics, 8th ed., Wiley, Hoboken, NJ, 2005.
[8] R. Berthelot, W. Schmidt, S. Muir, J. Eilertsen, L. Etienne, A.W. Sleight, M.A. Subramanian, Inorg. Chem. 51 (2012) 5377.
[9] E.A. Zvereva, M.A. Evstigneeva, V.B. Nalbandyan, O.A. Savelieva, S.A. Ibragimov, O.S. Volkova, L.I. Medvedeva, A.N. Vasiliev, R. Klingeler, B. Buechner, Dalton Trans. 41 (2012) 572.
[10] J.A. Russell, Measurement of Optical Bandgap Energies of Semiconductors, Master of Science in Physics, Oregon State University, 2011.

Chapter 8

General Conclusions and Future Work

It was realized through this work that new materials are available for discovery and characterization. New compositions in the family of layered oxides with honeycomb ordering were discovered and their properties were evaluated. Due to a high degree of stacking faults, the $Na_3LiFeSbO_6$ structure could not be determined by refinement of the XRD pattern. Other techniques such as ICP-AES and ^{57}Fe Mössbauer spectroscopy were used to aid in the verification of the composition and the coordination environment of the iron. Traditional methods of analysis may not be sufficient when investigating materials such as the $Na_3LiFeSbO_6$ composition in Chapter 5. While synthetic procedures failed to produce crystals or a defect free polycrystalline powder sample, characterization techniques are necessary to then understand the structure and properties of these types of materials. A discussion with Dr. Thomas Proffen, an expert in total scattering techniques, during a visit to Oak Ridge National Lab indicated that utilizing diffuse scattering to determine the local structure of a faulted material could be implemented to help solve the structure. Stacking faults are present as part of the average structure which X-ray diffraction and neutron diffraction measure. There are also programs such as DISCUS and DIFFaX which can be used to model stacking faults in a material and produce an experimental diffraction pattern that can be used qualitatively to determine the amount of stacking faults present in a compound.

A lesser degree of stacking faults was present in the other composition discovered in this work, $Li_3Ni_2BiO_6$. DIFFaX was implemented by Dr. Romain Berthelot in the work on $Li_3Ni_2BiO_6$ in Chapter 6, which indicated approximately 5% stacking faults were present in this compound. This was the second compound to be investigated involving bismuth in the honeycomb layer. The similarities of these layered compounds to current battery electrode materials led to the investigation of the electrochemical properties of this material as a cathode material. As with many of the more complex structures compared to $LiCoO_2$, this new compound has limited capacity. The Ni^{2+} was easily substituted with 50% of other 2+ metal cations, Cu, Mg, and Zn. Substitution by copper led to unexpected lattice parameters considering the similar size to that of Mg and Zn. It was determined that as usual with Cu^{2+} in an octahedral coordination, Jahn-Teller distortion occurs which affects the lattice parameters of this compound because of the orientation of the octahedra in these layers.

Solid solutions play a fundamental role in solid state chemistry and in this work two families of solid solutions were investigated, $Na_3M_{2-x}M'_xSbO_6$ (M, M' = Cu, Mg, Ni, Zn) and $Na_2M_{2-x}M'_xTeO_6$ (M, M' = Co, Ni, Zn). Although many of the parent compounds (i.e., $Na_3M_2SbO_6$ or $Na_2M_2TeO_6$) had been reported previously, this work on $Na_3Ni_{2-x}M'_xSbO_6$ first reported the magnetic susceptibility of the parent phase as well as that of the solid solutions. In the case for the tellurium phases, a smooth structure transition occurred between the nickel compound and the zinc and cobalt compounds. For both families of solid solutions, interesting color transitions

occurred which were the first report and discussion on the estimated band gap energies estimated using diffuse reflectance spectroscopy.

Layered materials in general are a very important class of solid state compounds that have a high impact on society already, specifically with their use in batteries. As the list of compounds grows, more fundamental insight will be available for preparing materials with desired properties. Synthesizing solid solutions of compounds also plays a key role in discovering new materials with exciting properties such as the blue pigment discovered in my research group the year before I joined. Although this field is driven by the search for new and efficient technologies, it is important to understand the fundamentals of the structure-property relationships of the materials being investigated.

Bibliography

A.M. Abakumov, A.A. Tsirlin, E.V. Antipov, in:, Editors-in-Chief: Jan Reedijk, Kenneth Poeppelmeier (Eds.), Comprehensive Inorganic Chemistry II (Second Edition), Elsevier, Amsterdam, 2013, pp. 1–40.
M. Armand, J.-M. Tarascon, Nature 451 (2008) 652.
N.W. Ashcroft, N.D. Mermin, Solid State Physics, Brooks/Cole, Belmont, CA, 1976.
M. Avdeev, V.B. Nalbandyan, I.L. Shukaev, in:, V.V. Kharton (Ed.), Solid State Electrochemistry I, Wiley-VCH Verlag GmbH & Co. KGaA, 2009, pp. 227–278.
R. Berthelot, D. Carlier, C. Delmas, Nat Mater 10 (2011) 74.
R. Berthelot, M. Pollet, D. Carlier, C. Delmas, Inorg. Chem. 50 (2011) 2420.
R. Berthelot, M. Pollet, J.-P. Doumerc, C. Delmas, Inorg. Chem. 50 (2011) 6649.
R. Berthelot, M. Pollet, J.-P. Doumerc, C. Delmas, Inorg. Chem. 50 (2011) 4529.
R. Berthelot, W. Schmidt, S. Muir, J. Eilertsen, L. Etienne, A.W. Sleight, M.A. Subramanian, Inorg. Chem. 51 (2012) 5377.
R. Berthelot, W. Schmidt, A.W. Sleight, M.A. Subramanian, Journal of Solid State Chemistry 196 (2012) 225.
T. Betz, Z. Anorg. Allg. Chem. 512 (1984) 19.
M. Bieringer, J.E. Greedan, G.M. Luke, Phys. Rev. B 62 (2000) 6521.
P.N. Bityutskii, V.I. Khitrova, J Struct Chem 9 (1969) 921.
A. Boulineau, L. Croguennec, C. Delmas, F. Weill, Solid State Ionics 180 (2010) 1652.
J.-J. Braconnier, C. Delmas, C. Fouassier, P. Hagenmuller, Materials Research Bulletin 15 (1980) 1797.
B. Brazel, R. Hoppe, Z. Naturforsch. B 38 (1983) 661.
J. Bréger, M. Jiang, N. Dupré, Y.S. Meng, Y. Shao-Horn, G. Ceder, C.P. Grey, Journal of Solid State Chemistry 178 (2005) 2575.
A.K. Cheetham, Day, Solid State Chemistry: Techniques, Clarendon Press, Oxford [etc.], 1988.
A.K. Cheetham, P. Day, Solid State Chemistry Compounds, Oxford University Press, New York, 1992.
S.K. Choi, R. Coldea, A.N. Kolmogorov, T. Lancaster, I.I. Mazin, S.J. Blundell, P.G. Radaelli, Y. Singh, P. Gegenwart, K.R. Choi, S.-W. Cheong, P.J. Baker, C. Stock, J. Taylor, Physical Review Letters 108 (2012).
E. Climent-Pascual, P. Norby, N.H. Andersen, P.W. Stephens, H.W. Zandbergen, J. Larsen, R.J. Cava, Inorg. Chem. 51 (2011) 557.
P.A. Cox, The Electronic Structure and Chemistry of Solids, Oxford Science Publications, Oxford, U. K., 1987.
B.D. Cullity, S.R. Stock, Elements of X-Ray Diffraction, Prentice Hall, Upper Saddle River, NJ, 2001.
J. Danon, L. May, An Introduction to Mössbauer Spectroscopy., Plenum Press, New York, 1971.
C. Delmas, C. Fouassier, P. Hagenmuller, Physica B+C 99 (1980) 81.

C. Delmas, J.-J. Braconnier, C. Fouassier, P. Hagenmuller, Solid State Ionics 3–4 (1981) 165.
S. Derakhshan, H.L. Cuthbert, J.E. Greedan, B. Rahaman, T. Saha-Dasgupta, Phys. Rev. B 76 (2007) 104403.
S. Derakhshan, J.E. Greedan, T. Katsumata, L.M.D. Cranswick, Chem. Mater. 20 (2008) 5714.
Y. Doi, K. Ninomiya, Y. Hinatsu, K. Ohoyama, J. Phys.: Condens. Matter 17 (2005) 4393.
J.F. Dorrian, R.E. Newnham, Materials Research Bulletin 4 (1969) 179.
M.D. Dyar, D.G. Agresti, M.W. Schaefer, C.A. Grant, E.C. Sklute, Annu. Rev. Earth Planet. Sci. 34 (2006) 83.
M.A. Evstigneeva, V.B. Nalbandyan, A.A. Petrenko, B.S. Medvedev, A.A. Kataev, Chem. Mater. 23 (2011) 1174.
S. Frenzen, Z. Naturforsch. 51 b (1996) 822.
GianniG46, Wikipedia, the Free Encyclopedia (n.d.).
J.B. Goodenough, Magnetism and the Chemical Bond, John Wiley & Sons: Interscience Publishers, New York-London, 1963.
C. Greaves, S.M.A. Katib, Mater. Res. Bull. 25 (1990) 1175.
A. Gupta, C. Buddie Mullins, J.B. Goodenough, Journal of Power Sources 243 (2013) 817.
J. Hesse, A. Rubartsch, J. Phys. E: Sci. Instrum. 7 (1974) 526.
J.L. Hodeau, M. Marezio, A. Santoro, R.S. Roth, Journal of Solid State Chemistry 45 (1982) 170.
F. Hulliger, Structural Chemistry of Layer-Type Phases, D. Reidel Publishing Company, Dordrecht, Holland, 1976.
J.P. Jakubovics, Magnetism and Magnetic Materials, Institute of Materials, London, 1994.
A.C.W.P. James, J.B. Goodenough, Journal of Solid State Chemistry 74 (1988) 287.
S. Juds, Photoelectric Sensors and Controls: Selection and Application, First Edition, CRC Press, 1988.
K. Kataoka, Y. Takahashi, N. Kijima, H. Nagai, J. Akimoto, Y. Idemoto, K. Ohshima, Materials Research Bulletin 44 (2009) 168.
H. Kawazoe, M. Yasukawa, H. Hyodo, M. Kurita, H. Yanagi, H. Hosono, Nature 389 (1997) 939.
C. Kittel, Introduction to Solid State Physics, 8th ed., Wiley, Hoboken, NJ, 2005.
H.-J. Koo, M.-H. Whangbo, Inorg. Chem. 47 (2007) 128.
G. Kortüm, Reflectance Spectroscopy Principles, Methods, Applications, Springer Berlin Heidelberg, Berlin, Heidelberg, 1969.
P. Kroeschell, R. Hoppe, Z. Anorg. Allg. Chem. 509 (1984) 127.
P. Kubelka, F. Munk,, Z. Tech. Phys. 12 (1931) 593.
R. Kubo, T. Nagamiya, Solid State Physics, McGraw-Hill, New York, 1969.
V. Kumar, N. Bhardwaj, N. Tomar, V. Thakral, S. Uma, Inorg. Chem. 51 (2012) 10471.
V. Kumar, A. Gupta, S. Uma, Dalton Trans. 42 (2013) 14992.

A.C. Larson, R.B. Von Dreele, Los Alamos National Laboratory Report LAUR 86-748 (1994).
M. Lee, L. Viciu, L. Li, Y. Wang, M.L. Foo, S. Watauchi, R.A. Pascal Jr, R.J. Cava, N.P. Ong, Nat Mater 5 (2006) 537.
M. Lee, L. Viciu, L. Li, Y. Wang, M.L. Foo, S. Watauchi, R.A. Pascal Jr., R.J. Cava, N.P. Ong, Physica B: Condensed Matter 403 (2008) 1564.
X. Ma, K. Kang, G. Ceder, Y.S. Meng, Journal of Power Sources 173 (2007) 550.
G.C. Mather, C. Dussarrat, J. Etourneau, A.R. West, J. Mater. Chem. 10 (2000) 2219.
G.C. Mather, R.I. Smith, J.M.S. Skakle, J.G. Fletcher, M.A. Castellanos R, M.P. Gutierrez, A.R. West, J. Mater. Chem. 5 (1995) 1177.
Y. Miura, R. Hirai, T. Fujita, Y. Kobayashi, M. Sato, J. Magn. Magn. Mater. 310 (2007) e389.
Y. Miura, R. Hirai, Y. Kobayashi, M. Sato, J. Phys. Soc. Jpn. 75 (2006) 084707.
K. Mizushima, P.C. Jones, P.J. Wiseman, J.B. Goodenough, Mater. Res. Bull. 15 (1980) 783.
L.R. Morss, E.H. Appelman, R.R. Gerz, D. Martin-Rovet, Journal of Alloys and Compounds 203 (1994) 289.
R. Nagarajan, S. Uma, M.K. Jayaraj, J. Tate, A.W. Sleight, Solid State Sci. 4 (2002) 787.
V.B. Nalbandyan, Russ. J. Inorg. Chem. 37 (1992) 1231.
V.B. Nalbandyan, M. Avdeev, M.A. Evstigneeva, J. Solid State Chem. 199 (2013) 62.
V.B. Nalbandyan, A.A. Petrenko, M.A. Evstigneeva, Solid State Ionics 233 (2013) 7.
M.J. O'Malley, H. Verweij, P.M. Woodward, Journal of Solid State Chemistry 181 (2008) 1803.
A.F. Orchard, Magnetochemistry, Oxford University Press, Oxford, 2003.
L. Pauling, J. Am. Chem. Soc. 51 (1929) 1010.
J.M. Paulsen, R.A. Donaberger, J.R. Dahn, Chemistry of Materials 12 (2000) 2257.
V.V. Politaev, V.B. Nalbandyan, A.A. Petrenko, I.L. Shukaev, V.A. Volotchaev, B.S. Medvedev, J. Solid State Chem. 183 (2010) 684.
V.V. Politaev, V.B. Nalbandyan, Solid State Sciences 11 (2009) 144.
D.A. Porter, K.E. Easterling, M.Y. Sherif, Phase Transformations in Metals and Alloys., CRC Press, Boca Raton, FL, 2009.
A. Riou, A. Lecerf, Y. Gerault, Y. Cudennec, Materials Research Bulletin 27 (1992) 269.
J. Rodriguez-Carvajal, T. Roisnel, Internation Union for Crystallography, Newsletter 20 (1998).
T. Roisnel, J. Rodriguez-Carvajal, Prodeedings of the Seventh European Powder Diffraction Conference (EPDIC 7) (2000) 118.
J.H. Roudebush, N.H. Andersen, R. Ramlau, V.O. Garlea, R. Toft-Petersen, P. Norby, R. Schneider, J.N. Hay, R.J. Cava, Inorg. Chem. (2013).
J.H. Roudebush, R.J. Cava, Journal of Solid State Chemistry 204 (2013) 178.
Royal Society of Chemistry, Introduction to Mössbauer Spectroscopy (2014).
J.A. Russell, Measurement of Optical Bandgap Energies of Semiconductors, Master of Science in Physics, Oregon State University, 2011.
R.E. Schaak, T. Klimczuk, M.L. Foo, R.J. Cava, Nature 424 (2003) 527.

W. Schmidt, R. Berthelot, L. Etienne, A. Wattiaux, M.A. Subramanian, Materials Research Bulletin 50 (2014) 292.
W. Schmidt, R. Berthelot, A.W. Sleight, M.A. Subramanian, Journal of Solid State Chemistry 201 (2013) 178.
E.M. Seibel, J.H. Roudebush, H. Wu, Q. Huang, M.N. Ali, H. Ji, R.J. Cava, Inorg. Chem. 52 (2013) 13605.
L.W. Shacklette, T.R. Jow, L. Townsend, J. Electrochem. Soc. 135 (1988) 2669.
R.D. Shannon, Acta Crystallogr., Sect. A: Found. Crystallogr. 32 (1976) 751.
W.C. Sheets, E.S. Stampler, M.I. Bertoni, M. Sasaki, T.J. Marks, T.O. Mason, K.R. Poeppelmeier, Inorg. Chem. 47 (2008) 2696.
Y.J. Shin, J.P. Doumerc, P. Dordor, C. Delmas, M. Pouchard, P. Hagenmuller, Journal of Solid State Chemistry 107 (1993) 303.
Y. Singh, P. Gegenwart, Phys. Rev. B 82 (2010) 064412.
J.M.S. Skakle, M.A. Castellanos R., S.T. Tovar, A.R. West, J. Solid State Chem. 131 (1997) 115.
D.A. Skoog, F.J. Holler, S.R. Crouch, Principles of Instrumental Analysis., Thomson Brooks/Cole, Belmont, CA, 2007.
O.A. Smirnova, M. Avdeev, V.B. Nalbandyan, V.V. Kharton, F.M.B. Marques, Mater. Res. Bull. 41 (2006) 1056.
O.A. Smirnova, V.B. Nalbandyan, A.A. Petrenko, M. Avdeev, J. Solid State Chem. 178 (2005) 1165.
A.E. Smith, H. Mizoguchi, K. Delaney, N.A. Spaldin, A.W. Sleight, M.A. Subramanian, J. Am. Chem. Soc. 131 (2009) 17084.
T. Sörgel, M. Jansen, Zeitschrift Für Anorganische Und Allgemeine Chemie 631 (2005) 2970.
P. Strobel, B. Lambert-Andron, Journal of Solid State Chemistry 75 (1988) 90.
K. Takada, H. Sakurai, E. Takayama-Muromachi, F. Izumi, R.A. Dilanian, T. Sasaki, Nature 422 (2003) 53.
Y. Takeda, K. Nakahara, M. Nishijima, N. Imanishi, O. Yamamoto, M. Takano, R. Kanno, Mater. Res. Bull. 29 (1994) 659.
J.-M. Tarascon, M. Armand, Nature 414 (2001) 359.
I. Terasaki, Y. Sasago, K. Uchinokura, Phys. Rev. B: Condens. Matter Mater. Phys. 56 (1997) R12685.
B.H. Toby, Journal of Applied Crystallography 34 (2001) 210.
B.H. Toby, (n.d.).
V.W. Urland, R. Hoppe, Z. Anorg. Allg. Chem. 392 (1972) 23.
J.H. Van Vleck, The Theory of Electric and Magnetic Susceptibilities, Oxford University Press, Oxford,, 1952.
L. Viciu, Q. Huang, E. Morosan, H.W. Zandbergen, N.I. Greenbaum, T. McQueen, R.J. Cava, J. Solid State Chem. 180 (2007) 1060.
A.R. West, Basic Solid State Chemistry, John Wiley & Sons, Chichester, 1999.
A. Wichainchai, P. Dordor, J.P. Doumerc, E. Marquestaut, M. Pouchard, P. Hagenmuller, A. Ammar, Journal of Solid State Chemistry 74 (1988) 126.

J. Xu, A. Assoud, N. Soheilnia, S. Derakhshan, H.L. Cuthbert, J.E. Greedan, M.H. Whangbo, H. Kleinke, Inorg. Chem. 44 (2005) 5042.
R.A. Young, International Union of Crystallography, Commission on Powder Diffraction, Netherlands Energy Research Foundation, eds., The Rietveld Method: International Workshop : Papers, Oxf. U. P., 1993.
E.A. Zvereva, O.A. Savelieva, Y.D. Titov, M.A. Evstigneeva, V.B. Nalbandyan, C.N. Kao, J.-Y. Lin, I.A. Presniakov, A.V. Sobolev, S.A. Ibragimov, M. Abdel-Hafiez, Y. Krupskaya, C. Jähne, G. Tan, R. Klingeler, B. Büchner, A.N. Vasiliev, Dalton Trans. 42 (2013) 1550.
E.A. Zvereva, M.A. Evstigneeva, V.B. Nalbandyan, O.A. Savelieva, S.A. Ibragimov, O.S. Volkova, L.I. Medvedeva, A.N. Vasiliev, R. Klingeler, B. Buechner, Dalton Trans. 41 (2012) 572.

Appendix

Appendix A

Solid State Ammonolysis Experimental Setup and Preliminary Experiments

A.1 Experimental Setup

The solid state ammonolysis station was setup using the procedures described by Brophy *et al*. with some modifications for the capabilities of our lab.[1] Figure A.1 shows the complete setup without the regulator on the ammonia tank. The inlet for gas flow is on the right of the furnace and the outlet is on the left and is bubbled through a dilute HCl solution to trap excess ammonia. There is a "Y" split with valves on the inlet line to allow for changing the gas flow from ammonia to N_2 gas for the cool down process. The ammonia gas flow is monitored by the flow through the outlet trap. Upon heating the ammonia reacts with the samples and/or undergoes decomposition which reduces the flow rate at higher temperature therefore the gas flow is monitored regularly throughout the heating cycle to maintain a constant flow rate by adjusting the regulator pressure. The actual flow rate is not known using this setup. The optimal sample position for this setup was determined to be in the center of the tube furnace.

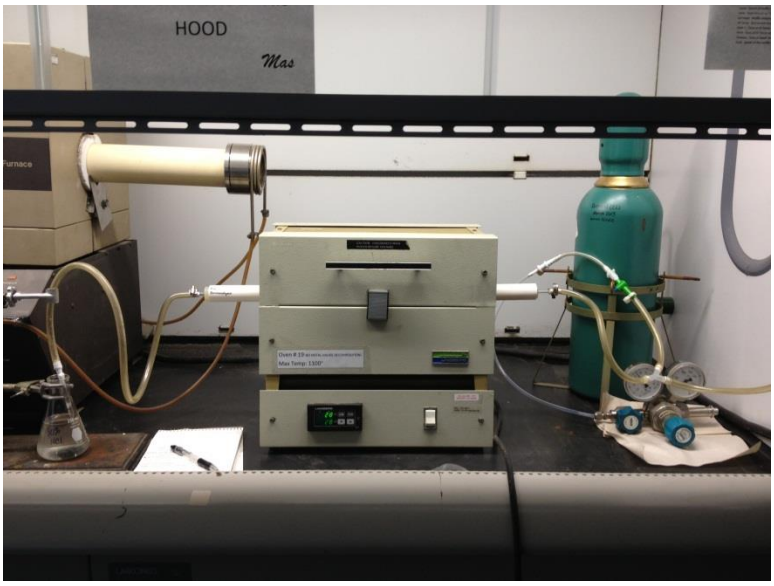

Figure A.1 Furnace setup for solid state ammonolysis reactions.

A.2 Preliminary Synthesis

Syntheses have been attempted by making precursor oxide perovskites or pyrochores or by heating well mixed metal oxide starting materials under an ammonia flow. The powders are loosely packed into small crucibles with a shallow edge. The synthesis temperature has ranged from 500 °C to 950°C depending on the material.[1,2] The reaction was held for 6 hours at temperature for most experiments and upon cooling the gas was switched from ammonia to N_2 gas for the entire cooling period. On a few occasions the ammonia was allowed to flow until the furnace was cooled to 400 °C and then the gas was switched to N_2 gas for the remaining cooling period. This did not improve the results of the experiments therefore was not used for every experiment. The furnace and approximate flow was calibrated following the procedure from Brophy *et al.* for preparation of

$BaTaO_2N$.[1] It was determined that the center of the tube was the optimal position for reaction of the powders with the ammonia gas.

Synthesis of $Y_2TiNbO_{7-x}N_x$ and $Y_2WAlO_{7-x}N_x$ were attempted using the metal oxide starting materials well mixed and loosely packed in alumina boats. The materials were heated two times at 900 °C for 6 hours. The resulting materials were mixed phases of pyrochlores and other ternary metal oxides. There was no indication that N was incorporated into the phases that were present. Successful synthesis of GaN and Ta_2N_5 was performed at 900 °C for 6 hours under ammonia and with N_2 gas flow upon cooling. These materials were used as starting materials in an attempt to synthesize the delafossite oxynitrides, $AgGa_{0.5}Ta_{0.5}ON$ and $CuGa_{0.5}Ta_{0.5}ON$. The metal (I) oxides were mixed in stoichiometric proportions with the prepared GaN and Ta_2N_5 for the desired composition. These materials were sealed in a quartz tube and heated in sealed tubes. Two different synthesis temperatures were tried, 500 °C and 1000 °C for 12 hours which both resulted in mixture of Ag or Cu metal with the other metal oxides. It was noticed upon opening the sealed tubes there was an increase of pressure in the tube due to a large popping sound that occurred upon opening the tube. This indicates that there may have been a release of NO_x gas in the reaction vessel and no N incorporation into the materials. Compositions $Eu_2Ti_2O_7$, $Eu_2Zr_2O_7$ were in their pyrochlore oxide form before ammonolysis using known techniques for synthesis. The $Eu_2Ti_2O_7$ compound was run under ammonia for 6 hours at 900 °C which resulted in a black powder mixed with some white material. Powder X-ray diffraction indicated a product of

$EuTiO_3$, the perovskite material. This indicates a simple reduction of the material with no indication that N was incorporated. The $Eu_2Zr_2O_7$ material showed no reaction under ammonia for 6 hours at 900 °C. Another composition $Sm_2Ru_2O_7$ was attempted starting with the mixed starting oxides and fired at 600 °C for 6 hours. No product was formed under these conditions. A lower temperature was used to prevent total reduction of RuO_2 to Ru metal.

A.3 Acknowledgements

This work was funded by the grant ACS PRF# 52309-ND10 in collaboration with Dr. Macaluso from the University of Northern Colorado.

A.4 References

[1] M.R. Brophy, S.M. Pilgrim, W.A. Schulze, J. Am. Ceram. Soc. 94 (2011) 4263.
[2] F. Tessier, R. Marchand, J. Solid State Chem. 171 (15 February) 143.